ISSN 1068-3755, Surface Engineering and Applied Electrochemistry, 2009, Vol. 45, No. 6, pp. 441–445. © Allerton Press, Inc., 2009.
Original Russian Text © S.A. Baranov, 2009, published in Elektronnaya Obrabotka Materialov, 2009, No. 6, pp. 4–11.

ELECTRICAL PRECISION TREATMENT OF MATERIALS

Magnetic Properties of Micro- and Nanowires in the Superhigh-Frequency Range

S. A. Baranov[a, b]

[a]*Institute of Applied Physics, Academy of Sciences of Moldova, ul. Academiei 5, Chisinau, MD-2028 Republic of Moldova*
[b]*Shevchenko Pridnestrov'e State University, ul. 25 Oktyabrya 128, Tiraspol, Republic of Moldova*
e-mail: baranov@phys.asm.md

Received August 3, 2009

Abstract—The skin-effect theory is presented using the example of an amorphous ferromagnetic material taking into account the ferromagnetic resonance. The theoretical dependence of the impedance of a microwire on its magnetic permeability is determined. The results allow analyzing experiments on studying the high-frequency properties of amorphous microwires.

DOI: 10.3103/S1068375509060015

INTRODUCTION

Current technologies allow obtaining micro- and nanoobjects, in particular, in the form of micro- and nanowires (MNWs). It is difficult to study the electrodynamic properties of MNWs due to their microscopic dimensions. Therefore, the role of noncontact methods for researching the electrodynamic characteristics of MNWs developed for the range of superhigh frequencies (SHF) is increasing.

In addition, the use of MNWs for obtaining of metamaterials is directly related to the practical applications of these materials, which usually exhibit unique high-frequency properties (see, e.g., [1–3]). MNWs serve for the preparation of unique radar absorbent screens (controlled by external fields). It is also possible to obtain materials with negative dispersion [4, 5] and other devices operating in this range of electromagnetic fields.

In this work, we use theoretical approaches that allow analyzing the experimental results. Note that these theoretical approaches were developed for the first time in [6], whose results are discussed here. New results that allow analyzing experiments on studying high-frequency properties of MNWs are obtained as well.

DETERMINATION OF THE WIRE IMPENDANCE IN THE ABSENCE OF FREQUENCY DISPERSION OF THE MAGNETIC PERMEABILITY

In contrast with a direct current, an alternating current in a conductor is distributed nonuniformly over its cross section; it is concentrated over the surface. This phenomenon is called the spin effect; it involves a change in the effective resistance and self-inductance. Below, we give the solution of the Maxwell equations for cylindrical conductors; let us start with the primary analysis of a semiplane.

We shall proceed from the equations for the electromagnetic field (Maxwell equation) in the CGS system:

$$rot\, E = -\frac{\mu}{c}\frac{\partial H}{\partial t}, \tag{1}$$

$$rot\, H = \frac{4\pi\sigma}{c}E + \frac{1}{c}\frac{\partial D}{\partial t}, \tag{2}$$

where σ is the specific conductivity and μ is the magnetic permeability (c is the light velocity in vacuum).

The displacement current density in the conductors is low as compared to the conduction current density; therefore, in the second equation, neglecting the second term, we obtain

$$\nabla^2 E = \frac{4\pi\sigma\mu}{c^2}\frac{\partial E}{\partial t}; \quad \nabla^2 H = \frac{4\pi\sigma\mu}{c}\frac{\partial H}{\partial t}. \tag{3}$$

For a monochromatic field with the frequency ω,

$$\nabla^2 E = 2ip^2 E, \tag{4}$$

where

$$p^2 = \frac{2\pi\mu\sigma\omega}{c^2}.$$

In a simplified case, when an infinite uniform conductor occupies the semispace so that its surface coincides with the plane $z = 0$, the electric field and, therefore, the current are directed along the X axis: ($E_Y = E_Z = 0$). Let E be dependent on the distance from the selected point of the conductor to its surface and independent of X, Y.

In this case, it is easy to obtain the equation from (3):

$$\nabla^2 E_x = \frac{\partial^2 E_x}{\partial z^2} = 2ip^2 E_x, \quad (5)$$

the general solution of which is as follows:

$$E_x = Ae^{kz} + Be^{-kz}.$$

For this equation (and for the more complicated cases below), we will use the complex-valued vector k, the modulus of which will be denoted by p:

$$k = p(1 + i).$$

Let us select only the damped solution

$$E_x = Be^{-pz}e^{i(\omega t - pz)}. \quad (6)$$

Using the real part of this solution, we obtain the solution in the usual form:

$$E_x = Be^{-pz}\cos(\omega t - pz). \quad (7)$$

The current density is expressed by the formula

$$j_x = j_0 e^{-pz}\cos(\omega t - pz). \quad (8)$$

Hence, while penetrating deep into the conductor, the electric vector phase varies linearly, and the amplitude decays by an exponential law. In addition, the main part of the current can be regarded to be localized in the surface layer with the value

$$\delta = 1/p.$$

At this depth, the current density is e times lower than the current density near the conductor surface. The introduced parameters (δ, k, p) can be used for the analysis of cylindrical conductors; the development of the qualitative behavior of an electromagnetic field is useful for the analysis of a more complicated case. Note that, for comparison, the mentioned parameters are often used for nonmagnetic samples (when the magnetic permeability $\mu = 1$); in this case, we shall denote them using δ_0, k_0, and p_0.

The alternating current in a cylindrical conductor is also concentrated on its surface; the effect is stronger at higher current frequencys. The current concentration on the surface involves a change in the resistance and self-inductance; hence, these value variations depend on the current frequency. If the total current is concentrated in the surface layer of a cylindrical wire, then the resistance of the latter must approach the resistance of the cylindrical surface having walls of respective thickness (on the order of δ). As the frequency increases, the thickness of the conducting layer decreases; therefore, the conductor resistance must increase. Since the analysis of the plane is of interest for us only in comparison with a cylindrical conductor, let us proceed to this case.

Consider a cylindrical conductor with the radius $r_0 \equiv r_{zh}$. Let us introduce a cylindrical coordinate system, the axis of which coincides with that of the cylindrical wire. The direction along the wire axis is taken as the direction of the field E. The intensity of E is equal to the projection of E on the axis z in modulus; it depends on the coordinate r only. In this case, equations of type (3)–(5) are written in the form

$$\frac{d^2E}{dr^2} + \frac{1}{r}\frac{dE}{dr} - 2ip^2E = 0. \quad (9)$$

There is only one solution (accurate within an arbitrary constant factor) of the equation that remains final on the wire axis; this solution is called the zero-order Bessel function of the argument $pr\sqrt{-2i}$

$$E = const\, J_0(pr\sqrt{-2i}). \quad (10)$$

The asymptotic expressions have the following form: if

$$pr_0 \ll 1, \text{ or } \quad r_0 \ll \delta,$$

then

$$J_0(pr\sqrt{-2i}) \cong 1 + \frac{i(pr_0)^2}{2} - \frac{(pr_0)^4}{4}, \quad (11)$$

and if

$$pr_0 \gg 1, \text{ or } \quad r_0 \gg \delta,$$

then

$$J_0(pr\sqrt{-2i}) \cong A\frac{e^{pr_0 - i(pr_0 - \pi/8)}}{\sqrt{2\pi pr_0}}. \quad (12)$$

The amplitude of the real part of the current density will increase while moving from the current axis in proportion to

$$1 + \frac{(pr)^4}{16}.$$

In the case of high frequencies and thick wires $pr_0 \gg 1$, an approximate expression can be used:

$$E \sim \text{const}\frac{e^{pr - i(pr - \pi/8)}}{\sqrt{r}}. \quad (13)$$

At a considerable distance from the wire, this expression can be extrapolated in the form of (in order to compare this result with formulas (6) and (7))

$$E_z \sim Ae^{-p(r_0 - r)}\cos(\omega t + \pi/8 - pr). \quad (14)$$

The asymptotic formula for the current will be expressed as follows:

$$j \approx Ce^{-p(r_0 - r)}\cos(\omega t + \pi/8 - pr). \quad (15)$$

As one can see from formula (15), the current density decreases exponentially while moving from the conductor surface deep into the conductor; that is, the main part of the current is localized in the surface layer, which is in

complete agreement with analogous formula (8). For the electric field intensity in the general form,

$$E_z = \text{const}\, J_0(kr)e^{-i\omega t} \tag{16a}$$

(for the sake of convenience, we again use the complex wave vector $k = (1 + i)\, p = (1 + i)/\delta$).

For the magnetic field intensity, using the Maxwell equation (formulae (1), (2)), we obtain

$$\frac{i\omega}{c}H_\varphi = rot_\varphi E = -\frac{\partial E_z}{\partial r}.$$

Since

$$J_0'(x) = -J_1(x),$$

then, finally, for the magnetic field intensity,

$$H_\varphi = -i\,\text{const}\sqrt{\frac{4\pi\sigma i}{\omega}}J_1(kr)e^{-i\omega t}. \tag{16b}$$

Note that the same factor const enters the electric and magnetic field. We can assume that, on the conductor surface,

$$H = \frac{2I}{cr_0}.$$

In concept, the value of this constant can be expressed through the electric current *I*. (The latter is equivalent to the so-called Leontovich–Shchukin boundary condition and is not always valid for small particles).

Let us write the result for the electric-to-magnetic field ratio, which determines the wire's complex resistance per unit of length (that is, the complex resistance of the wire unit length):

$$\begin{aligned} Z &= \left(\frac{k}{2\pi\sigma r_0}\right)\frac{J_0(kr_0)}{J_1(kr_0)} = R_{surf.}k\frac{J_0(kr_0)}{J_1(kr_0)} \\ &= R_{per\ unit\ of\ length} = \left(\frac{kr_0}{2}\right)\frac{J_0(kr_0)}{J_1(kr_0)}, \end{aligned} \tag{17}$$

where the notion of the surface resistivity or complex resistance per unit of length at a constant current is introduced:

$$R_{surf.} = \frac{1}{2\pi r_0\sigma}; \quad R_{per\ unit\ of\ length} = \frac{1}{pr_0^2\sigma}. \tag{18}$$

Equation (17), generally speaking, does not depend on the boundary conditions; it is rather general for MNWs.

Formula (17) is of great help for experimental analyses (see, e.g., [6–9]); however, the domain of its applicability is not limited to the magnetic resonance that

often takes place in ferromagnetic materials. Below, we discuss the theory taking into consideration the ferromagnetic resonance (FMR).

LINEARIZED LANDAU–LIFSHITZ EQUATIONS FOR AMORPHOUS FERROMAGNETICS

The ferromagnetic properties of substances are described by the Landau–Lifshits equation:

$$\frac{dM}{dt} = -\gamma[M \times \hat{H}], \tag{19}$$

where γ is the gyromagnetic ratio, where $\hat{H} = H_{exch} + H_{anis} + H_{ext}$; $H_{exch} = \alpha\nabla^2 M$; H_{anis} is the internal field, which is the anisotropy field and is proportional to the mechanical stresses and magnetostriction in the case of amorphous ferromagnetics; and H_{ext} is the external magnetic field.

To linearize the equation, we consider the system's magnetization intensity in the form of a constant and small variable (time dependent) component:

$$M = M_0 + m(t). \tag{20}$$

We shall neglect the second-order terms, assuming that the external field

$$H_{ext} = H_0 + h(t) \tag{21}$$

also consists of a constant and small variable (time dependent) component.

Let us present the linearized variant of equation (19) in Cartesian coordinates by setting

$$m(t) \approx me^{-i\omega t}, \tag{22}$$

where the two-component vector $-m(m_x, m_y)$ is introduced.

Thereupon, equation (21) has the form

$$\begin{aligned} i\omega\ m_x &= -\gamma\ \hat{H}\ m_y - \gamma\ \ M_0 h_y; \\ -i\omega\ m_y &= \gamma\ \ \hat{H}\ m_x + \gamma\ M_0\ \ h_y. \end{aligned} \tag{23}$$

Equations (14) can be diagonalized by introducing coordinates with vectors:

$$a_\pm = x \pm iy. \tag{24}$$

Using their properties, we obtain for the magnetization vector

$$M_\pm = \frac{\omega_M}{\omega_H \pm \omega}. \tag{25}$$

Here,

$$\omega_M = \gamma M_0; \quad \omega_H = \gamma\hat{H}. \tag{26}$$

Let us introduce the resonance and nonresonance magnetic permeabilities:

$$\mu_\pm \sim \frac{\omega_M}{\omega_H \pm \omega}. \tag{27}$$

We shall take into consideration the relaxation phenomena replacing ω by $\tilde{\omega} \longrightarrow \omega - i\gamma$, where γ is responsible for the ferromagnetic resonance width.

CYLINDRICAL WAVE DISPERSION IN AMORPHOUS WIRES

We shall begin with the rearrangements of the Maxwell equations in a rotating coordinate system. Let us consider the formula

$$\nabla \times [\nabla \times H] = \nabla(\nabla \cdot H) - \nabla^2 H.$$

The first term in the right-hand side of this formula in fixed coordinates is zero; however, it must be taken into consideration in a rotating system.

We shall write the Maxwell equation in a rotating coordinate system:

$$\begin{aligned} B_- &= i\mu_0 \frac{\delta_0^2}{4}(\nabla^-\nabla^- H_+ - \nabla^+\nabla^- H_-); \\ B_+ &= i\mu_0 \frac{\delta_0^2}{4}(\nabla^+\nabla^+ H_- - \nabla^+\nabla^- H_+). \end{aligned} \tag{28}$$

The general solution of the equations will be presented in the form of an eigen-function series of the operator ∇^2 in a cylindrical coordinate system (we choose only the functions that do not diverge at $r \longrightarrow 0$). These functions have the form

$$f_n(kr) = e^{in\varphi} J_n(kr), \tag{29}$$

where k is the propagation constant.

There is a limiting case of proceeding to formulae (16a), (16b) when

$$E \sim J_0(k_0 r); \quad H \sim J_1(k_0 r). \tag{30}$$

Let us present the nabla operator in the form

$$\nabla^{\pm} = \frac{\partial}{\partial x} \pm i\frac{\partial}{\partial y}.$$

This operator in a spherical coordinate system is as follows:

$$\nabla^{\pm} = \frac{\partial}{\partial r} e^{\pm i\varphi} \pm \frac{i}{r} e^{\pm i\varphi} \frac{\partial}{\partial \varphi}.$$

Thereupon, using the relations for the Bessel functions $\rho\, J_n'(\rho) = -n\, J_n(\rho) + \rho\, J_{n-1}(\rho)$,

$$\rho\, J_n'(\rho) = n\, J_n(\rho) - \rho\, J_{n+1}(\rho),$$

we obtain

$$\nabla^{\pm} f_n(kr) = \pm n f_{n\pm 1}(kr). \tag{31}$$

The introduced nabla operators are analogs of birth and annihilation operators.

Using the properties of the functions (their orthogonality), we present the expansion of H and B into an eigen-function series, where the value of the wave vector parameter K is not determined yet (here, it is presented as an undetermined parameter of the problem); n ranges from 1 to infinity

$$H_{\pm} = \sum_n H_n^{\pm} f_{n\pm 1}(kr);$$

$$B_{\pm} = \sum_n B_n^{\pm} f_{n\pm 1}(kr).$$

For the decomposition amplitude, we obtain (introducing a yet undetermined dimensionless wave vector K)

$$\begin{aligned} B_{n\pm} &= iK^2(H_n^+ + H_n^-); \quad B_{n\pm} = \mu_{\pm} \cdot H_n^{\pm}; \\ K^2 &= \mu_0 \delta_0^2 \frac{k^2}{4}. \end{aligned} \tag{32}$$

For a homogeneous system, a nontrivial solution takes place only in the case if the system's determinant is zero. We obtain the equation for the determination of the parameter K:

$$\begin{vmatrix} iK^2 + \mu_+ & iK^2 \\ iK^2 & iK^2 + \mu_- \end{vmatrix} = 0. \tag{33}$$

Hence,

$$\mu_-\mu_+ + iK^2(\mu_+ + \mu_-) = 0. \tag{34}$$

The dispersion equation with respect to the parameter K, if it is determined, is a binary cubic. Therefore, it describes three types of dispersion. This is the dispersion of fundamental, spin, and surface waves (spin and surface waves will not be discussed below).

If the characteristic sizes of an object are less than the wavelength, then (according to the Leontovich–Shchukin condition) we can introduce the notion of impedance $Z(\omega)$, which characterizes the relation between the modes E and H at the conductor boundary in the form

$$E_\omega = Z(\omega) \cdot H_\omega. \tag{35}$$

To find $Z(\omega)$, the known boundary conditions are written; in our case, they are expressed in the form of the continuity conditions H_φ and E_z at the conductor boundary (it is necessary to proceed to a cylindrical coordinate system). Due to the awkwardness of these relations, we will not give them here.

Since each n-mode is independent in a linear approximation,

$$Z = \sum_n Z_n. \tag{36}$$

For each wave,

$$K_j \; j = (1, 2, 3); \quad E_n = \sum_j A_j b_j;$$

$$Z_n H_n = \sum_j B_j b_j.$$

Note that E_n and H_n are related by the Maxwell equation and the external field $E_n = H_n$. For the completeness of the problem, we shall set the vector $B_{n,r}$ (or $M_{n,r}$) at the boundary taking into account the surface magnetism: $\frac{\partial M_r^{\pm}}{\partial r} - K' M_r^{\pm} = 0$, $K' = \frac{K_S}{A}$, and K_S is the surface magnetism anisotropy (A is the exchange interaction).

We obtain the solution for Z_n:

$$Z_n = \frac{\Delta_1}{\Delta},$$

where

$$\Delta = \begin{vmatrix} H_n & B_j & \cdot & \cdot \\ 0 & A_j & \cdot & \cdot \\ 0 & X_j & \cdot & \cdot \\ 0 & Y_j & \cdot & \cdot \end{vmatrix} \quad \Delta_1 = \begin{vmatrix} H_n & 0 & 0 & 0 \\ A_j & B_j & \cdot & \cdot \\ \cdot & X_j & \cdot & \cdot \\ \cdot & Y_j & \cdot & \cdot \end{vmatrix}.$$

Therefore,

$$Z_n = \frac{\begin{vmatrix} B_j & \cdot & \cdot \\ X_j & \cdot & \cdot \\ Y_j & \cdot & \cdot \end{vmatrix}}{\begin{vmatrix} A_j & \cdot & \cdot \\ X_j & \cdot & \cdot \\ Y_j & \cdot & \cdot \end{vmatrix}}.$$

The coefficients $A, B, \ldots, X, Y$ have the form

$$A_{jn} = \frac{1}{2}\left[\frac{1}{\mu_{-j}} J_{n-1}(k_j r) - \frac{1}{\mu_{+j}} J_{n+1}(k_j r)\right];$$

$$B_{jn} = \rho \frac{k_j}{\mu_{\text{eff}.\,j}} J_n(k_j r);$$

$$X_j^n = \left(\frac{1}{\mu_0} - \frac{1}{\mu_{-j}}\right) C_{jn};$$

$$Y_j^n = \left(\frac{1}{\mu_0} - \frac{1}{\mu_{+j}}\right) C_{jn};$$

$$C_{jn} = k_j J'_{n-1}(k_j r) - K' J_{n-1}(k_j r).$$

If we neglect all the modes j except for the principal uniform resonance, then

$$Z_n \sim \rho \quad k_4 \frac{J_{n-1}(k_4 r)}{J_n(k_4 r)}.$$

In the case when the skin layer is much less than the radius, we can obtain the known formula for a plane, when

$$Z \sim \rho k,$$

where

$$k \approx \mu^{\frac{1}{2}}.$$

It is this approximation that was used for the basic research of FMR using standard microwave spectroscopes.

We will discuss the influence of spin and surface waves on the resonance in a separate paper.

CONCLUSIONS

(i) The skin-effect theory is discussed using the example of a ferromagnetic material taking into account the FRM in the case of cylindrical samples.

(ii) The theoretical dependence of the wave resistance of the MNWs on their magnetic permeability, electromagnetic field frequency, conductivity, and wire radius is obtained.

(iii) The result allows analyzing experiments on studying the high-frequency properties of ferromagnetic MNWs, which is an extremely important problem in terms of studying the magnetic properties of metamaterials.

REFERENCES

1. Baranov, S.A., Zotov, S.K., Larin, V.S., and Torkunov, A.V., Specific Features of Natural Ferromagnetic Resonance in an Amorphous Microwire, *Fiz. Met. Metalloved.*, 1991, vol. 69, issue 12, pp. 172–173.
2. Baranov, S.A., Berzhanskii, V.N., Zotov, S.K. et al., Ferromagnetic Resonance in Amorphous Magnetic Wires, *Fiz. Met. Metalloved.*, 1989, vol. 67, issue 1, pp. 73–78.
3. Baranov, S.A. and Stoyanov, S.S., Study of Microwire by Ferromagnetic Resonance Method, *Elektron. Obrab. Mater.*, 2006, no. 3, pp. 191–195 [*Surf. Eng. Appl. Electrochem.* (Engl. Transl.), vol. 42, no. 3, p. 94].
4. Baranov, S.A., Colpacovici, I., Kleimenov, V., Bugakov, V., and Usenco, V., Composite on the Basis of Microwire with Negative Value of Permeability in Microwave Range of Frequencies, *Moldavian J. Phys. Sci.,* 2003, vol. 2, no. 2, pp. 174–176.
5. Baranov, S.A. and Usenko, V.P., A Composite of Microwire with Negative Refraction, *Elektron. Obrab. Mater.*, 2003, no. 5, pp. 89–90.
6. Kraus, L., Theory of Ferromagnetic Resonances in Thin Wires, *Czech J. Phys.*, 1982, vol. B32, pp. 1264–1282.
7. Landau, L.D. and Lifshits, E.M., *Elektrodinamika sploshnykh sred* (Electrodynamics of Continua), Moscow: GITTL, 1957.
8. Zuberek, R., Szymezak, H., Gutowski, M., Zhukov, A., Zhukova, V., Usov, N.A., Garcia, K., and Vazquez, M., *J. Magn. Magn. Mater.*, 2007, vol. 316, pp. 890–894.
9. Reynet, O., Adenot, A.-L., Deprot, S., and Acher, O., Effect of the Magnetic Properties of the Inclusions on the High-Frequency Dielectric Response, *Phys. Rev.*, 2002, vol. B66, pp. 094412–094420.

ISSN 1068-3755, Surface Engineering and Applied Electrochemistry, 2009, Vol. 45, No. 6, pp. 446–454. © Allerton Press, Inc., 2009.
Original Russian Text © S.S. Belevskii, S.P. Yushchenko, A.I. Dikusar, 2009, published in Elektronnaya Obrabotka Materialov, 2009, No. 6, pp. 12–21.

ELECTRICAL SURFACE TREATMENT METHODS

Electrodeposition of Nanocrystalline Co–W Coatings from Citrate Electrolytes under Conditions of Controlled Hydrodynamics : Part 1 Co Electrodeposition

S. S. Belevskii, S. P. Yushchenko, and A. I. Dikusar

Institute of Applied Physics, Academy of Sciences of Moldova, ul. Akademiei 5, Chisinau, MD-2028 Republic of Moldova
e-mail: dikusar@phys.asm.md

Received October 1, 2009

Abstract—The results of complex research of cobalt electrodeposition under controllable hydrodynamic conditions with a rotating cylindrical electrode (RCE) from a citrate electrolyte used for obtaining cobalt–tungsten coatings are presented. The influence of the electrolyte pH on the change of the state of the cobalt in the solution, the electrodeposition rate, and the surface morphology is shown. The oscillatory process at potentials close to stationary has been detected and its mechanism is offered. The hydrodynamic conditions (the electric deposition current density increase with the growth of the RCE rotation speed) have been observed have an affect only at $Re \geq 200$ and to occur at reaching a certain thicknesses of the electrodeposited layer. The existence of a linear dependence between the current density and the potential of the electric deposition suggests the probability of the formation of a film in the initial period of the deposition.

DOI: 10.3103/S1068375509060027

Electrolytic coatings characterized by such functional properties as high corrosion resistance to hostile environments at high temperatures, high strength, high wear resistance, etc., have been extensively used in various branches of industry. Electrolytic chromium coatings satisfy to a greater extent the above necessary set of requirements. However, the technological conditions of their obtaining from solutions that contain hexavalent chromium are considered to be ecologically destructive ones; hence, a number of the European Commission's directives place restrictions on the industrial application of this technology [1, 2].

As was shown in [3], the Co–W alloy electrolytic coatings obtained from citrate solutions close to neutral are found to be the most appropriate ones to replace chromium coatings. An obligatory condition of the latter is the investigation of the various functional properties of such coatings along with the detailed examination of the optimal conditions for their realization. As is shown in [4], the unique character of the corrosive and mechanical properties of such coatings may be explained by the fact that they are crystalline (the characteristic size of the crystallites ranges within several nanometers). It has been noted repeatedly that the functional properties of such coatings depend to a great extent on the alloy composition, first of all, on the tungsten content [3–7].

It is known that the cobalt–tungsten coatings obtained from citrate solutions are referred to the category of coatings whose electrodeposition occurs due to the so called induced codeposition. The general properties of these processes have been examined for the deposition of various metals of iron groups with molybdenum, tungsten and rhenium [8–11]. Their characteristic peculiarity is that the composition of such coatings and, hence, their properties depend on the hydrodynamic conditions of the deposition. Concerning the cobalt–tungsten coatings obtained from citrate solutions, this has been demonstrated, in particular, by [7]. However, the results obtained in [7] are only qualitatively indicative of the role of the hydrodynamic conditions in obtaining cobalt–tungsten coatings by induced electrodeposition, since the hydrodynamic conditions used in this work were not, strictly speaking, controllable ones.

Our series of papers, the first of which is the present one, deal with the experimental investigation of the deposition processes under controllable hydrodynamic conditions and the application of a rotating cylindrical electrode (RCE) and also of a so called Hull's cell with RCE [10–13]. The purpose of this series of papers is not only the development of the fundamentals of the mechanism of the induced codeposition of cobalt–tungsten alloys but also the study of the influence of the hydrodynamic conditions of the deposition on the technological characteristics of the coating, for example, such as the micro- and macrodistribution of the deposition rates, as well as the composition and functional properties of the surfaces being obtained.

The present paper is devoted to the research of the role of the hydrodynamic conditions in the electrodeposition process of cobalt from a citrate solution as the main process, the result of which is the deposition of an alloy because tungsten fails to be deposited from aque-

ous solutions without cobalt or other iron group metals being deposited [8, 9, 12].

METHODS OF INVESTIGATION

The Electrolyte Composition and Its Peculiarities

In papers [4–7, 15], there was used an electrolyte for the deposition of cobalt–tungsten alloys of the following composition (mol/l): Na_2WO_4—0.2; $CoSO_4$—0.2; $C_6H_8O_7$ (citric acid)—0.04; $Na_3C_6H_5O_7$ (sodium citrate)—0.25; H_3BO_3—0.65 (pH = 6.6). The deposition temperature equaled 60°C. It is these conditions that will be used in the series of papers, the first of which is the present paper. However, taking into account the aim of the present paper, there was used an electrolyte of the above composition but without sodium tungstate with the pH being varied in the range of 4–7. In some cases, for the purpose of comparison, there was used an aqueous solution of $CoSO_4$ of the electrolyte concentration but with no citrate, citric, or boric acids.

The electrolyte containing cobalt citrate and boric acid was studied for the Co(II) content by means of potentiometric titration using a solution of $K_3[Fe(CN)_6]$ with a tungsten electrode [16]. The method is based on the reduction of the ammonia complex Co(II) using a solution of Fe(III). The determination was performed in the range of pH values from 4 to 7. This was correlated with the fact that the pH of the initial solution of the cobalt citrate complex with the boric acid equaled 4.95 and, after the sodium tungstate addition to it (of the concentration relevant to the one of the electrolyte), it made up 6.8. The pH was varied by the addition of both the ammonium solution and NaOH. As will be shown below, the essential changes of the Co(II) concentration values were not determined due to the method of the pH varying failing.

Both the aqueous solution of the cobalt sulfate and the citrate solutions at various pH values were studied by the measurement of the absorption spectra in the visible region with an SF46 spectrophotometer. *The electrochemical measurements* were performed by making use of the RCE from steel St3, the design of which is presented in Fig. 1. The height of the RCE operation surface h equaled 15 mm with its radius r being 5 mm. The RCE of the visible area made up 4.7 cm^2. The remaining part of the area was insulated. The insulation diameter a at the upper and bottom parts equaled 22 mm. The insulation height l = 25 mm.

Prior to the electrodeposition, the surface was coated by a layer of nickel from an electrolyte that comprised nickel chloride (hexaqueous) with a concentration of 240 g/l and chlorohydric acid with a concentration of 80 g/l. The electrodeposition duration was 1 min at a current density of 30 mA/cm^2. The very technique of obtaining the cobalt–tungsten coatings on steel (with a nickel underlayer coating) was used earlier [4–7]. It was also applied in the series of experiments discussed in the present paper for the cobalt electrodeposition.

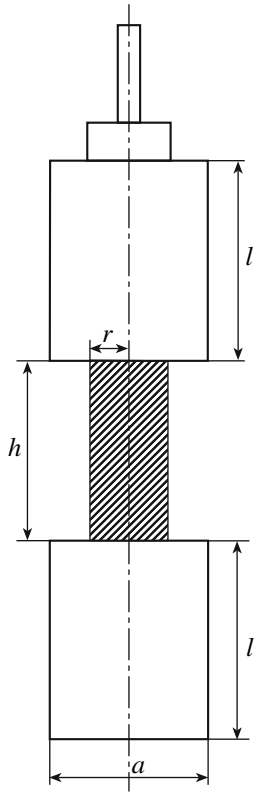

Fig. 1. The RCE scheme (see the text for the details).

The deposition temperature of all the experiments hereinafter described, except for specified cases, equaled 60°C.

The speed of the RCE rotation varied from 0.3 to 165 rpm. As will be shown below, the rotation speeds varying from 0.3 to 11 rpm actually produced no changes in the electrochemical characteristics of the deposition, and, at higher values, there was observed an influence, for example, on the potential of the deposition at a fixed current or on the current density at a fixed potential. Evidently, the reason lies in the RCE attaining certain Reynolds numbers. The turbulent regime is known to be reached at the RCE when $\mathrm{Re} = \frac{\omega r^2}{\nu} =$ ~200 (ω is the cylinder rotation frequency, s^{-1}; r is the RCE radius; and ν is the kinematic viscosity, cm^2/s) [11–17].

For the purpose of the calculation the Reynolds criterion, there was determined the kinematic viscosity of the examined electrolyte at 60°C, which turned out to be 0.72×10^{-2} cm^2/s for the electrolyte with sodium tungstate and 0.63×10^{-2} cm^2/s for the electrolyte without sodium tungstate. This implies that the transition to the turbulent flow regime (characterized by the equal availability of the electrode surface along its plane at a diffusional regime and the known calculation ratios for the definition of the thicknesses of the hydrodynamic

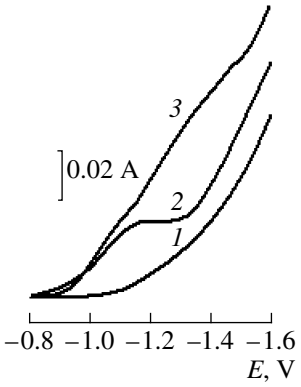

Fig. 2. Voltamperograms obtained in electrolytes I (*1*), II (*2*), and III (*3*) for the RCE at a rotation speed of 0 rpm and a temperature of 20°C. The potential change rate is 100 mV/s.

boundary layer and the limiting diffusional currents [11, 17]) is expected to be observed at the rotation speeds of the cylindrical electrode of 45–50 rpm.

In the process of the RCE, the application the potentiodynamic polarization curves was registered at various rotation speeds, which were taken down at the potential applying rates from 1 to 100 mV/s. This was performed at the potential variation from stationary to –(1.4–1.5) V. During all the measurements, there was used a saturated silver–chloride electrode as the comparison electrode, the measured (or preset) values of which were recalculated for the hydrogen scale. All the values presented below correspond to the potentials in relation to the hydrogen electrode. Along with the potentiodynamic dependences, there were also fixed the dependences of the current density on the time at a fixed potential, including the use of a tungstateless electrolyte with various pH values.

A 10 mm thick 60 × 40 mm graphite plate was the anode. There were two variants of the measurements: with separated and nonseparated anode and cathode spaces. In the first case, the anode was located in a separate cell connected with the cathode by a salt bridge filled with a 20% sodium sulfate solution.

Initially, in order to determine the region of potentials in which the deposition occurs, the potentiodynamic polarization curves at a temperature of 20°C and the rate of the potential applying of 100 mV/s in a nonagitated solution were fixed, while making use of three kinds of electrolytes: the electrolyte containing only sodium tungstate (electrolyte I), the electrolyte containing only cobalt sulfate (electrolyte II) and the electrolyte containing both tungstate and cobalt sulfate (electrolyte III). All the remaining electrolyte components and their concentrations remained constant (they are presented above). The corresponding polarization curves are illustrated in Fig. 2.

The basic electrolyte being examined in the present paper was electrolyte II. Subsequent publications will comprise the investigations of the composition and properties of the electrolytic coatings obtained from electrolyte III.

One can see that, in the electrolyte containing cobalt sulfate in a citrate solution, in the region of the potentials of –(0.9–1.3) V, there are observed the currents of reduction missing in the solution that contains only tungstate. The current densities in this region of potentials increase significantly in electrolyte III. In other words, the results presented in Fig. 2 clearly show the effect of the induced reduction revealed in this solution in the interval of potentials of –0.9 V and above that.

In the same region of potentials, there was defined the current efficiency of the cobalt electrodeposition fixed by the specimens' weight increase after a certain quantity of the electricity was applied. The value of the transferred charge was measured on the basis of the integration of the current–time curves at the potentiostatic mode. Since there were used solutions with various pH values and the deposition was carried out at various rotation speeds, for which the current density values differed greatly, the values of the weight change were various (occurring, among other factors, due to the different values of the current efficiency), ranging from 10 to 60 mg.

The morphology of the obtained surface was observed by means of a scanning electron microscope (TESCAN VEGA).

RESULTS AND DISCUSSION

The cobalt state in the solution

As follows, for example, from [18] (see also [19]), there may occur various forms of cobalt citrate complexes (along with hydrated Co(II)) with regard to the cobalt and citrate concentration in the solution (and their ratios as well). The ratio of the various cobalt forms significantly changes with the pH varying. In the acidic solution, the hydrated cobalt ion concentration is maximal, while, in the solutions close to neutral, that of $[CoCit]^-$ [18] prevails.

The probability of various cobalt complexes' existence in the solution being explored is confirmed by the potentiometric titration results (Fig. 3). It is evident that the cobalt concentration determined by means of the potentiometric titration method [16] corresponds to the analytical concentration only up to pH values of about 5.5. With the pH increase to 7, the measured concentration decreases by several times. It should be emphasized that the change (with the pH increase) of the cobalt concentration being determined is irrespective of the kind of the added solution; this change may be provided by ammonia or NaOH (Fig. 3).

This is worth noting, since the potentiometric determination method of cobalt [16] is based on its ammonia complex oxidation by a solution of $K_3[Fe(CN)_6]$.

The probability of the origination of different forms of complex cobalt compounds at various pH values has been confirmed by the investigation results of the solu-

tions' absorption spectra (Fig. 4, the thickness of the utilized vessels was 0.1 cm). Figure 4 presents the absorption spectra of the aqueous solutions of pure cobalt sulfate along with the spectra in the presence of a blend of sodium citrate and citric acid at various pHs. One can see that, on the addition of the complex-forming agents' blend at pH 4, the character of the spectrum (curve *2*) actually remains unchanged. The absorption peak found observed in the region of 510–530 nm for the cobalt sulfate (curve *1*) shifts to the long wave region by 10 nm with increasing absorption intensity. Such kind of behavior may be indicative of the formation of a low-molecular dimeric complex with a citrate ion, as described in [20].

With the pH increase to 7, the solution coloring intensity grows and the color changes from red-violet to lilac dark blue. These changes are distinctly exhibited by the sharp modifications of the absorption spectrum character (curve *3*). The peak at 520 nm changes its form and shifts still further to the long wave region, and the absorption intensity increases. In the region of 680–780 nm, there appears a wide peak of medium intensity. The occurrence of such a kind of broadened peaks testifies to the formation of polynuclear polymeric compounds in the solution, similar to the ones described in [21, 22].

Thus, it seems evident that, in the investigated solution, cobalt may exist in various kinds of forms at the pH varying with these forms not being limited to only low-molecular complexes, as was expected on the basis of the data presented in [18, 19] in particular. The probability of the existence of the cobalt polymer compounds, which is indicated by the absorption peak in the region of 680–780 nm, was qualitatively shown by us in the experiments on the gel-filtration separation of the solution components. The results of these experiments will be presented in an independent report.

In [7], it was shown that, in the citrate electrolyte, in the presence of sodium tungstate, the absorption spectrum was similar to the one introduced in Fig. 4 (curve *3*). Taking into account that, when tungstate is added in a concentration relevant to its content in obtaining the cobalt–tungsten coatings (pH changes up to 6.8–7), the formation of the polymer complexes may also be observed at the citrate electrolytes' application used for obtaining such coatings.

Elecrodeposition at Low Current Densities (Potentials) The oscillatory deposition-passivation process

The electrodeposition in this region of the potentials differed greatly with respect to the fact whether or not it occurred under conditions of nonseparated (Fig. 5) or separated anode and cathode spaces (Fig. 6). Moreover, the oscillatory process being observed here took place only in the case of relatively low rates of the potential modifications (in particular, at 1 mV/s). At high rates, for example, 100 mV/s, it failed to be registered.

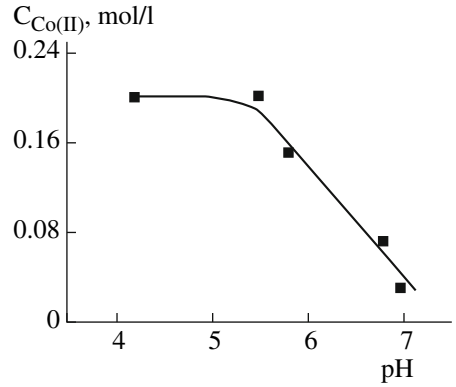

Fig. 3. The dependence of the cobalt (II) concentration in the citrate solution on the pH obtained by potentiometric titration at its analytic concentration of 0.2 mol/l in the solution.

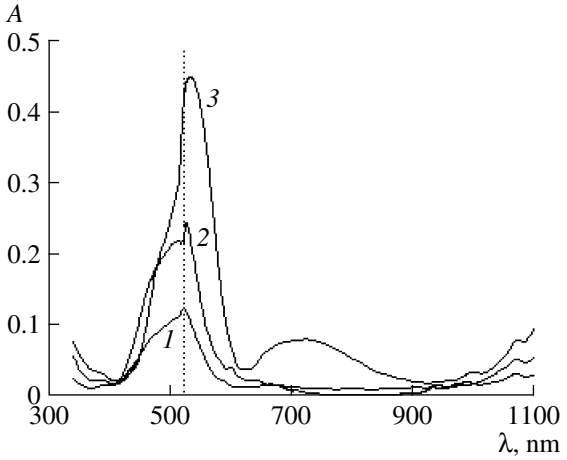

Fig. 4. The absorption spectra of the aqueous solutions of cobalt sulfate (*1*); $CoSO_4$ + citric acid + sodium citrate at pH ~ 4 (*2*); and the same at pH ~ 7 (*3*).

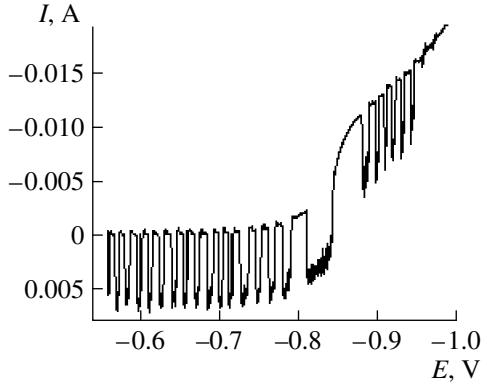

Fig. 5. Voltamperogram obtained in electrolyte II at the RCE rotating at a speed of 45 rpm at a 1 mV/s change of the rate in a cell with nonseparated electrode spaces.

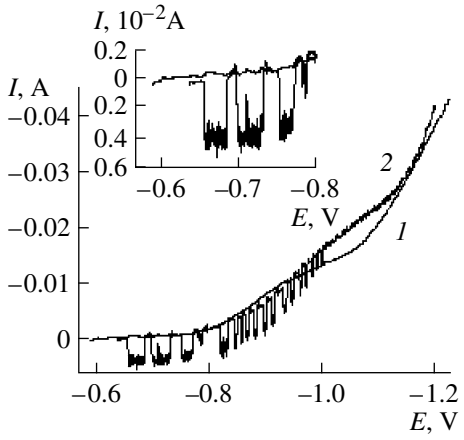

Fig. 6. Voltamperograms obtained in electrolyte II at the RCE rotating at a speed of 11 rpm at a 1 mV/s change of the rate in the cells with separated (*1*) and nonseparated (*2*) electrode spaces. In the insert, there is shown a fragment of the voltamperogram at the potentials close to stationary.

Although electrodeposition in this region of the potentials is actually not realized, the research of the occurring processes is of great importance, since the macrodistribution of the electrodeposited layers' thicknesses, i.e., the throwing power of the electrolytes, depends on the rates of the reactions in this region.

From the curves in Fig. 5 and Fig. 6, one can see that, when the potential shifts from its stationary value to the cathode direction, there arise periodic sharp peaks of the anode current at the various RCE rotation speeds. The frequency of such oscillations increases with the cathode potential growth and their amplitude decreases (Fig. 6). Since, at the separated anode and cathode spaces, this effect vanishes, one may assume that it is caused by the cathode reduction of the dissolved oxygen, whose concentration sharply rises under the conditions of its anodic generating. It is known indeed that the final products of the dissolved oxygen reduction are OH^- ions:

$$O_2 + 2H_2O + 4e = 4OH^-. \quad (1)$$

The abrupt alkalization of the solution may cause the anodic dissolution of the depositing cobalt (or nickel which serves as a substrate for the cobalt deposition) according to the following reactions:

$$Co + 2OH^- = Co(OH)_2 + 2e, \quad (2)$$

$$Ni + 2OH^- = Ni(OH)_2 + 2e. \quad (3)$$

The normal equilibrium oxidation–reduction potentials for reactions (2) and (3) relatively equal –0.73 and –0.72 V [23], and considering the alkalization due to reaction (1), the equilibrium potential may shift towards even greater cathode potentials. However, the dissolution (in the region of the cathode potentials) of cobalt (or a nickel substrate) according to reactions (2) and (3) leads to the formation of a cobaltic (nickel) hydroxide dead layer at the surface, further inhibiting the dissolution.

With a further shift of the potential towards the cathode region at this layer, the oxygen reduction will be observed again and the process reiterates. At the potentials exceeding –0.8 V, together with the oxygen reduction, there will occur Co(II) reduction, which will cause the amplitude decrease of the anode oscillations and their frequency growth actually up to the oscillatory process's total termination (see Fig. 6). It is evident that the occurrence of these processes should lead to the output decrease of the electrodeposition current. Indeed, at the potential –1.0 V, the current efficiency with the rotation speed of 85 rpm amounted to only 38% at the nonseparated anode and cathode spaces with the electrolyte pH being 7.

It is evident that, under these conditions, along with the electrodeposition of cobalt, there occurs the process of its corrosion with the oxygen depolarizing.

The current efficiency with the electrolyte pH being 7 (at the same potential value but with separated anode and cathode spaces) turned out to be even lower (24%), and it remained constant at the RCE rotation speed varying from 11 to 165 rpm. It is no wonder, since, with the cathode current being registered at this potential and with the nonseparated anode and cathode spaces, the share of the anodic constituent is great (Figs. 5, 6).

Thus, the electrodeposition of cobalt from the citrate solution at low current densities is accompanied by the electrodeposited layer corrosion with the oxygen depolarizing, due to which a significant decrease of the electrodeposition current efficiency takes place. It is evident that the current efficiency should increase at the potential shift to the cathode region (current density increase), since the influence of the corrosive processes will be diminished.

Hydrodynamics and Electrolyte pH Effect on the Cobalt Deposition Rate

Figure 7 illustrates the current–time dependences for the RCE at the rotation speed of 165 rpm (Re = 685) for the citrate solution being studied at pH = 4 and pH = 7 at the separated anode and cathode spaces under the potentiostatic conditions (the potential equals –1.0 V).

There are at least three peculiarities of the obtained dependences. The first one consists in the fact that the achievement of the current's stationary value is observed after applying a considerable amount of electricity. For example, for the electrolyte with pH = 4, after applying about 5 C/cm^2 with 70% current efficiency, it is relevant to the layer thickness on the order of 1 μm (Fig. 7). The second one consists in the significant influence of the pH on the deposition rate. At equal rotation speeds and a fixed potential, the electro-

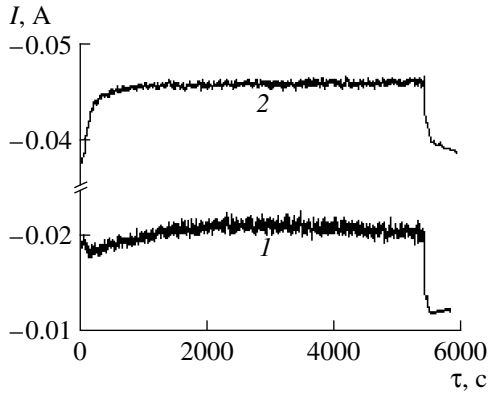

Fig. 7. The dependence of the cobalt electrodeposition current from electrolyte II at pH = 7 (*1*) and pH = 4.4 (*2*) on time in the potentiostatic conditions (E = –1.0 V) at the RCE rotating at a speed of 165 rpm (Re = 685) in a cell with separated anode and cathode spaces.

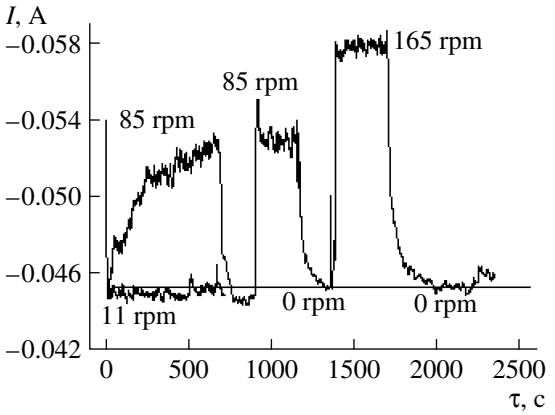

Fig. 8. The dependence of the cobalt electrodeposition current on the time in the potentiostatic conditions (E = –1.0 V) in electrolyte II with pH = 4.4 for the RCE rotating at various speeds of rotation in a cell with separated anode and cathode spaces.

lyte current density with pH = 4 increases more than twofold at one and the same cobalt concentration in the solution. Finally, the third one consists in the presence of the chaotic current oscillations, which confirms, on the one hand, the RCE turbulent character of the flow at the Re numbers being used and, on the other hand, it points to the presence of a concentration limit of the deposition rate. As is shown, for example, in [24], it is the presence of the chaotic current oscillations at a turbulent mode of the flow that is considered to be the qualitative characteristic of the diffusion rate limitation in the electrochemical process.

The results represented in Fig. 8 clearly demonstrate the rotation speed influence on the deposition current density. In this figure, it is shown by how much the current value increases versus the RCE rotation speed growth. One can see that, until the rotation speed reaches 11 rpm (i.e., until Re ~ 50), the rate of stirring produces no effect on the current value (the current density value).

Attention should be paid as well to a certain peculiarity of the observed dependences. After the potentiostatic mode is on, a sharp current drop is detected, and, only after applying a current quantity of about 5 C/cm^2 (see also Fig. 7) is the stationary current value reached. The obtained results allow one to assume that the concentration limits of the deposition rate are not the only reason for the rate limitation of the process. Actually, immediately after the current (potential) mode is on, there arises a considerable barrier to the current flow, and the establishment of a stationary diffusion limited current is found to be reached only after the formation of a fairly thick layer of the coating.

The dependence "stationary current density–potential" in this region of potentials is linear in the coordinates *i*–*E* (Fig. 9). In other words, the most probable reason for the limitations is the formation (at the initial moment of the deposition) of a film, the charge transfer through which has an ohmic nature.

In this region of potentials, the current efficiency increases with the current density (the potential) growth and attains more than 70%, which is considerably higher than at the neutral medium deposition. Thus, the pH decrease to pH ~ 4 leads not only to the increase of the deposition current density but also to the growth of the current efficiency (Fig. 9). This can be reasonably explained by the fact that the current density increase causes the decrease of the corrosion processes' contribution.

The data presented in Figs. 7–9 relates to the experiments with the separated anode and cathode spaces. However, the influence of the stirring rate on the deposition current density occurs in the case of nonseparated electrode spaces as well (Fig. 10). It should be noted

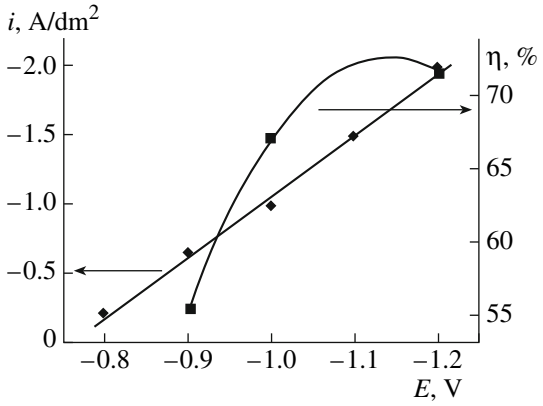

Fig. 9. The dependence of a stationary value of the electrodeposition current density and the current efficiency on the potential of the RCE rotating at a speed of 165 rpm in electrolyte II at pH = 4.4 in a cell with separated cathode and anode spaces.

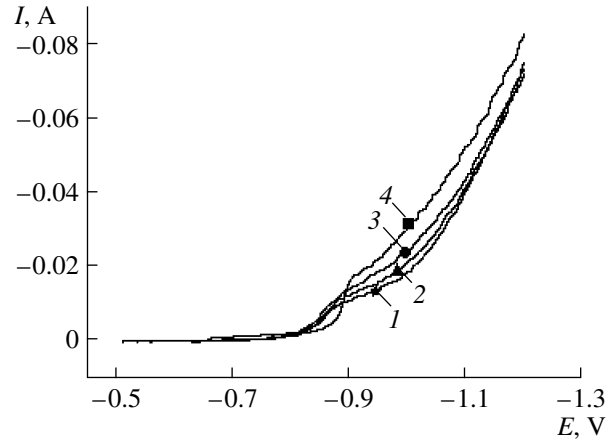

Fig. 10. Voltamperograms obtained from electrolyte II with pH = 6.7 at the potential rate change of 1 mV/s in a cell with nonseparated anode and cathode spaces at the following RCE rotation speeds (rpm): 11 (*1*), 45 (*2*), 85 (*3*), 165 (*4*).

that, for the sake of a more distinct picture, there were removed the anode oscillations in Fig. 10, the origin nature of which was discussed above.

The Morphology of the Electrodeposited Surfaces

It was remarked above that the solution pH change provokes a cardinal modification of the composition of the cobalt citrate complexes being formed, which, in turn, changes the electrodeposition rate. In the acidic solutions, the rate of the deposition (together with the current density and the current efficiency) is considerably higher than in the neutral ones at one and the same cobalt analytic concentration. A lower deposition rate in the neutral medium leads to the formation of more compact coatings (Fig. 11). In the acidic medium, the coatings are found to be more incoherent (Fig. 12). At the same time, the degree of "compactness" is enhanced with the cathode potential increase (Figs. 11, 12).

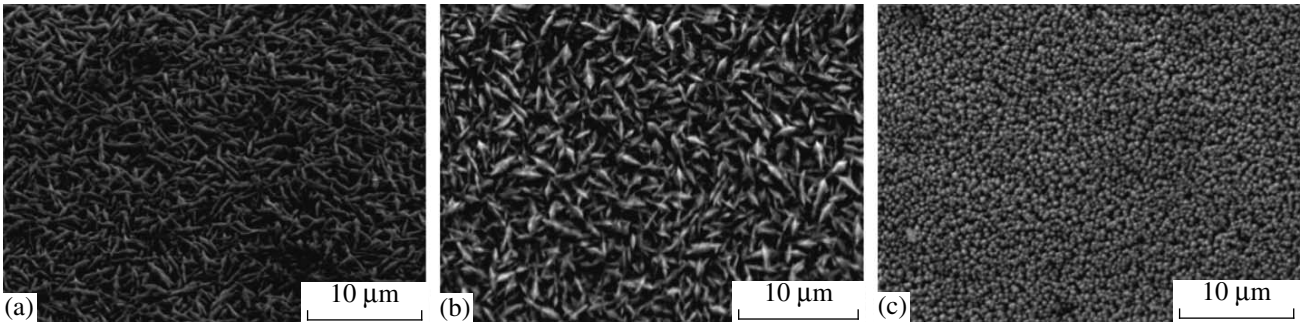

Fig. 11. Images of the RCE surfaces obtained by the scanning electron microscopy after the electrodeposition from electrolyte II at pH = 7 in a cell with nonseparated anode and cathode spaces at a rotation speed of 85 rpm and the following potentials (V): –0.95 (a); –1.0 (b); –1.05 (c).

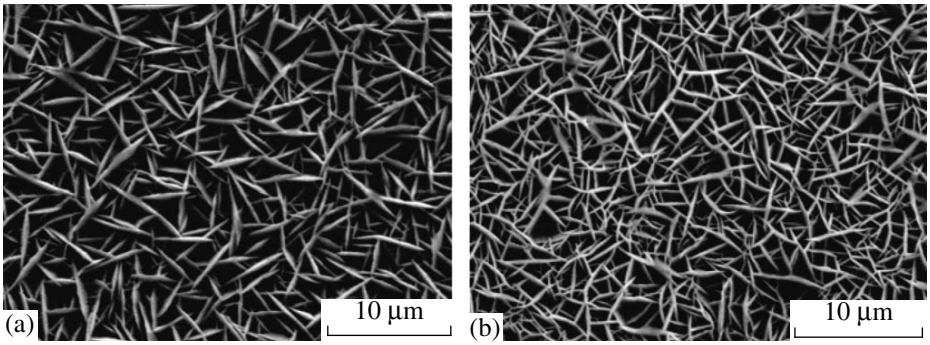

Fig. 12. The RCE pictures of the surfaces obtained by the scanning electron microscopy after the electrodeposition from electrolyte II at pH = 4.4 in a cell with separated anode and cathode spaces at a rotation speed of 165 rpm and the following potentials (V): –1.0 (a); –1.1 (b).

CONCLUSIONS

The results of the above experiments show that the composition of the cobalt citrate complexes in the electrolyte for the electrochemical deposition of cobalt–tungsten coatings depends to a great deal on the pH. In the neutral medium (unlike the acidic solutions), the formation of polymer complexes is found to be possible.

The change of the complexes' composition leads to the deposition rates varying in the controllable hydrodynamic conditions. In the acidic solutions, the deposition rate (together with the current density and the current efficiency) significantly exceeds the one observed in the neutral media at the similar RCE rotation speed and the same potential. It was demonstrated that the current efficiency decrease at low densities of the current was due to corrosion upon oxygen depolarization, owing to which in the systems with nonseparated anode and cathode spaces the anodic oxygen liberation may influence the cathode process. There was detected an oscillatory process at the potentials close to stationary and its mechanism is offered.

It is demonstrated that the hydrodynamic conditions' influence (the increase of the deposition current density with the RCE rotation speed growth) is observed only at relatively high Re numbers ($Re \geq 200$), and it takes place at fairly great thicknesses of the electrodeposited layer.

The linear dependence between the current density and the electrodeposition potential suggests the probability of the formation of a film at the initial period of the deposition.

ACKNOWLEDGMENTS

The financing of the research was performed in the framework of the state programs of the Moldova Republic: Electrophysical and Chemical Surface Processes of Micro- and Nanometric Scales; Multilayer Nanostructural Materials Obtained by Electrochemical Methods: The Study of the Tribological, Corrosive, and Magnetic Properties.

REFERENCES

1. Directive 2000/53/EC of the European Parliament and of the Council of 18 September 2000 on End – of Life Vehicle, *Official J. of the Eur. Communities*, 2000, L 269, pp. 34–42.
2. Directive 2002/95/EC of the European Parliament and of the Council of 27 January 2003 on the Restriction of the Use of Certain Hazardous Substances in Electrical and Electronic Equipment, *Official J. of the Eur. Union*, 2003, L 37, pp. 19–23.
3. Weston, D.P., Shipway, P.H., Harris, S.J., and Cheng, M.K., Friction and Sliding Wear Behaviour of Electrodeposited Cobalt and Cobalt-Tungsten Alloy Coatings for Replacement of Electrodeposited Chromium, *Wear*, 2009, Vol. 267, pp. 934–943.
4. Tsyntsaru, N., Belevsky, S., Dikusar, A., and Celis, J.-P., Tribological Behaviour of Electrodeposited Cobalt-Tungsten Coatings: Dependence on Current Parameters, *Trans. Inst. Metal Finish*, 2008, Vol. 86, pp. 301–307.
5. Kublanovsky, V., Bersirova, O., Yapontseva, J., Tsintsaru, N., Belevskii, S. and Dikusar, A., Pulse Electrodeposition of Cobalt-Tungsten Alloys from Citrate Electrolyte on Steel, its Corrosion Characteristics, *Physico-Chemical Mechanics of Materials*, 2007, no. 6, Special Issue, pp. 80–90.
6. Tsyntsaru, N.I., Belevskii, S.S., Volodina, G.F., Bersirova, O.L., Yapontseva, Yu.S., Kublanovskii, V.S. and Dikusar, A.I., Composition, Structure and Corrosion Properties of the Coatings from Co-W Alloys Electrodeposited at Stationary Current, *Surf. Eng. Appl. Electrochem.*, 2007, no. 5, pp. 9–15.
7. Silkin, S.A., Belevskii, S.S., Tsyntsaru, N.I., Shul'man, A.I., Shchuplyakov, A.N. and Dikusar, A.I., Influence of Long-Term Operation of Electrolytes on the Composition, Morphology and Mechanical Properties of Surface Produced at Deposition of Co-W Coatings from Citrate Solutions, *Surf. Eng. Appl. Electrochem.*, 2009, Vol. 45, no. 1, pp. 1–12.
8. Brenner, F., *Electrodeposition of Alloys*, New York: Academic Press Inc., 1963.
9. Vas'ko, A.T., *Elektrokhimiya molibdena i vol'frama* (Electrochemistry of Molybdenum and Tungsten), Kiev: Naukova Dumka, 1977.
10. Podlaha, T.J. and Landolt, D., Induced Codeposition. I. Experimental Investigation of Ni – Mo Alloys, *J. Electrochem. Soc.*, 1996, Vol. 143, pp. 885–892.
11. Madore, C., West, A.S., Matlosz, M., and Landolt, D., Design Considerations for a Cylinder Hull Cell with Forced Convection, *Electrochem. Acta*, 1992, Vol. 37, no. 1, p. 69.
12. Bobanova, Zh.I., Yushchenko, S.P., Yakovets, I.V., and Dikusar, A.I., Dissipating Capacity of Sulfuric Acid Electrolyte of Coppering at Intensive Modes of Electrodeposition, *Electrocemistry*, 2005, Vol. 41, no. 1, pp. 91–96.
13. Bobanova, Zh.I., Yushchenko, S.P., Yakovets, I.V., Yakhova, E.A., and Dikusar, A.I., Determination of Dissipating (Localizing) Capacity of Electrolytes at Electrochemical Treatment by Using the Hull Cells with a Rotating Cylindric Electrode, *Elektron. obrab. mater.*, 2000, no. 6, pp. 4–15.
14. Eliaz, N. and Gileadi, E., Induced Codeposition of Alloys of Tungsten, Molybdenum and Rhenium with Transition Metals, in *Modern Aspects of Electrochemistry*, Springer, New York: 2008, no. 42, pp. 191–301.
15. Silkin, S.A., Tin'kov, O.V., Petrenko, V.I., Tsyntsaru, N.I., and Dikusar, A.I., Electrodeposition of the Co–W Alloys: Role of the Temperature, *Surf. Eng. Appl. Electrochem.*, 2006, no. 4, pp. 7–13.
16. Pyatnitskii, I.V., *Analiticheskaya khimiya kobalta* (Analytical Chemistry of Cobalt), Moscow: Nauka, 1965.
17. Eisenberg, M., Tobias, S.W. and Wilke, S.R., Ionic Mass Transfer and Concentration Polarization at Rotating Electrodes, *J. Electrochem. Soc.*, 1954, Vol. 101, p. 306.
18. Gomez, E., Pellicer, E., and Valles, E., Developing Plating Bath for the Production of Cobalt-Molybdenum Films, *Surf. and Coat. Technology*, 2005, Vol. 197, pp. 238–246.

19. Stability Constants of Metal-Ion Complexes, Section B: Organic Ligands, Douglas D. Perrin (Ed.), *IUPAC Chemical Data Series 22*, Exter: Pergamon Press, 1983.

20. Kotsakis, N., Raptopoulou, S.P., Tangoulis, V., Terzis, A., Giapintzakis, J., Jakuch, T., Kiss, T., and Salifoglou, A., Correlations of Synthetic, Spectroscopic, Structural and Speciation Studies in the Biologically Relevant Cobalt(II)–Citrate System: The Tale of the First Aqueous Dinuclear Cobalt(II)–Citrate complex, *Inorg. Chem.*, 2003, Vol. 42, p. 22.

21. Murrie, M., Teat, S.J., Stoeckli-Evas, H., and Gudel, H.U., Synthesis and Characterization of a Cobalt(II) Single-Molecule Magnet, *Angew. Chem.*, Int. Ed., 2003, Vol. 42, p. 4653.

22. Hudson, T.A., Berry, K.J., Moubaraki, B., Murray, K.S., and Robson, R., Citrate, in Collaboration with a Guanidinium Ion, as a Generator of Cubane-like Complexes with a Range of Metal Cations: Synthesis, Structures and Magnetic Properties of $[C(NH_2)_3]_8[(MII)_4(cit)_4] \cdot 8H_2O$ (M = Mg, Mn, Fe, Co, Ni, and Zn; cit = Citrate), *Inorg. Chem.*, 2006, Vol. 45, p. 3549.

23. *A handbook on electrochemistry*, Sukhotin, A.M. (Ed.), Leningrad: Khimiya, 1981.

24. Fetter, K., *Elektrokhimicheskaya kinetika* (Electrochemical Kinetics), Moscow, Leningrad: Khimiya, 1967.

ISSN 1068-3755, Surface Engineering and Applied Electrochemistry, 2009, Vol. 45, No. 6, pp. 455–460. © Allerton Press, Inc., 2009.
Original Russian Text © F.Kh. Burumkulov, P.V. Senin, S.A. Velichko, V.I. Ivanov, P.A. Ionov, M.A. Okin, 2009, published in Elektronnaya Obrabotka Materialov, 2009, No. 6, pp. 22–29.

ELECTRICAL SURFACE TREATMENT METHODS

The Properties of Nanocomposite Coatings Formed on a Steel 20H Surface by Means of Electrospark Processing Using Rod-Shaped Electrodes of Steels 65 G and SV 08

F. Kh. Burumkulov, P. V. Senin, S. A. Velichko, V. I. Ivanov, P. A. Ionov, and M. A. Okin

All-Russian Scientific-Research Institute of Farm Equipment Maintenance and Reconditioning Technology, Russian Academy of Agricultural Sciences, pr. 1st Institutskii 1, Moscow, 109428 Russia

e-mail: tehnoinvest-vip@mail.ru

Received August 17, 2009

Abstract—The phase composition, the sizes of the grains (crystallites), the microstructure and microhardness, and the physical and mechanical properties of the nanocomposite coatings on the 20H steel surface resulting from the electrical processing in a gas medium by compact electrodes made of steels 65G and Sv08 with regard to the processing velocity and their influence on the wear resistance of the composition have been investigated.

DOI: 10.3103/S1068375509060039

INTRODUCTION

The surface strength of materials may be improved not only as a result of perfecting their physical and mechanical properties' but also due to modifying their processing with the deposition of protective and strengthening coatings using concentrated sources of energy, e.g., rod-shaped electrode electrospark processing (ESP) in a gas medium.

It is known [1 and 2] that the highest energy concentration in a heated spot is the energy of electric spark pulses used as a metal treatment tool.

According to the data of the Melitopol plant of tractor hydraulic aggregates (MePTH, Ukraine), the ware resource of reconditioned hydraulic control valves of the P75/80 type and the hydraulic system of the wheel- and track-type tractors of over 180 modifications and equipping more than 350 thousand tractors of the MTP, YuMP, T-150, DT-75, KhTP-120 to 3510, and T-4 types is two–six times lower compared to the new ones. Therefore, an urgent problem of the resource conservation is the wear resistance improvement of the reconditioned joint assemblies by means of technologies that provide 100% of the ware resource of the hydraulic control valves after their being reconditioned.

METHODS OF INVESTIGATION

The aim of the present investigation is to study at the surface of steel 20H the phase composition, the microstructure and microhardness, the dimensions of the grains (crystallites), and the physical and mechanical properties of nanocomposite coatings resulting from EST with compact rod-shaped electrodes of 65G and Sv08 steels.

In the present work, the spool landing of the hydraulic valve P-75 was used as the base surface. It is a 25 mm cylinder made of steel 20H (HRC 56–63) that was ESP coated with 65G and Sv08 steels. The choice of the materials was motivated by their practical merits [1].

The electrospark processing was carried out at the turning machine (Fig. 1) by an Elitron-22 device in the fifth energy mode (the discharge energy was $W = 1.66$ J, the number of pulses was $n = 100$ Hz) [1]. The measurement of the coating thickness was performed by a passmeter within accuracy of 2 mm. The mass was measured using an analytical balance (VL-200).

The processed workpiece–cathode for the preset mode of operation rotates at a constant rate. The electrode–anode rotating at a frequency of 50 s^{-1} is brought into proximity with it. After which, the longitudinal feed of the electrode (at rates of 0.08, 0.114, 0.193, and 0.26 mm/rot.) is turned on at the machine.

Metallographic investigations of the specimens' coating were carried out after their being processed at the grinding-and-polishing machine "METKON GRIPO 2V" with a "METAM PB-21" microscope and a "DURAMIN-5" microhardness tester. Triboengineering testing of the friction couple "slide valve–framing" were performed according to the scheme "roller–pad" at a "CMT-1" friction machine in the mode of "on the brink of sticking" and in conditions of the boundary friction according to State Standard 23.224-86 [1].

The properties of the coating were studied by the diffraction method with a "DRON-5M" diffractometer in Cu Kα doublet radiation. The processing of the X-ray spectra was carried out according to the standard program PDW 4.0 (SPA "Burevestnik").

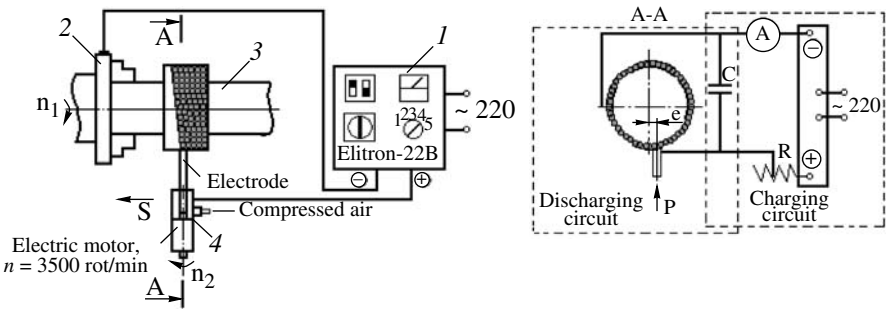

Fig. 1. The principal operation scheme of the experimental device "BIG-3" for reconditioning of cylindrical external surfaces in the mechanized mode. *1*—generator "*Elitron-22B*"; *2*—the chuck of the turning screw-cutting machine; *3*—a processed workpiece; *4*—the machining head.

RESULTS AND DISCUSSION

The results of the measurement of the mass weight gain of the specimens are presented in Fig. 2, which shows that the change of the mass falling within the unit of the processed surface at the velocity variation of the electrode feed is of nonlinear character.

The loss of the mass weight gain of the detail can be explained by the fact that, with the increase of the electrode feed velocity, there occurs the reduction of the time for the work-piece surface processing, or, in other words, within a unit of time, there is performed a lesser quantity of single acts of transfer.

The dependency of the coating thickness (Fig. 3) upon the feed velocity is similar to the mass change (Fig. 2), except that, beginning with the feed velocity of $s \geq 0.114$ mm/rot, the coating layer deposited by the steel 65G electrode becomes thicker than that obtained by the Sv08 steel. The correlation between the coating thickness and the mass weight gain is actually linear, which is indicative of the relative homogeneity (the equality of the average density) of the coating.

The nonlinearity of the correlation between the coating thickness and the electrode feed velocity can be explained by the fact that the dependency of the processing time on the feed velocity has an inverse character. The specimen's mass weight gain decrease with the feed velocity increase leads to the coating thickness reduction.

The X-ray exposure was performed at the specimen's side surface. The distortions of the diffraction picture caused by the specimen's surface irregularity were eliminated by means of the crevices selection.

The X-ray diagrams of the surfaces obtained with the 65G and Sv08 electrode materials are depicted in Fig. 4.

The fluctuation of the background line results from the surface irregularity. The phase structure of the examined coatings corresponds to the α-Fe phase with inclusions of iron oxide Fe_3O_4. The phase of the iron carbide was not detected.

The half-width of the reflections increases with the feed velocity growth (see the table), which is indicative of the increased disordering of the coating structure.

The widening of the reflections resulted from the small sizes of the grains, the distortions of the crystalline structure, and the inhomogeneity and was proportional to $\sec\theta$, $\tan\theta$, and $\sin^2\theta/\cos\theta$, correspondingly, due to which one can distinguish three types of widening. In the present paper, the parameters of the coating

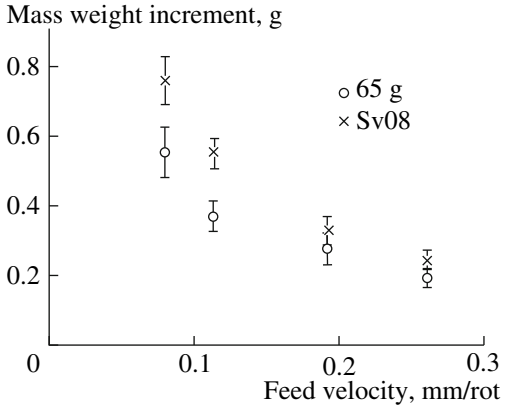

Fig. 2. The specimens' mass varying versus the electrode feed velocity.

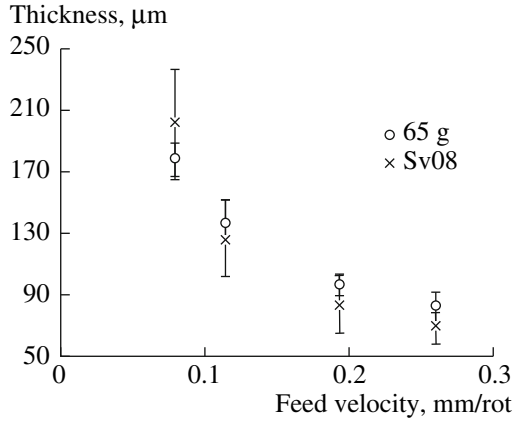

Fig. 3. The coating thickness versus the feed velocity.

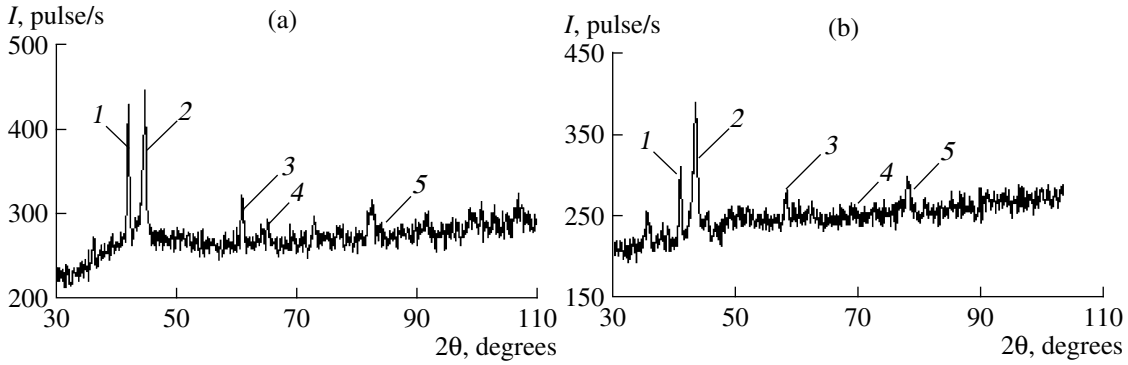

Fig. 4. X-ray diagrams of the coatings obtained at a feed velocity of 0.08 mm/rot. (*1*) and (*3*) are the reflections of iron oxide Fe_3O_4, (*2*) is the reflection (110) of α-iron, (*4*) is (200), and (*5*) is (211). (a) the steel 65G electrode; (b) the steel Sv08 electrode.

substructure were calculated according to lines 110 and 211 of the α-Fe phase [3].

According to the standard technique using the method of approximation, it was defined that, for all the specimens, the relation of the physical widening $\frac{\beta_{211}}{\beta_{110}}$ is less than the relation $\frac{\sec\Theta_{211}}{\sec\Theta_{110}} \cong 5.3$. Hence, the widening itself mainly results from the crystallite dispersion and the coating inhomogeneity [4].

In the diffraction experiment, the average crystallite size is determined by the Warren formula:

$$\langle D\rangle = \frac{K_{hkl}\lambda}{2\cos\theta\beta(\theta)},,$$

where k_{hkl} is the Scherrer constant, the value of which depends on the crystallite form, the domain, and on the indices (hkl) of the diffraction reflection; λ is the X-ray wave length; θ is the X-ray beam tilt angle at the specimen (Bragg's angle); $\beta = \sqrt{(FWHVM_{exp})^2 - (FWHM_R)^2}$ is the diffraction reflection widening; and $FWHM_R$ is the full width of the diffraction line at the half-height, which is measured at a homogeneous specimen with a 1–10 μm size of the particles.

The X-ray diagram analysis (Fig. 4) showed that, with the feed velocity increase, the average size of the grain decreases.

The above effect is characteristic for both of the coatings being examined and is correlated with the reduction of the specimen processing time falling within the surface area unit (the time of the thermal action on the coating being formed is reduced, and the clusters' formation is retarded).

The size of the crystallite clusters irrespective of the electrode feed mode are smaller at the coating formed by the 65G electrode than at the coating deposited by the Sv08 electrode (Fig. 5). This occurs due to the fact that the white layer of the steel 65G coating has a martensitic structure with strengthening phases; therefore, the microtensions in the substance structure are higher than in the coating formed by the Sv08 wire.

In the zone of the electrode contact with the surface of the detail being processed, the discharge temperature attains 10^4 K. Since the specimen is rather massive, there occurs rapid heat transfer from the surface and, hence, there takes place the local hardening of the transferred substance. The process of the coating deposition causes the entire specimen's heating. Later on, it gradually gets cooler down to the room temperature; therefore, there occurs the specimen's drawback.

In order to determine the character of the influence of the structure change on the mechanical properties of the specimens' surface, there were carried out metallo-

Half-width of reflections 110 and 211

Electrode—steel 65G			Electrode—steel Sv08		
feed velocity, mm/rot	half-width 110, degrees	half-width 211, degrees	feed velocity, mm/rot	half-width 110, degrees	half-width 211, degrees
0.080	0.492	0.990	0.080	0.447	0.937
0.114	0.535	1.044	0.114	0.480	1.059
0.193	0.610	1.219	0.193	0.501	1.013
0.260	0.635	1.269	0.260	0.599	0.987

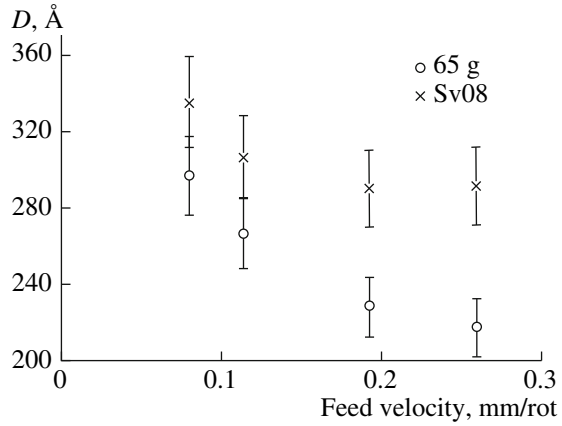

Fig. 5. The dependency of the average size of the crystallite on the feed velocity.

graphic investigations. Figure 6 depicts pictures of transverse metallographic specimens. As follows from Fig. 6, the coating consists of three layers: 1—the deposited layer (the white layer); 2—the thermodiffusion layer; 3—the substrate material (Fig. 7). The thermodiffusion layer's thickness equals 1/2 to 3/4 of the white layer. It is found to originate in the zone of the highest thermal action of the ESP on the substrate.

The coatings are highly irregular and inhomogeneous. In the picture, one can distinctly see the pores and oxides. With the electrode feed velocity increase, the coating becomes less defective.

The white layer's structure changes starting from the coating surface to the diffusion layer, reaching the highest density at its boundary (the light band on the etched specimen). It may be assumed that, due to the concentrated heat source action on the surface of the steels, the boundary areas become enriched by carbon and various defects, and, as a result, there develops ultradisperse structure with 30–200 nm crystallites [5].

As a rule, at the reconditioning of the precision friction couples, the white layer is partially removed by the attrition in (up to 50%) order to make use of the layer of high uniformity characterized by the high bearing capacity and wear resistance.

To determine the value of the microhardness by Vickers at the surface of the transverse metallographic specimen, there were made punctures with a preset step beginning from the edge (Fig. 7). The substrate boundary layer was taken to be the starting point because of its being fairly even and easily observable.

By the fivefold repeating of the measuring and subsequent averaging, the distribution of the microhardness value based on the coating depth was obtained (Figs. 8 and 9).

It was determined that the character of the coating's micrhardness change with regard to the depth is actually similar. For the hardened steels, the coating microhardness from the surface to the substrate actually decreases according to a linear law and reaches its minimum value in the thermodiffusional zone and, then, increases to the initial value of the substrate.

The average microhardness of the diffusion zone coating formed as a result of the 65G electrode processing is 12% higher in comparison with that obtained with the Sv08 electrode. This can be explained by the fact that the Sv08 electrode wire is low-carbon, which accounts for the structure of the diffusion zone being low-carbon also. With the electrode feed velocity increase, the weakened zone shifts into the substrate depth.

The spread in the values of the microhardness (HV) at the left-hand side of zero indicates the considerably disordered structure of the coating. Such a behavior of HV coatings may show that the deposition occurs in a layer-by-layer mode with each subsequent layer being deposited on the previous one. This leads to the annealing (vanishing of the structural defects) of the latter. The annealing also accounts for the microhardness value decreasing in the boundary layer.

Figures 10 and 11 display the character of the dependence of the microhardness value at a distance of 15 and 34 μm from the boundary coating substrate, i.e., the light band at the etched metallographic specimen (Fig. 6), upon the electrode feed velocity.

The analysis of the experimental data shows that the microhardness of the white layer of the highest density during the 65G electrode treatment is found to be

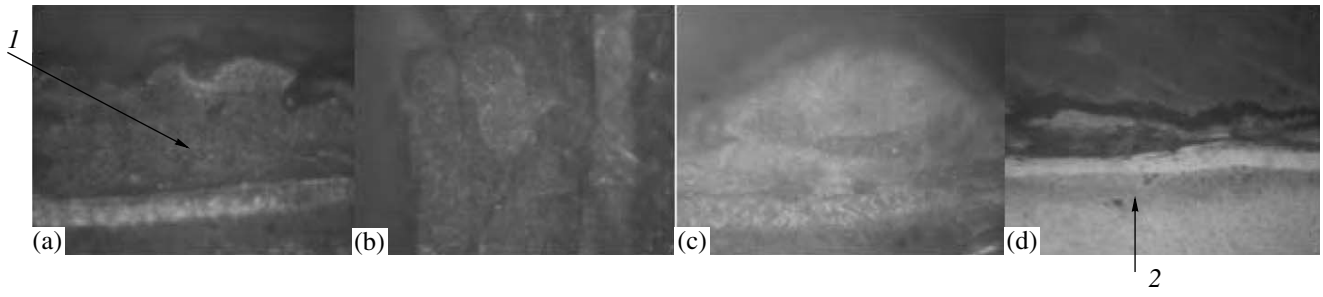

Fig. 6. A picture of the etched transverse specimens with the coatings. (a) and (b) the electrode of steel 65G, the feed velocity is 0.193 mm/rot, ×400; (c) the electrode of steel Sv08, the feed velocity is 0.114 mm/rot, ×300; (d) the electrode of steel Sv08, the feed velocity is 0.193 mm/rot, ×125.

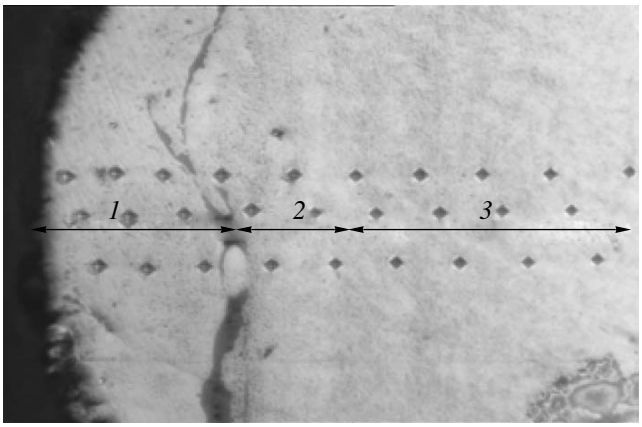

Fig. 7. The picture of the trail of punctures, ×300.

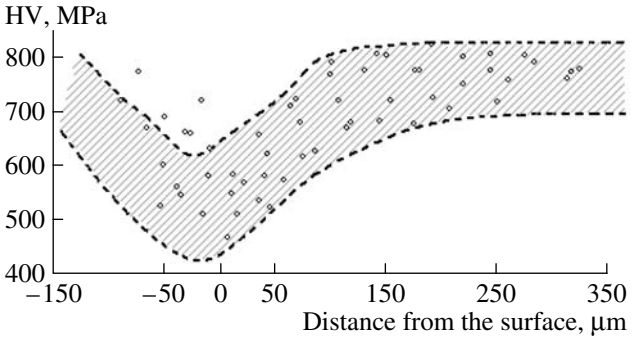

Fig. 8 .The general character of the changes with regard to the depth of the coating microhardness value obtained at the steel 65G coating and feed velocity of 0.08 mm/rot.

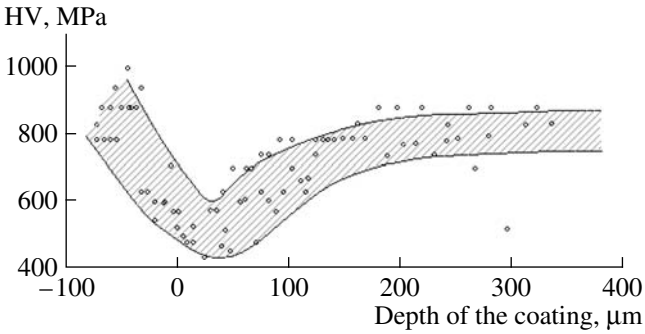

Fig. 9. The general character of the changes with regard to the depth of the coating microhardness value obtained at the steel Sv08 coating and the feed velocity of 0.26 mm/rot.

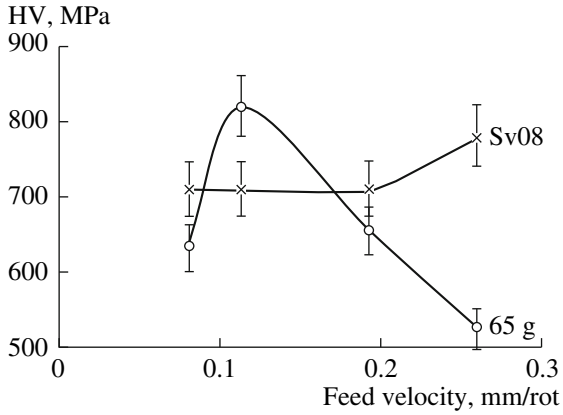

Fig. 10. The dependency of the microhardness value at a distance of 15 μm from the coating–substrate boundary on the feed velocity.

attained at the electrode feed velocity of 0.114 mm/rot (0.26 mm/rot for the Sv08 electrode).

As follows from Fig. 3, the coating's greatest thickness is reached at the electrode feed of 0.114 mm/rot. Therefore, the more preferable technological requirement is the reconditioning of the worn slide valves by the 65G electrode at a feed of 0.114 mm/rot. In this mode of the coating deposition, the average size of the crystallite clusters equals 26 nm (see Fig. 5).

The value of the macrotensions (the remaining tensions) was defined by the method of $\sin^2\psi$ (Fig. 12) [4].

The character of the dependency of the remaining tensions on the feed velocity is nonmonotonic both for the 65G and Sv08 steels, which suggests that the structure formation process in the surface layer is a complicated one. One may assume that, with the decrease of the thermal action time, the mobility of the defects that can penetrate into the upper layers varies in a certain manner.

From Figs. 10, 11, and 12, it follows that, for the coating of steel 65G, with the decrease of the remaining tensions of stretching, the microhardness increases up to its maximum value at the longitudinal electrode feed of s = 0.114 mm/rot. Hence, if a coating is exposed to surface plastic deformation, its microhardness should increase.

The wear resistance of the coatings was determined by the comparison of the wear intensity of the test specimens of steel 20H (HRC 56–63) versus similar specimens after the coating layer deposition by the ESP and grinding in. The triboengineering testing demonstrated that the wear intensity of the friction couple whose rolling element surface is fused with the steel 65G at the electrode feed of s = 0.114 mm/rots is 1.8–2.4 times less than that of the test compound (Fig. 13). This occurs due to the fact that the microhardness of the coating is 1.27 times more than that of the substrate, and the value of the complex irregularity is 2.8 times less as compared to the test rolling element.

In addition, the friction surface of the rolling element is well lubricated due to the presence of recess holes holding the lubricant [1].

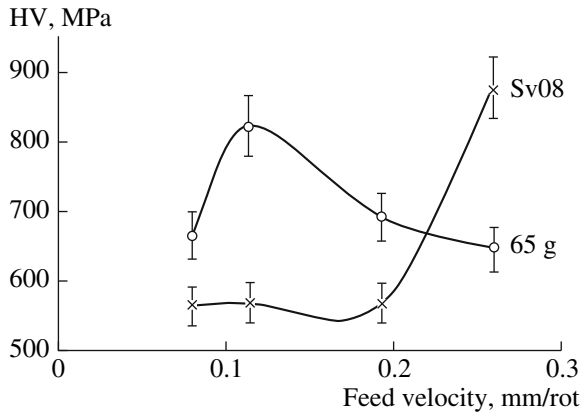

Fig. 11. The dependency of the microhardness value at a distance of 34 μm from the coating–substrate boundary on the feed velocity.

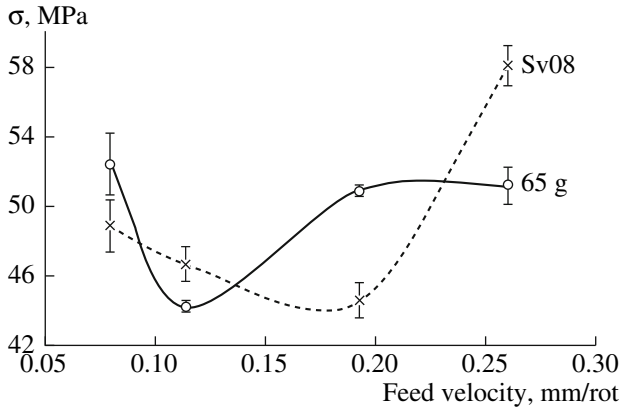

Fig. 12. The dependency of the remaining tensions' value on the feed velocity (the index "+" denotes the stretching macrohardness).

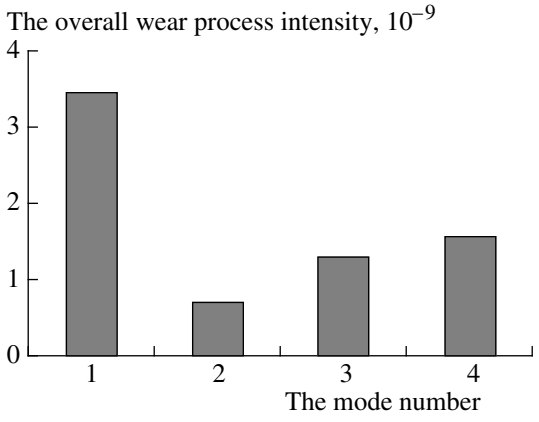

Fig. 13. The dependence of the overall wear intensity of the friction couples. 1—the test friction couple, the rolling element (steel 20H), and the pad (cast iron SCh15); 2, 3, and 4—the friction couples whose rolling element surface is deposited with a steel 65G coating at the electrode feed of 0.114, 0.193, and 0.26 mm/rot, correspondingly.

CONCLUSIONS

(1) The velocity of the longitudinal feed of the workpiece at mechanized ESP leads to the decrease of the mass transfer and the coating thickness due to the reduction of the surface processing time; i.e, a lesser quantity of single transfer events is performed for a given time unit. The average density of the deposited material is constant.

(2) The phase composition of the coatings being examined corresponds to the phase of pure α-Fe with inclusions of iron oxide Fe_3O_4.

(3) With the feed velocity increase, the crystalline structure of the coatings becomes more disordered, which mainly results from the ultradispersiveness of the clusters.

(4) The microhardness dependency with regard to the depth is heterogeneous. The HV behavior in the coating can be explained by the fact that the coating deposition is performed in the "layer-by-layer" mode, and each subsequent layer is deposited at the previous one. This leads to the partial annealing of the latter. The decrease of the microhardness value at the boundary layer occurs due to the annealing.

(5) The dependence of the macrotensions' value (the remaining tensions) upon the feed velocity is nonmonotonic and correlates with the varying microhardness, which is typical of both of the electrode materials.

(6) The wear intensity of the friction couple whose rolling element surface is deposited with steel 65G by means of the ESP at the electrode feed s = 0.114 mm/rot is 1.8– 2.4 times less than that of the test compound.

REFERENCES

1. Burumkulov, Ph.Kh., Lezin, P.P., Senin, P.V., Ivanov. V.I., Velichko, S.A. and Ionov, P.A., *Electroiskrovye tekhnologii vosstanovleniya i uprochneniya detalei mashin i instrumentov (teoriya i praktika)* (Electrospark Technologies of Reconditioning and Strengthening of Vehicle Pieces and Tools (Theory and Practice), Saransk: Krasnyi Oktyabr'", 2003.
2. Mikhailyuk, A.I., Gitlevich, A.I., Rapoport, L.S. et al., The Influence of the Modes of Electrospark Alloying on the Structure and Wear Resistance of Iron, *Elektrich. metody obrab. poverkhnosti*, 1988, no. 4, pp. 10–13.
3. Gorelik, S.S., Skakov, Yu.A. and Rastorguev, L.N., *Rentgenograficheskii i elektronno-opticheskii analiz* (X-Ray and Electron-Optical Analysis), Moscow: Mosk. inst. stali i splavov, 1994.
4. Gusev, A.I., *Nanomaterialy, nanosruktury, nanotekhnologii* (Nanomaterials, Nanostructures, Nanotechnologies), Moscow: PHIZMATLIT, 2009, ed. 2.
5. Burumkulov, Ph.Kh., Okin, M.A. and Ivanov. V.I., The Influence of Physical and Mechanical Properties and the Remaining Tensions of Electrospark Coatings on the Compounds Wear Resistance, *Remont, vosstanovlenie, modernizatsiya*, 2009, no. 3, pp. 17–23.

ISSN 1068-3755, Surface Engineering and Applied Electrochemistry, 2009, Vol. 45, No. 6, pp. 461–464. © Allerton Press, Inc., 2009.
Original Russian Text © Yu.E. Kisel', G.V. Gur'yanov, D.M. Kroitoru, 2009, published in Elektronnaya Obrabotka Materialov, 2009, No. 6, pp. 30–34.

ELECTRICAL SURFACE TREATMENT METHODS

Wear Resistance of Composite Electrochemical Coatings Based on Iron Alloys

Yu. E. Kisel'[a], G. V. Gur'yanov[b], and D. M. Kroitoru[c]

[a]*Bryansk State Academy of Engineering and Technology, pr. Stanke Dimitrova 3, Bryansk, 241037 Russia*
e-mail: ykp2@mail.ru
[b]*Bryansk State Agricultural Academy, Bryansk Region, Kokino, 243365 Russia*
[c]*Institute of Applied Physics, Academy of Sciences of Moldova, ul. Academiei 5, Chisinau, MD-2028 Republic of Moldova*
e-mail: croitoru@phys.asm.md

Received August 25, 2009

Abstract—The influence of the volume content of a solid dispersed phase on the coefficient of variation of the microhardness of composite electrochemical coatings is shown. A theoretical model of the description of the relationship between the volume content of a solid dispersed phase and the coefficient of variation of the microhardness is given.

DOI: 10.3103/S1068375509060040

INTRODUCTION

The deposition of iron-based composite electrochemical coatings (CECs) makes it possible to significantly expand the range of efficient application of the technology due to the considerable improvement in the quality and wear resistance of electrodeposited coatings [1–3]. The selection of an electrolyte for obtaining a CEC matrix and a filler is determined by the scope of the treated components and the conditions of their operation. White alumina micropowders are promising as CEC fillers. Meanwhile, iron-based alloys, which allow improving the physicomechanical properties of CECs, are used as a binding agent [4, 5]. However, data on their operation capability in conditions of abrasive wear are scarce. It is impossible to find the relationship between the mechanical properties of coatings and the conditions of their obtaining on the basis of the available data, which limits the possibilities to select a CEC matrix and to objectively judge the regularities of the behavior of remanufactured components in the course of their operation. At the same time, it has not been determined in a unique fashion which sizes and volume content of particles of the disperse phase (DP) in a coating provide the highest wear resistances of CECs in conditions of abrasive wear. To develop the operating procedure of the deposition of composite coatings on fast wearing components of agricultural equipment, it is necessary to study the influence of DP on the operation capability of CECs and to select the optimum conditions for obtaining of the most wear-resisting base.

Therefore, the aim of this work was to develop a method for the enhancement of the lifetime of fast wearing components of agricultural equipment by means of composite electrochemical coatings based on iron–nickel alloys.

RESEARCH TECHNIQUE

The iron–nickel coatings were obtained from an electrolyte of the following composition, kg/m^3: 500$FeCl_2 \cdot 4H_2O$; 100$NiSO_4 \cdot 7H_2O$; 1.5$Na_2H4C_4O_6 \cdot 2H_2O$. The iron–cobalt deposits were obtained from the following electrolyte, kg/m^3: $FeCl_2 \cdot 4H_2O$—500; $CoSO_4 \cdot 7H_2O$—100; $Al_2(SO_4)_3 \cdot 18H_2O$—80. The electrolysis modes were varied as follows: the electrolyte temperature T ranged from 30 to 80°C; the current density D, from 13.4 to 46.8 A/dm^2; the solution pH, from 0.2 to 1.2. Studies of the steel preparation conditions and the determination of the possibilities to use literature recommendations concerning the anode treatment were carried out in the electrolyte: 300–350 kg/m^3 H_2SO_4 and 20–22 kg/m^3—$FeCl_2 \cdot 4H_2O$ [2]. The influence of the electrolysis parameters on the properties and abrasive wear resistance of the coatings was studied with the use of second-order central rotatable uniform planning at $k = 3$ [6].

The CEC samples were obtained from an iron–nickel electrolyte suspension (ES) containing white alumina DP (M2–M40 grades) in a special bath with a volume of 5 l (Fig. 1). The velocity of the flow of the ES was set on the basis of the recommendations in [2]. The ES flow entered the working part of the bath through the perforated bottom damper. To measure the flow velocity in a separate section, a Venturi-type flow-rate meter with a differential gage was designed and installed. The powder content in the ES was varied from 25 to 150 kg/m^3.

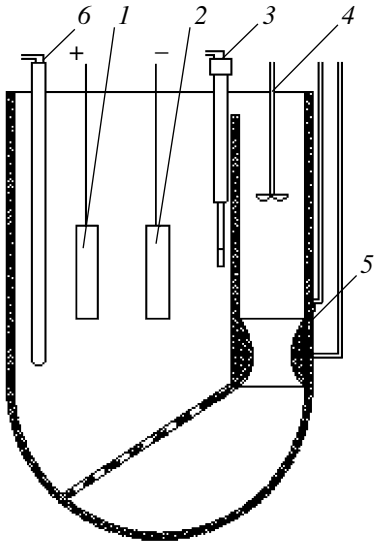

Fig. 1. Bath with a concave bottom and a perforated baffle plate for deposition of CECs: (*1*) depicts the anode; (*2*) the cathode; (*3*) the thermometer; (*4*) the mixer; (*5*) the Venturi flow-rate meter; and (*6*) the contact heater.

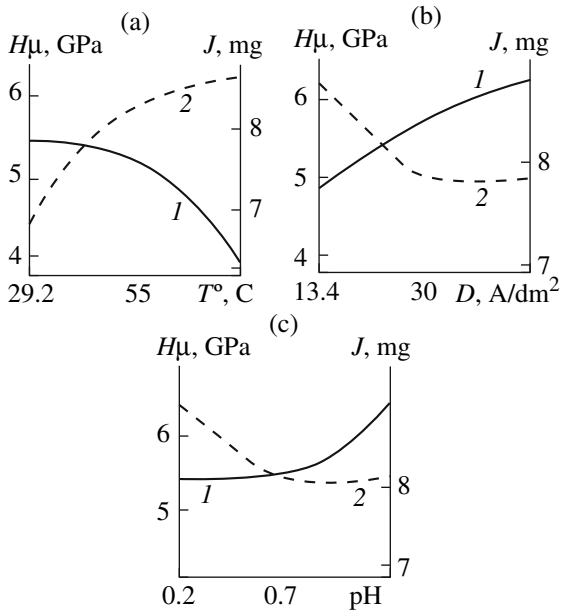

Fig. 3. Influence of the electrolysis modes on the microhardness (*1*) and wear (*2*).

The microhardness of the coatings was determined by means of a PMT-3 microhardness gage according to the State Standard GOST 9450-76. The abrasion tests for friction using loose abrasive particles were carried out according to GOST 23.208-79 by means of an ad-hoc laboratory installation (Fig. 2).

Electrochemical coatings with a thickness of 0.5 ± 0.1 mm were deposited on plates of steel St3 (with a length of 30 mm, a width of 30 mm, and a thickness of 1 mm). The force of the pressing of a sample to a the rubber roller P ranged from 20 to 88 N; the roller revolutions varied from 60 to 325 r/min, which corresponds to the variation of the relative sliding velocity V_{rel} from 0.3 to 0.9 m/s. The time of the tests was governed by the necessity to obtain an appreciable value of the wear J (mg), which was measured by the weight method to a precision of 0.05 mg.

As an abrasive material, we used fluvial sand with a grain size of no more than 1 mm. The comparison standards were samples of quenched steel 65G, which is most commonly used for the production of cutting units of tillage equipment; "pure" iron–nickel; and iron–cobalt coatings.

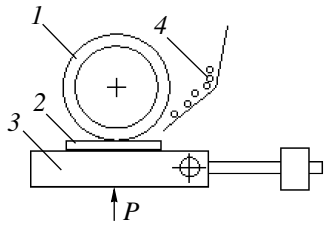

Fig. 2. Diagram of the installation for the abrasion resistance testing of the samples: (*1*) is the rubber roller; (*2*) the sample; (*3*) the support; and (*4*) the abrasive material.

RESULTS AND DISCUSSION

The studies showed that the abrasive wear resistance of the iron–nickel base in realistic conditions depends on the electrolysis parameters. By the regression analysis of factorial experiments, we obtained an empirical relation adequately describing the dependence of the wear of the electrolytic alloys on the electrolysis parameters. After the suppression of the insignificant coefficients, the equation took the following form (X_1 is the temperature, °C; X_2 is the current density, A/dm^2; and X_3 is the solution pH):

$$J_{\text{Fe–Ni}} = 8.8 + 0.95X_1 - 0.6X_3 + 0.69X_3^2 + 0.5X_1X_2 + 0.94X_1X_3 + 0.66X_2X_3.$$

A decrease in the temperature led to an increase in the wear resistance of the coatings; the optimum value of the solution's pH is at the center of the experiment's design (Figs. 3a, 3c). As the current density grew, the wear of the alloys increased and passed through maximum at 35–40 A/dm^2 (Fig. 3b).

Thus, the optimum mode of obtaining of wear-resistant deposits free from inclusions is as follows: the solution pH = 0.7–1.0; D = 35–40 A/dm^2; T = 40–45°C. The adherence to the recommended conditions for the deposition of the alloys allows obtaining deposits with their wear resistance being higher by a factor of 1.5–2 than that of the steel of a commercial plough [7].

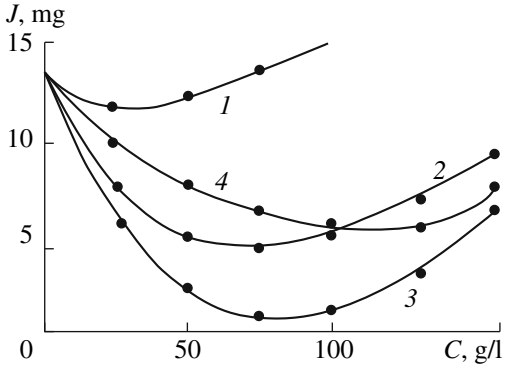

Fig. 4. Influence of the particle content in the electrolyte on the wear rate of the iron–alumina deposits in contact with a loose abrasive material: (*1*) M2; (*2*) M10; (*3*) M14; (*4*) M20.

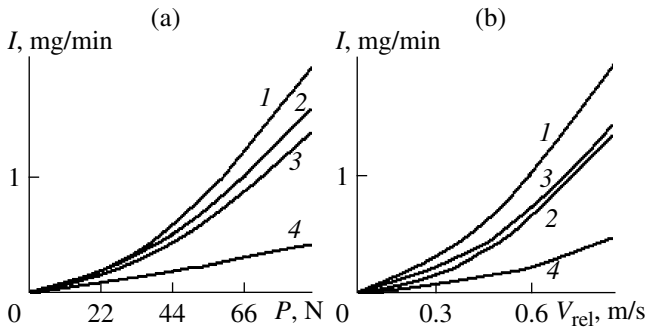

Fig. 5. Influence of the load (a) and relative sliding velocity of the friction pair (b) on the wear rate *I* of the standards and the sample with a CEC: (*1*) stands for quenched steel 65G; (*2*) iron–nickel; (*3*) iron–cobalt; and (*4*) iron–nickel–alumina M10.

The study of the influence of the content and size of the DP on the wear of the coatings revealed that the solid particles of white alumina allow enhancing the wear resistance of the CECs under abrasive wear by a factor of 4–5 as compared to "pure" iron–nickel coatings and by a factor of 8–10 as compared to quenched steel 65G. The highest wear resistance is found in the CECs with the volume content of the DP up to 26–28 vol % deposited from an ES containing micropowder of M14 aluminum oxide in an amount of 80–90 kg/m^3 (Fig. 4).

In the conditions of the operation of the working parts of tillage equipment, the wear takes place most often as a result of repeated plastic deformation–redeformation of the material's surface microvolumes by rolling abrasive grains. It is known that a variation in the sliding velocity and the force of pressing of the rubbing surfaces leads to a change in the mode of interaction between the rubbing surface and the abrasive material from the particles rolling to sliding and microcutting [8].

The analysis of the test results showed that an increase in the load and the relative sliding velocity of the friction pair led to an increase in the wear rate *I* (mg/min) of the standards and samples coated with the CECs (Fig. 5). In addition, the wear of the samples with iron–nickel coatings and the standard of the quenched steel 65G was more severe than that of the CECs. The wear rate of the composite increased linearly with the load, remaining less by a factor of 4 than that of the coatings without the DP and by a factor of 8 than the standard of the quenched steel 65G. The strongest influence on the wear resistance of the CECs was exerted by the relative sliding velocity; as it increased from 0.3 to 0.9 m/s, the wear varied by a factor of 1.5. At V_{rel} = 0.9 m/s, it was higher than the standard of the quenched steel 65G by a factor of 12.

The high wear resistance of the CECs upon the stiffening of the operation conditions can be explained by the circumstance that, in the conditions of the combined wearing-out processes, the solid phase exhibits a considerable resistance to deformations and wear as well as by the fact that, with the particle inclusion, the strength of the binding material increases, although the level of its internal stresses remains relatively high. An increase in the load and the sliding velocity results in an increase in the component of the microcutting and edging of the coating surface by the abrasive particles. The filler particles play the role of contact patches and barriers at the direct destruction of the surface; they distribute the stresses and shift the process of destruction to a polydeformation one. This circumstance leads to a significant increase in the relative wear resistance of the CECs in comparison with coatings without DP.

The field service tests of the plough shares reinforced with CECs showed that their wear resistance is higher by a factor of 1.5–2 than that of commercial plough shares [7]. The iron–nickel and iron–cobalt coatings, as well as the CECs on their basis, exhibited high efficiency in the reconditioning and enhancement of the wear resistance of excavator teeth, hydraulic control valve spools, K-700 friction plates, wrist pins, and lifter bodies of 10D100 and D50 Diesel engines.

CONCLUSIONS

The conditions of obtaining of CECs based on iron alloys with inclusion of white alumina as a filler, which exhibit high wear resistance in conditions of abrasive wear, were found. The introduction of solid particles of M14 grade in a solution of 80–90 kg/m^3 (in a coating of 26–28 vol %) into alloys of electrolytic iron allows increasing their abrasive wear resistance by a factor of 8–10 in comparison with quenched steel alloys and by a factor of 4–5 in comparison with coatings without DP.

REFERENCES

1. Saifulin, R.S., *Neorganicheskie kompozitsionnye materially* (Inorganic Composite Materials), Moscow: Khimiya, 1983.

2. Gur'yanov, G.V., *Elektroosazhdenie iznosostoikikh kompozitsii* (Electrodeposition of Wear-Resistant Composites), Kishinev: Shtiintsa, 1986.
3. Borodin, I.N., *Uprochnenie detalei kompozitsionnymi pokrytiyami* (Reinforcement of Components with Composite Coatings), Moscow: Mashinostroenie, 1982.
4. Gamburg, Yu.D., *Elektrohimicheskaya kristallizatsiya metallov i splavov* (Electrochemical Crystallization of Metals and Alloys), Moscow: Yanus–K, 1997.
5. Vyacheslavov, P.M., *Elektroliticheskoe osazhdenie splavov* (Electrodeposition of Alloys), Leningrad: Mashinostroenie, 1977.
6. Kolemaev, V.A., Staroverov, O.V., and Turundaevskii, V.B., *Teoriya veroyatnostei i matematicheskaya statistika* (The Theory of Probability and Mathematical Statistics), Kolemaev, V.A., Ed., Moscow: Vysshaya Shkola, 1991.
7. Kisel', Yu.E., Enhancement of Lifetime of Fast Wearing Components of Agricultural Equipment by Composite Electrochemical Coatings Based on Iron Alloys, *Extended Abstract of Cand. Sci. (Eng.) Dissertation*, Moscow, 2001.
8. Tenenbaum, M.M., *Soprotivlenie abrazivnomu iznashivaniyu* (Abrasive Wear Resistance), Moscow: Mashinostroenie, 1976.

ISSN 1068-3755, Surface Engineering and Applied Electrochemistry, 2009, Vol. 45, No. 6, pp. 465–470. © Allerton Press, Inc., 2009.
Original Russian Text © A.I. Grigor'ev, S.O. Shiryaeva, 2009, published in Elektronnaya Obrabotka Materialov, 2009, No. 6, pp. 35–41.

ELECTRICAL PROCESSES IN ENGINEERING AND CHEMISTRY

On Electrostatic Instability of a Space-Charged Jet of Dielectric Liquid

A. I. Grigor'ev and S. O. Shiryaeva

Demidov State University, ul. Sovetskaya 14, Yaroslavl, 150000 Russia

e-mail: shir@uniyar.ac.ru

Received May 7, 2009

Abstract—On the basis of the dispersion equation for the nonaxisymmetric capillary waves at the surface of a strongly volumetrically charged cylindrical jet of an ideal incompressible dielectric liquid, it has been found that, for liquids with their dielectric permittivity changed in a wide range of values, there may occur electrostatic instability of the jet's side surface.

DOI: 10.3103/S1068375509060052

INTRODUCTION

The phenomenon of liquid electrodispersion has been extensively used in engineering and technology (see, e.g., [1–6] and the literature presented there). The regularities of the occurrence of the capillary-electrostatic instability and the disintegration of charged jets into drops have been thoroughly examined both experimentally and theoretically [1–6]. Nevertheless, certain problems correlated with the phenomenon in question remained out of scope of the performed investigations. In particular, this concerns the peculiarities of the disintegration into separate drops of jets with a fairly strong charge. This was left out of the considerations of theoreticians, and, as for experimenters [7 and 8], they just mentioned the fact of the peculiar phenomenology of the jet disintegration at high densities of the surface charge, while offering no physical interpretation of the observed phenomenon. According to the experimental data [7 and 8], the strongly charged jets ejected from the top of the meniscus of a liquid at the top of the capillary via which the liquid is supplied into the discharge system diverge in branches, jetting out subsidiary small jets from the side surface (as a tree shoots out its branches), and it is these small jets that disintegrate into drops. The branching of the jet occurs in the form of the chaotic throwing out (from the surface of the major jet at an angle to its axis) of a number of far more thin jets, which disintegrate into fine droplets. The physical explanation for the described picture of the strongly charged jet disintegration is discussed in ref. [9].

It is well-known that, at sufficiently high intensities of the electric field near the surface of an ideally conducting liquid, namely, a spherical drop [10 and 11] or a plane surface, liquids [12 and 13] are exposed to instability with respect to the negative pressure of the electric field: the emitting bulges formed there are called Taylor cones [14]. From the Taylor cones' tops, there are emitted strongly charged thin liquid jets disintegrating into separate droplets, which carry away an excess charge from the liquid surface [15]. It is this kind of mechanism of the excess charge unloading that has been offered in [9] for a jet of an ideally conducting liquid as well at sufficiently high intensities of the electric field near its surface. In the present paper, it is proposed to investigate an opportunity of realization of electrostatic instability near the jet's side surface of a volumetrically charged dielectric liquid.

FORMULATION OF THE PROBLEM

Suppose there is one infinite cylindrical jet with radius R of an ideal incompressible liquid moving along the symmetry axis at a constant velocity U_0 with the mass density ρ, the dielectric permittivity ε_{in}, and the coefficient of the surface tension σ. The medium around the jet is characterized by the dielectric permittivity ε_{ex} and a negligibly small mass density. Let us accept that the jet is charged and that, in the framework of the model of a "freezed-in" charge, it is distributed homogeneously in a volume with μ density with the charge $\eta \equiv \pi R^2 \mu$ falling within the jet length unit.

Since, in the present paper, a finite jet is being considered, in order to simplify the problem, let us use an inertial coordinate system that moves together with the jet at the same velocity U_0.

It is evident that, in such a coordinate system, the field of the velocities of the liquid flowing in the jet $U(r, t)$ can be totally determined by the possible (e.g., having a thermal nature) capillary oscillations of its surface and have a value of the same infinitesimal order as the amplitude of the oscillations. We shall search for the critical conditions of the realization of the instability of the capillary oscillations of such a jet's surface.

All the calculations are to be performed in a cylindrical coordinate system with the *OZ* axis coinciding with the jet's axis of symmetry, ort n_z of which is directed along the velocity vector U_0. In the dimensionless variables, where the jet radius R, the liquid density ρ, and the coefficient of the surface tension σ have been used as the main scales ($R = \rho = \sigma = 1$), the equation of the free surface of the jet exposed to random oscillations of small amplitude can be written as

$$r = 1 + \varepsilon\xi(\varphi, z, t),$$

where ε is the oscillation amplitude ($\varepsilon \ll 1$), and $\xi(\varphi, z, t)$ is the jet's surface disturbance $|\xi(\varphi, z, t)| \sim 1$ caused by the capillary waves at its surface (this time induced by the thermal motion of the liquid molecules).

The mathematical setting of the problem of the calculation of the capillary oscillations of the jet consists of the equations of hydrodynamics and electrostatics (on the assumption that the rate of the liquid's motion is far less than the relativistic one):

$$\frac{\partial U}{\partial t} + (U \cdot \nabla)U = -\frac{1}{\rho}\nabla P; \quad divU = 0.$$

At the jet's surface $r = R + \xi$, there should be fulfilled the following:

—the kinematic boundary condition

$$\left.\frac{dF}{dt}\right|_{F=0} = 0, \text{ and}$$

—the dynamic boundary condition

$$-(P - P_{atm}) + div\vec{n} - P_q = 0.$$

At the jet's axis, the field of velocities U should be limited:

$$r \longrightarrow 0: |U| < \infty,$$

where P_{atm} is the atmospheric pressure; $U(r, t)$, $P(r, t)$ are the field of velocities and the field of pressures inside the jet; P_q is the electrostatic field pressure onto the jet surface, which is calculated from the boundary problem for the electric potentials inside (Φ^{in}) and outside (Φ^{ex}) the jet, respectively:

$$\Delta\Phi^{in} = -4\pi\frac{\mu}{\varepsilon_{in}}, \quad \Delta\Phi^{ex} = 0,$$

$$r = R + \xi; \quad \Phi^{in} = \Phi^{ex}, \quad \varepsilon_{in}\vec{n} \cdot \nabla\Phi_{in} = e_{ex}\vec{n} \cdot \nabla\Phi_{ex},$$

$$r \longrightarrow 0: \quad \Phi^{in} \longrightarrow 0, \quad r \longrightarrow \infty: \quad \Phi^{ex} \longrightarrow 0.$$

Note that, in the model of the dielectric jet, the charge is "freezed-in" inside the liquid, and the surface lacks free charges. Therefore, the dependence of the electric potential Φ upon the time can be totally determined by the changing of the jet's surface form in time, and the dependence upon the spatial variables of the potentials inside (Φ^{in}) and outside (Φ^{ex}) the jet can be obtained from the solution of the electrostatic problem written above.

In addition to the written conditions, there should be fulfilled the requirement of the constancy of the jet segment volume, the length of which equals the wave length λ:

$$\int_{z_0}^{z_0+\lambda}\int_{0}^{1+\xi}\int_{0}^{2\pi} dzrdrd\varphi = \pi\lambda.$$

DISPERSION EQUATION

The solution of the formulated problem can be found by

$$\begin{aligned}
\xi(\varphi, z, t) &= C_1\exp[i(kz - \omega t + m\varphi)];\\
\psi(\vec{r}, t) &= C_2 I_m(kr)\exp[i(kz - \omega t + m\varphi)];\\
\Phi_{in}(\vec{r}, t) &= C_3 I_m(kr)\exp[i(kz - \omega t + m\varphi)];\\
\Phi_{ex}(\vec{r}, t) &= C_4 K_m(kr)\exp[i(kz - \omega t + m\varphi)].
\end{aligned} \tag{1}$$

where $I_m(k)$ and $K_m(k)$ are Bessel's modified functions of the first and second type, m is the azimuthal parameter, and C_j are the indefinite constants. Omitting the procedure of finding the solution described in detail by [6 and 16], let us proceed to writing the dispersion equation of the problem for the azimuthal number $m = 2$:

$$\begin{aligned}
\omega^2 &= g(k)[3 + k^2 + WF(k, \varepsilon_{in}, \varepsilon_{ex})];\\
W &\equiv \omega\mu^2 \equiv \eta^2/\pi;\\
F(k, \varepsilon_{in}, \varepsilon_{ex}) &\equiv \frac{1}{(\varepsilon_{in}g(k) - \varepsilon_{ex}h(k))\varepsilon_{in}\varepsilon_{ex}}\\
&\times [(\varepsilon_{in} - \varepsilon_{ex})^2 g(k)h(k) + \varepsilon_{in}(\varepsilon_{in} - \varepsilon_{ex})g(k)\\
&+ 3\varepsilon_{ex}(\varepsilon_{in} - \varepsilon_{ex})h(k) + 4\varepsilon_{in}\varepsilon_{ex}];\\
g(k) &\equiv 2 + \frac{kI_3(k)}{I_2(k)}; \quad h(k) \equiv 2 - \frac{kK_3(k)}{K_2(k)}.
\end{aligned} \tag{2}$$

The charge parameter W is defined as the ratio of the pressure of the electric field of the self-charge onto the jet's surface to the pressure of the surface tension forces under its cylindrical surface. Since W is expressed by the charge falling within the jet's length unit, and the mathematical formulation of the problem comprises no physical characteristics of the charge transfer, the obtained dispersion equation can also be used for the investigation of the waves at the homogeneously charged surface of an ideally conducting jet when performing the transition to the limit $\varepsilon_{in} \longrightarrow \infty$ in the dispersion equation. In the analysis performed with "physical" precision, the condition $\varepsilon_{in} \longrightarrow \infty$ may be replaced with a weaker one: $\varepsilon_{in} \gg 1$. As a result, the dispersion equation (2) can be applied for the analysis of the elec-

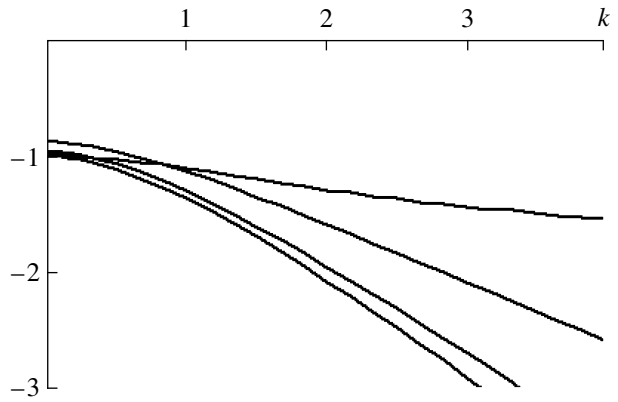

Fig. 1. The dependence $F_\mu = F_\mu(k)$ at $\varepsilon_{ex} = 1$ and various electric permittivities of ε_{in} of the jet. Along the right side from the top to bottom: $\varepsilon_{in} = 1.048$ is liquid helium; $\varepsilon_{in} = 5$; $\varepsilon_{in} = 20$; $\varepsilon_{in} = 80$.

trostatic instability of the jet's side surface with any final electroconductivity.

ANALYSIS OF THE OBTAINED RESULTS

From dispersion equation (2), it follows that, since the multiplier $g(k)$ is always positive, regardless of the value of the parameter W, the jet surface is stable with respect to the virtual wave deformations with $m = 2$ when the expression enclosed in square brackets on the right hand side of the dispersion equation is positive. The appearance of the complex solutions of the dispersion equation relevant to the unstable waves is correlated with the passage of the right hand side of the dispersion equation crossing zero to the negative values' region, which is possible at $F\mu(k, \varepsilon_{in}, \varepsilon_{ex}) < 0$ and at fairly large values of the parameter W when the following correlation is fulfilled:

$$W \geq \frac{3 + k^2}{|F(k, \varepsilon_{in}, \varepsilon_{ex})|}. \quad (3)$$

From Fig. 1, it is evident that the function $F\mu\,(k, \varepsilon_{in}, \varepsilon_{ex})$ is always negative and, to accomplish the electrostatic instability, it is enough for the charge parameter to satisfy correlation (3). In this case, the dispersion equation will have two imaginary complex conjugate roots. The positive sign root nearby the imaginary unit will correspond to the occurrence of the spiral wave disturbances with $m = 2$ at the jet's surface. The amplitude of such disturbances will exponentially increase with time, and, from their tops, there will be thrown daughter jets disintegrating into separate drops in absolute compliance with the theory of refs. [6 and 9] and the data of the experiments of refs. [7 and 8].

Figure 2 illustrates the dependences of the frequency squared on the wave number of the wave at the jet sur-

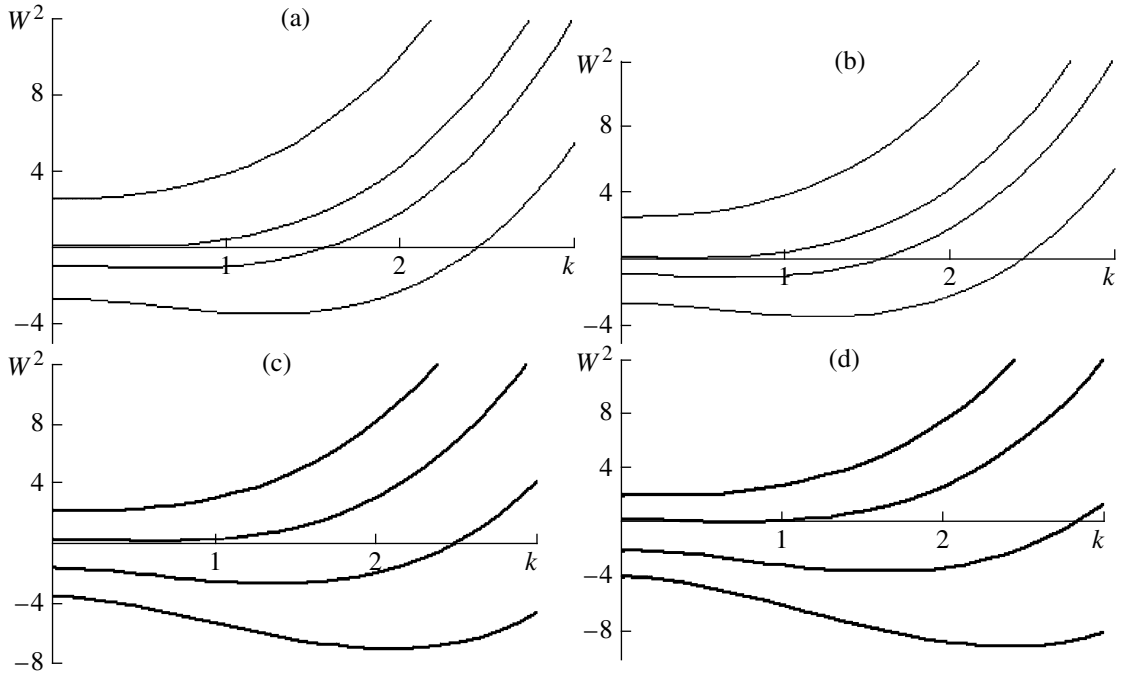

Fig. 2. The dependence of the frequency squared on the wave number of the wave at the jet surface calculated at $\varepsilon_{ex} = 1$ for the following: (a) $F_\mu = 1.048$, $W = 2$, $W = 3$, $W = 4$, $W = 5$; (b) $F_\mu = 5$, $W = 2$, $W = 3.41$, $W = 4$, $W = 5$; (c) $F_\mu = 20$, $W = 2$, $W = 3$, $W = 4$, $W = 5$; (d) $F_\mu = 80$, $W = 2$, $W = 2.89$, $W = 4$, $W = 5$.

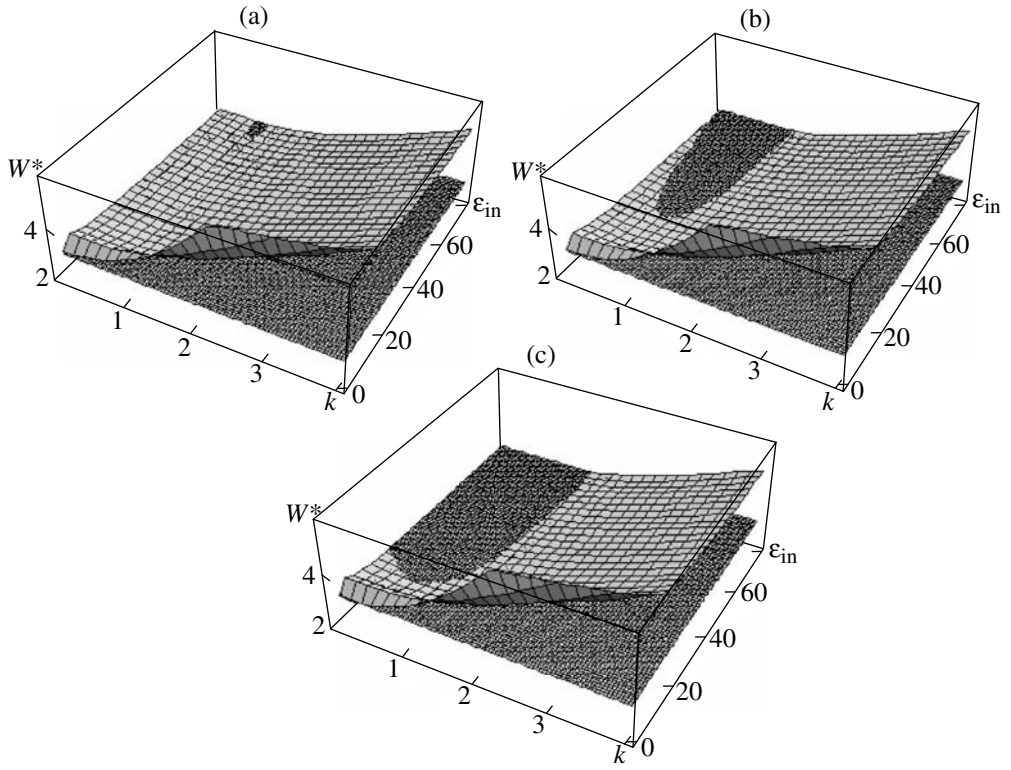

Fig. 3. The surface that determines the location of the boundaries of the realization region of the jet's electrostatic instability within the space of the parameters $\{k, F_\mu, W\}$ crossed by the plane: (a) $W = 2.955$; (b) $W = 3.04$; (c) $W = 3.13$.

face $\omega^2 = \omega^2(k)$ calculated at $m = 2$ and $\varepsilon_{ex} = 1$ for various values of the liquid dielectric permittivity ε_{in} and the charge parameter W. To the unstable waves with $m = 2$ at the jet surface correspond the states with $\omega^2 < 0$. The curves reaching the X-axis at the specified dielectric permittivity ε_{in} correspond to the critical (for the beginning of the realization) parameter W^*. From Fig. 2, one can see that W^* with the increase of the dielectric permittivity of the liquid changes nonmonotonically; W^* with the increase of ε_{in} initially starts growing a little, attaining, as the calculation shows, its maximum ($W^* \approx 3.52$) at $\varepsilon_{in} \approx 3.1$ and, then, decreases to $W^* \approx 2.89$ at $\varepsilon_{in} = 80$ with the wave number relevant to the point of contact of the curve $\omega^2 = \omega^2(k)$ of the X-axis being increased. For the fixed values of the charge parameter W, the increment value of the most unstable wave and the wave number corresponding to it grow with the increase of the liquid dielectric permittivity ε_{in}. This conclusion is confirmed as well by the calculation results displayed by Fig. 3, which present the surfaces defining the location of the realization region boundaries of the jet's electrostatic instability in the space of the parameters $\{k, \varepsilon_{in}, W\}$ crossed by the plane $W = W_c = \text{const}$. It can be seen from Fig. 3 that the area of the geometrical locus where at a specified W_c the electrostatic instability of the jet's side surface is realized arising at $\varepsilon_{ex} = 1$, $W = 2.89$ into the vicinity of the point $\varepsilon_{in} = 80$ and $k \approx 0.78$ increases with the increase of W_c expanding either side by k and towards the decrease of ε_{in} (at the accepted peak limitation of ε_{in} by the value of $\varepsilon_{in} = 80$). At $W = 3.04$, the left k boundary of the region of the electrostatic instability realization at $\varepsilon_{in} = 80$ obtains the value of $k = 0$. At $W = 3.13$, the front ε_{in} boundary of the region of the electrostatic instability realization obtains the values of $\varepsilon_{in} < 20$. The calculations show that, at $W = 3.25$, the electrostatic instability may be realized already at $\varepsilon_{in} = 10$ in the range of the wave numbers' values of $0 \le k \le 1$.

LIMITATIONS CORRELATED WITH THE DISCHARGE PHENOMENA

The circumstance that the electrostatic instability of the jet's side surface in the wide range of values of the dielectric permittivity of the liquid can be realized at fairly great values of the charge parameter ($2.89 < W < 3.25$) necessitates the researching of the probability of the corona discharge ignition at the jet's surface. More precisely, it is worthwhile to reveal the limitations imposed by the probability of the corona discharge ignition on the jet's radii and the values of the surface tension coefficients of the dispersed liquids.

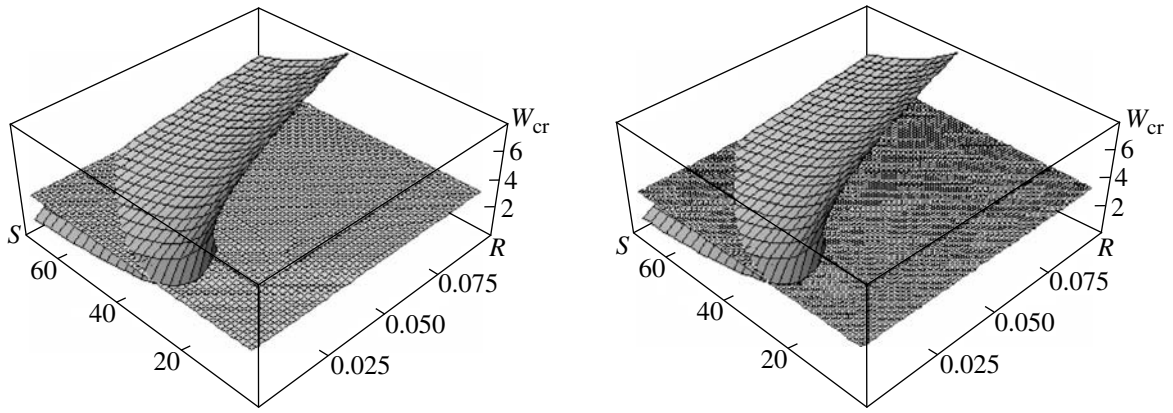

Fig. 4. The dependence of the critical value of the dimensionless charge parameter W_{cr} on the value of the surface tension coefficient of the liquid σ measured in dyne/cm and the jet radius R measured in cm crossed by the plane: (a) $W = 2.955$; (b) $W = 3.13$.

The field intensity at the surface of a volumetrically charged cylinder with the radius R can be determined by the known expression $E \equiv 2\pi\mu R/\varepsilon_{ex}$. As to the corona discharge, in the presence of a smooth cylindrical surface in the air at a normal atmospheric pressure in the radial electrostatic field, it may ignite according to the Peek empirical formula [17] $E_{cr} \approx 31 \times (1 + 0.308/\sqrt{R})$ kV/cm, where R is measured in centimeters.

In the dimensional form, the parameter W is written as $W \equiv \pi\mu^2 R^3/\sigma \equiv E^2 R/4\pi\sigma$. By substituting here the obtained critical value using Peek's formula (for the corona discharge ignition in the vicinity of the R radius jet) of the field intensity, one can find the maximum allowable value of the charge parameter (calculated in the Gaussian system of units):

$$W_{cr} \equiv \frac{\left[31\left(1 + \dfrac{0.308}{300\sqrt{R}}\right)\right]^2 R}{4\pi\sigma}.$$

In Fig. 4, there are presented the calculation results of this relationship in the form of the dependence $W_{cr} = W_{cr}(R, \sigma)$ crossed by the plane W = const. The discharge phenomena at the specified W = const produce no influence upon the development of the hydrodynamic processes at the jet's surface in the geometrical locus where the surface $W_{cr} = W_{cr}(R, \sigma)$ is located higher than the plane W = const and is more significant there, where the surface $W_{cr} = W$cr(R, σ) goes under the plane W = const . From Fig. 4, one can see that, at the charge parameter variation in the range of $2.955 \le W \le 3.13$, the corona discharge at the jet's side surface fails to interfere with the electrostatic instability realization for the jets of liquids with sufficient radii $R > 25$–30 μm in the wide range of variation of the surface tension coefficient value $1 < \varepsilon_{in} < 70$.

CONCLUSIONS

On the basis of the dispersion equation analysis for the nonaxisymmetric capillary waves with the azimuthal number $m = 2$ at the surface of a strongly volumetrically charged cylindrical jet of an ideally incompressible dielectric liquid, it was shown that, for liquids with dielectric permittivilities varying in a wide range of values from $\varepsilon_{in} = 1.048$ for liquid helium to $\varepsilon_{in} = 80$ for water, there may occur the electrostatic instability of the jet's side surface. The discharge phenomena at the side surface of a strongly charged jet correlated with the probability of the corona charge ignition at the jet's surface are essential for thin jets with radii less than ≈25.

ACKNOWLEDGMENTS

This work was performed within the framework of the Topical University Plan and was supported by the Grant of the Governor of Yaroslavl Region, the Russian Education Foundation (project no. 2.1.1/3776), and the Russian Foundation for Basic Research (project nos. 09-01-00084 and 09-08-00148).

REFERENCES

1. Buraev, T.K., Vereshchagin, I.P., and Pashin, N.M., Dispersion Process Investigation of Liquids in the Electric Field, in *Sil'nye elektricheskie polya v tekhnologicheskikh protsessakh* (Strong Electric Fields in Technological Processes), Moscow: Energiya, 1979, no. 3, pp. 87–105.
2. Entov, V.M. and Yarin, A.L., Dynamics of Free Jets and Films of Viscous and Rheologically Complex Liquids, *Itogi nauki i tekhniki, ser. "Mekhanika zhidkosti i gasa",* VINITI: 1984, Vol. 17, pp.112–197.
3. Grigor'ev, A.I., Instability of Charged Drops in the Electric Fields, *Surf. Eng. Appl. Electrochem.*, 2000, no. 6, pp. 3–22.
4. Grigor'ev, A.I. and Shiryaeva, S.O., Capillary Instabilities of the Charged Surface of Drops and Electrodisper-

sion of Liquids, *Izv. Ros.. Akad. Nauk*, 1994, no. 3, pp. 3–22.

5. Grigor'ev, A.I., Shiryaeva, S.O., Voronina, N.V., and Egorova, E.V., On Oscillations and Random Disintegration of Charged Liquid Jets, *Surf. Eng. Appl. Electrochem.*, 2006, no. 6, pp. 15–27.
6. Shiryaeva, S.O., Grigor'ev, A.I., and Volkova, M.V., *Spontannyi kapillyarnyi raspad zaryazhennykh strui* (Random Capillary Disintegration of Charged Jets), Yaroslavl: Izd-vo YarGU, 2007.
7. Cloupeau, M. and Prunet, Foch B., Electrostatic Spraying of Liquids: Main Functioning Modes, *J. Electrostatics*, 1990, Vol. 25, pp. 165–184.
8. Jaworek, A. and Krupa, A., Classification of the Modes of EHD Spraying, *J. Aerosol Sci.*, 1999, vol. 30, no. 7, pp. 873–893.
9. Grigor'ev, A.I., Electrostatic Instability of a Strongly Charged Jet of Electroconducting Liquid, *Zh. Tekh. Fiz.*, 2009, Vol. 79, issue 4, pp. 35–46.
10. Rayleigh, Lord, On Equilibrium of Liquid Conducting Masses Charged with Electricity, *Phil. Mag.*, 1882, Vol. 14, pp. 184–186.
11. Grigor'ev, A.I., On the Mechanism of Instability of a Charged Conducting Drop, *Zh. Tekh. Fiz.*, 1986, Vol. 56, issue 7, pp. 1272–1278.
12. Tonks, L.A., A Theory of Liquid Surface Rupture by Uniform Electric Field, *Phys. Rev.*, 1935, Vol. 48, pp. 562–568.
13. Frenkel', Ya.I., To the Theory of Tonks on Rupture of Liquid Surface by Stationary Electric Field in Vacuum, *Zh. Eksp. Tekh. Fiz.*, 1936, Vol. 6, no. 4, pp. 348–350.
14. Taylor, G.I., Disintegtation of Water Drops in an Electric Field, *Proc. R. Soc.,* London, Ser. A, 1964, Vol. 280, pp. 383–397.
15. Grigor'ev, A.I. and Shiryaeva, S.O., The Laws of Rayleigh Disintegration of a Charged Drop, *Zh. Tekh. Fiz.*, 1991, Vol. 61, issue 3, pp. 19–28.
16. Shiryaeva, S.O., Grigor'ev, and A.I., Levchuk, T.V., On Stability of Nonaxisymmetric Modes of Volumetrically Charged Jet of Viscous Dielectric Liquid, *Zh. Tekh. Fiz.*, 2003, Vol. 73. issue 11, pp. 22–30.
17. Raizer, Yu.P., *Fizika gazovogo razryada* (Physics of Gas Discharge), Moscow: Nauka, 1987.

ISSN 1068-3755, Surface Engineering and Applied Electrochemistry, 2009, Vol. 45, No. 6, pp. 471–479. © Allerton Press, Inc., 2009.
Original Russian Text © I.A. Ashikhmin, Yu.K. Stishkov, 2009, published in Elektronnaya Obrabotka Materialov, 2009, No. 6, pp. 42–51.

ELECTRICAL PROCESSES IN ENGINEERING AND CHEMISTRY

Structural Features of EHD Flows in Wire–Wire Symmetric Systems of Electrodes

I. A. Ashikhmin and Yu. K. Stishkov

St. Petersburg State University, Electrophysics Research and Education Center, Department of Physics, ul. Ulyanovskaya 3, St. Petersburg-Petrodvorets, 198504 Russia

e-mail: Stishkov@paloma.spbu.ru

Received July 21, 2009

Abstract—A computer model of the electrohydrodynamic (EHD) flow on the basis of a complete system of equations in a symmetric wire–wire system of electrodes is presented in this work. Based on this model, three numerical experiments have been carried out for the cases of unipolar injection and symmetric and asymmetric bipolar injection. As a result of the comprehensive analysis of these numerical experiments, it has been found that the structure of the through EHD flow in the case of asymmetric bipolar injection is ideal for the realization of the liquid through pumping in a closed channel necessary for the operation of an EHD pump.

DOI: 10.3103/S1068375509060064

INTRODUCTION

An EHD apparatus represents a classical example of the application of nanotechnologies. In these devices, ions introduced into a liquid are used to transfer an impulse to a neutral medium (this is a way to cause the liquid to move). The actual dimensions of EHD pumps are rather small; the interelectrode gap may be 1 mm. It has been repeatedly noted that the size of the molecular complex set in motion by a single ion is rather big and amounts to 10^{12} molecules. On the one hand, this is associated with the generation of a supermolecular structure in every ion field, the so-called salvation shell, on the other, with the diffusive mechanism of impulse transfer, which is highly efficient at small distances.

The major problem facing the designers of EHD devices is the problem of taking the medium impulse out of the region of the electric field action beyond the boundaries of the interelectrode gap and the liquid delivery through a closed hydraulic circuit to the serviced objects. This problem is mainly associated with neutralization of the impulse source (ions) beyond the interelectrode gap boundaries. With the neutralization not being complete in actual EHD converters, most of the power is utilized for the formation of the so-called internal recurrent vortices, thus reducing the EHD pump's efficiency.

The most widespread EHD pump construction is the nonsymmetrical electrode system of needle-ring (confusor) type proposed by Stuetzer [1]. The nonsymmetrical electrode systems usually used to create EHD pumps have some shortcomings. In such systems, EHD flows are set up in highly nonuniform electric fields with the degree of nonuniformity amounting to quite high values, especially in systems of needle-plate type. Thus, there have been established conditions under which the near-electrode processes at an electrode with a small curvature radius are much more intensive than at the counter electrode. For this reason, in some works, there is postulated the generation of a charge only near the needle electrode (unipolar injection). The authors think that such a system should work in any low-conductivity liquid; that is why an EHD pump is often considered for the pumping of low-conductivity liquids. However, in the case of intense injection, the problem of neutralization of the space charge carriers at the interelectrode gap boundary is stubborn.

As the results show, the charge generation intensity and thus the EHD flow velocity significantly depend on the electrode–liquid boundary properties. It has been revealed [2] that, by varying the composition and concentration of the impurities in the liquid, as well as the material of the electrodes and their coatings, it is possible to control not only the velocity but the direction of the EHD flow and its structure. Tests of classical constructions of EHD pumps of the needle–ring and blade–plate types also revealed the governing influence of the liquid impurity composition on the EHD pump operation [10].

The analysis of the theoretical works on the investigation of the metal–dielectric contact, as well as the metal–electrolyte contact, shows that, in the region under examination, there appears a charged layer caused by the difference of the contacting substances. The electric current passage through the contact layer at the metal–dielectric boundary is attended by electron tunneling through the barrier. The ionization action in the actual solution is a complex heterogeneous process attended by a number of transformations. If a liquid dielectric is described as a good insulating material, its electric properties are determined by impurity mole-

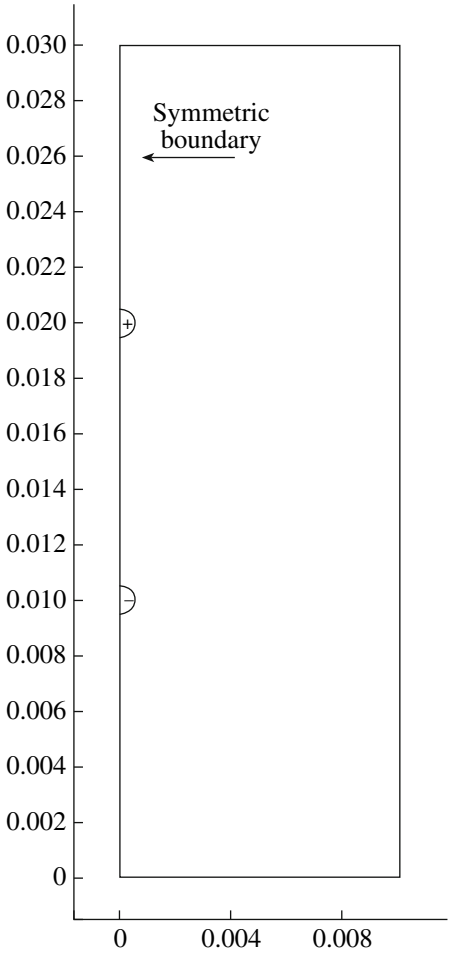

Fig. 1. The model's geometry.

cules with higher electron-donor or electron-acceptor qualities. Thus, it is deemed that the charge transfer at the interface occurs at the impurity molecules.

Following these data, in work [2], it is suggested to introduce the notion of an EHD converter but not a pump, i.e., to recognize the device as a device for the conversion of electric current energy into the working liquid mechanical flow energy using as a working liquid not any low-conductivity liquid but a fluid having a certain set of electrophysical and electrochemical features.

The EHD flow structure and direction are mainly determined by the electrode–liquid contact nature; thus, the liquid electrophysical properties, as well as the electrode–liquid interface features, are the key characteristics of the converter.

The main differences of EHD converters of the electrochemical type from conventional EHD pump constructions are the absence or the secondary importance of the geometrical asymmetry of the electrodes, focusing the action of the electrode system and favoring the elimination of the internal vortices, as well as the use of the electrodes–liquid contact electrochemical asymmetry to produce the pumping.

The electrochemical asymmetry is accomplished by the use of electrodes produced from various materials, the application of various electrode coatings, or the implementation of a working liquid with impurities.

Using symmetrical systems of electrodes, it is possible (rather than to neutralize the charge carriers–ions at the external boundary of the interelectrode gap) to introduce a charge of the opposite sign into the liquid neutralizing the medium space charge. As practice shows, this is much simpler to be realized.

From this viewpoint, the study of EHD flows in a symmetric system of electrodes is highly topical. There are many works dedicated to this subject. Some of them are experimental [3], and some are devoted to computer simulation [9].

SIMULATION

The computer simulation of the process of EHD-flow generation and development in symmetric electrode systems of wire–wire type based on a complete set of EHD equations in the two-dimensional case is the aim of this work. For the first time, the association between the charge generation degree and the local field strength in the near-electrode region has been considered. The variation of the electrode–liquid contact properties allows producing and investigating the different kinds of EHD flows. The results of the computer simulation of the EHD flows for the case of unipolar injection symmetrical to bipolar and nonsymmetrical bipolar injection are presented in this work. The complete set of equations has the following form [2]:

$$\gamma\frac{\partial\vec{v}}{\partial t} + \gamma(\vec{v}, \nabla)\vec{v} = -\nabla p + \eta\Delta\vec{v} - \rho\nabla\varphi; \quad (1)$$

$$\nabla\vec{v} = 0; \quad (2)$$

$$\Delta\varphi = -\frac{\rho}{\varepsilon\varepsilon_0}; \quad (3)$$

$$\frac{\partial c_+}{\partial t} + \mathrm{div}(-D\nabla c_+ - z_+ bFc_+\nabla\varphi) = R - \vec{v}\nabla c_+; \quad (4)$$

$$\frac{\partial c_-}{\partial t} + \mathrm{div}(-D\nabla c_- - z_- bFc_-\nabla\varphi) = R - \vec{v}\nabla c_-; \quad (5)$$

$$\rho = F(z_+c_+ + z_-c_-).$$

Here, ρ is the charge volume density; γ is the substance density; v is the flow velocity; p is the pressure; η is the dynamic viscosity; φ is the electric field potential; ε is the relative permittivity; ε_0 is the vacuum permittivity; D is the diffusion coefficient; F is the Faraday number; b is the mobility; R is the recombination coefficient; c_+, $c-$ are concentrations of positive and negative ions, respectively; and z_+, z_- are the charging numbers.

For the simulation, a system was chosen with symmetric electrodes positioned in the channel with dielectric walls as depicted in Fig. 1. The model comprises

two infinite cylindrical electrodes located in transformer oil. The electrode diameter is 1 mm, and the distance between the electrodes is 1 cm, corresponding to the parameters of the experimental installations. As the model has a vertical axis of symmetry, only half of the model was built and the corresponding boundary conditions were preset on the symmetry axis.

BOUNDARY CONDITIONS

(1) For the Poisson equation, the constant potential value is +10000 V and 0 V on the upper and lower electrodes, respectively. The symmetry condition $n = 0$ is preset at the symmetric boundary. The condition of screening of the electric field by the surface charge is set at the outer upper and lower boundaries.

(2) For the Navier–Stokes equation, the condition of adhesion $\vec{u} = 0$ is prescribed on the electrodes. At the symmetric boundary, we have the condition that the normal velocity vector component $\vec{n}\vec{u} = 0$ is absent. On the outer side of the upper and lower walls, there is the condition of the open boundary:

$$[-p\hat{I} + \eta(\nabla\vec{u} + (\nabla\vec{u})^T)]\vec{n} = 0. \quad (6)$$

(3) The Nernst–Planck equation. As for the foregoing equations, the symmetry condition is prescribed at the symmetric boundary and the condition of the "convective flux" $\vec{n}(-D\nabla c - zbFc\nabla\varphi) = 0$ is set on the walls.

At the electrodes–liquid boundary, there is prescribed the ion flow dictated by the following considerations. As the current passage through the liquid dielectric is not usually attended with dissolution of the electrodes or with the release of substances, it is assumed that the elementary act of the ion generation proceeds through an oxidation–reduction mechanism:

—cathode Ox + e = Red;

—anode Red – e = Ox.

The metal-contact boundary current on the cathode is determined by the difference between the work of the yield from the metal surface and the oxidized form electron affinity energy, and on the anode by the difference between the reduced form ionization energy and the work of the yield from the metal surface.

The reactions of ion generation on the anode and cathode are not the same. It is known that the ejection of an electron from a molecule is energy consuming and characterized by the ionization potential. For instance, when molecular iodine is used as an impurity, the energy of ionization of an iodine molecule into a positive ion ($J_2 - e \longrightarrow J^+$) is 9.7 eV. At the same time, the attachment of an electron to an atom or molecule can occur with the liberation of energy. In this case, it is said that the particle possesses electron affinity. The Electron affinity measure is the energy E_{af} liberated at the ionization of the molecule into a negative ion. For an iodine molecule $E_{af} \approx 3.2$ eV; for the –OH, –CN, and $-NO_2$ groups, the E_{af} is 2, 3, and 3 eV, respectively. In the context of the ionization–recombination mechanism, the introduction of the impurity molecules of halogens, as well as of molecules containing the –OH, –CH, and $-NO_2$ groups, possessing electron affinity into the liquid should cause the intensification of the ion generation processes on the cathode.

The assay of theoretical works on the study of the metal–dielectric contact, as well as the metal–electrolyte one, shows that there appears a charged layer in the examined region caused by the difference of the work of the yield from the contacting substances. The electric current passage through the contact layer at the metal–dielectric boundary is attended with the tunneling of electrons through the barrier. The ionization action in the actual solution is a complicated heterogeneous process attended by a number of transformations. If the liquid dielectric is characterized as a good insulating material, its electric features are determined by the impurity molecules possessing high electron-donor or electron-acceptor qualities. Thus, it is assumed that, at the phase boundary, the charge transfer occurs only to the impurity molecules.

As in most cases when the composition of the impurity molecules determining the ion generation on the electrodes is unknown, we use the dependence according to the formula of Schottky [6]:

$$\vec{J} \sim A\exp\left(B\sqrt{\left\|\vec{E}\right\|}\right)H(t)\vec{n}, \quad (7)$$

however, the coefficients A and B are chosen in such a way that the integral current corresponds to the experimental data. For this purpose, after the model is built, a series of trial calculations are carried out and the value of the parameter A is found at which the flow rate has the same order as in the experiment. The value of the parameter B is selected in such a way that, under steady conditions, there is no flow upward; i.e., the flow structure is the same as is observed in the experiment.

The introduced function $H(t) = 1 - \exp\left(-\frac{t}{t_0}\right)$ is necessary in order that the solution converges at the initial stages. The value $t_0 = 2$; i.e., it can be said that the current switching on proceeds smoothly within 2 seconds.

THE SIMULATION RESULTS AND THEIR DISCUSSION

It is shown that, in the case of unipolar injection, there appears a charge lock hindering the through pumping. In the case of symmetrical injection, there is no through pumping but charge accumulation is also absent; i.e., there is a charge neutralization region centrally located in the IEG. In the case of nonsymmetric injection, a through flow with the charge neutralization region outside the interelectrode gap can be relized.

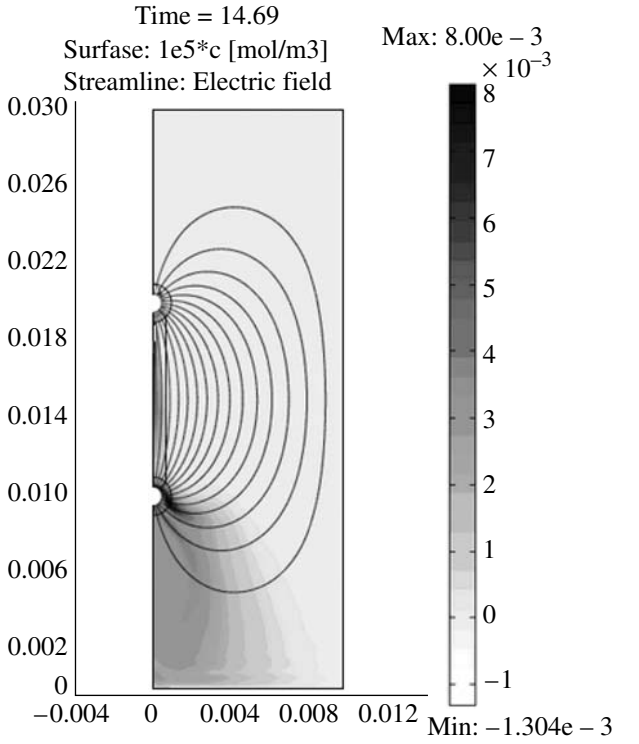

Fig. 2. Distribution of the electric charge volume density and the electric field lines.

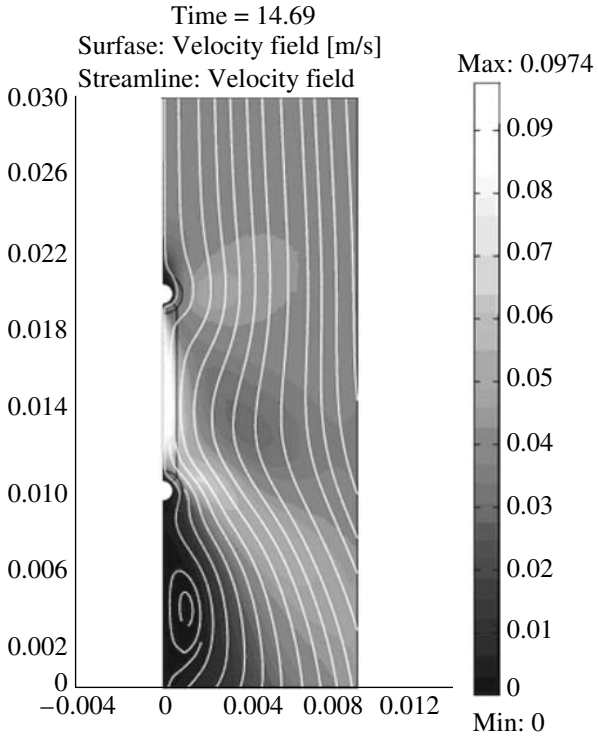

Fig. 3. Outline diagram of the velocities in the model. The white lines are the liquid streamlines.

The distribution of the electric charge volume density and the electric field lines are presented in Fig. 2; the velocity diagram and the liquid streamlines at unipolar injection from the upper electrode are shown in Fig. 3. In the interelectrode gap, the EHD flow is typical: a nearly immobile charged ring round the active electrode and a thin charged jet spreading up to the passive electrode having a short area of acceleration and a long area of uniform flow. However, though there is no obstacle in the form of a wall, after the passive electrode moves around the charge lock (Fig. 2), a recurrent vortex (Fig. 3) hindering the liquid through pumping occurs behind the electrode. This is connected with the complicated mechanism of the ion neutralization on the passive electrode's surface. In some works, there are proposed various variants of constructions to intensify the process of the ion neutralization on the passive electrode's surface [2].

We consider the distribution of the main characteristics of the flow with unipolar injection along the streamlines. The streamlines are selected as is depicted in Fig. 4.

Such distributions allow better understanding of the EHD-flow dynamics. For this purpose, we will construct and analyze the distribution of the electric force and the velocity module along these streamlines.

It is seen from the obtained distributions for the electric force and velocity that there is an area of vigorous acceleration between the electrodes due to the Coulomb force and then the deceleration of the liquid occurs. Electric forces also take part in the deceleration of the liquid behind the passive electrode. In addition, it is observed that, behind the passive electrode, the charge is not eliminated but accumulates. As is seen from the diagrams, this substantially reduces the velocity in the behind-the-electrode area.

Thus, in our opinion, it is the most profitable to introduce an opposite sign charge from the passive counter electrode surface into the liquid but not to neutralize the exhausted charge. In this case, the opposite sign charges when mixing neutralize the medium in the behind-the-electrode region.

In this case, the main task is the accurate balancing of the charge generation processes on each electrode. In a full-scale experiment, it can be achieved by the selection of the contact features: the cathode-impurity admixture and the anode-impurity admixture. The charge generation from the cathode can be intensified by the introduction into the liquid of impurities possessing a high electron affinity or by the production of electrodes from materials with a lesser work yield. The charge generation process on the anode can be intensified by the introduction of impurities with a reduced ionization energy. In the numerical experiment, it will suffice to select the coefficients A and B in boundary condition (2.2).

Using the same coefficients in (2.2), the solution appears in the form of counter oppositely charged currents

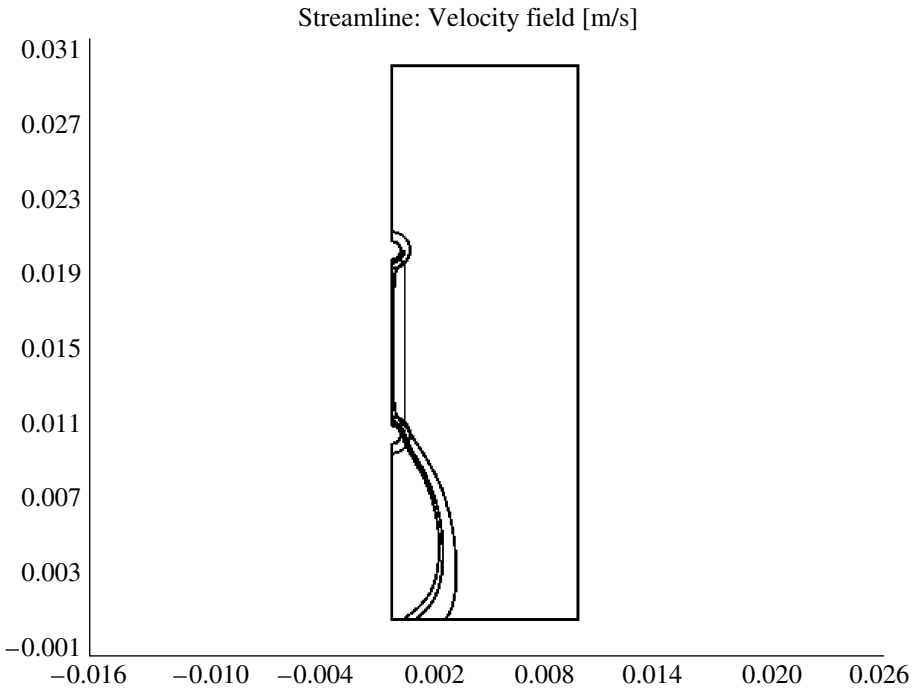

Fig. 4. Streamlines along which the unipolar flow characteristics are examined.

(Figs. 7 and 8). It is seen that the compensation of the counter charges occurs in the middle of the interelectrode gap, where oppositely charged jets meet. The through pumping is almost absent, yet there is no charge accumulation as well. For through pumping, it is necessary to change the charge generation conditions on one of the electrodes, for instance, on the cathode.

Let us consider the problem solution results obtained at the following injection currents: the anode

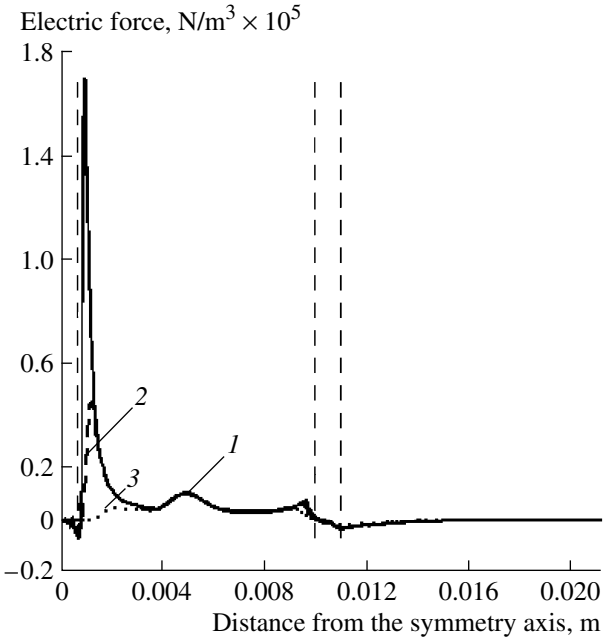

Fig. 5. Coulomb force distribution along the streamlines. *1*—0.6; *2*—0.7; *3*—1 mm.

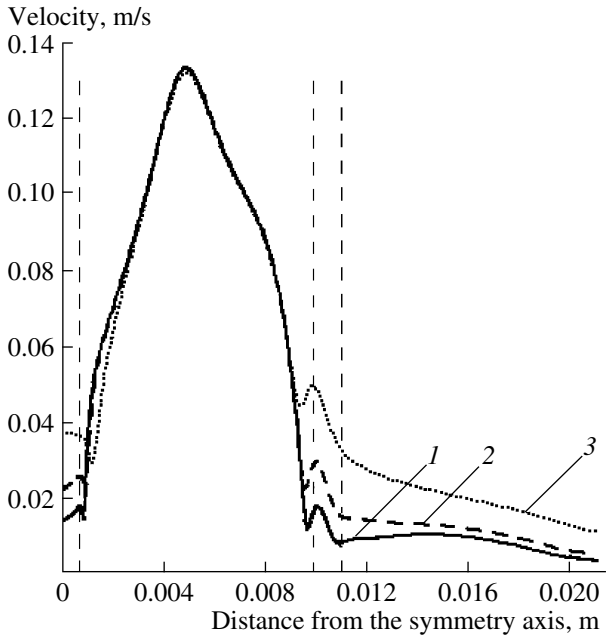

Fig. 6. Distribution of the velocity module along the streamlines. *1*—0.6; *2*—0.7; *3*—1 mm.

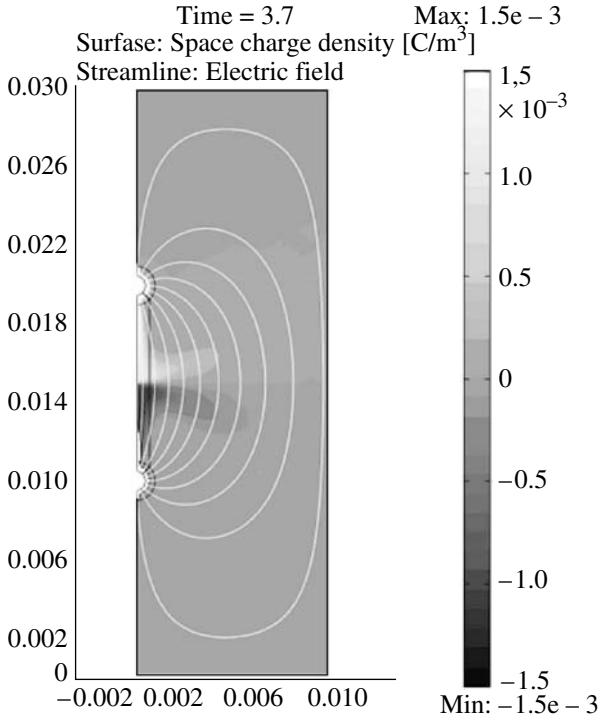

Fig. 7. Distribution of the charge density and the electric field lines at symmetric flow.

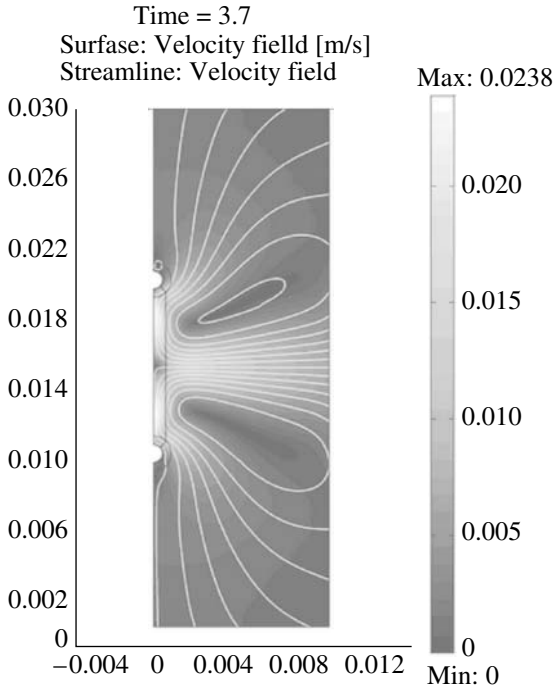

Fig. 8. Distribution of the velocities and streamlineslines at symmetric flow.

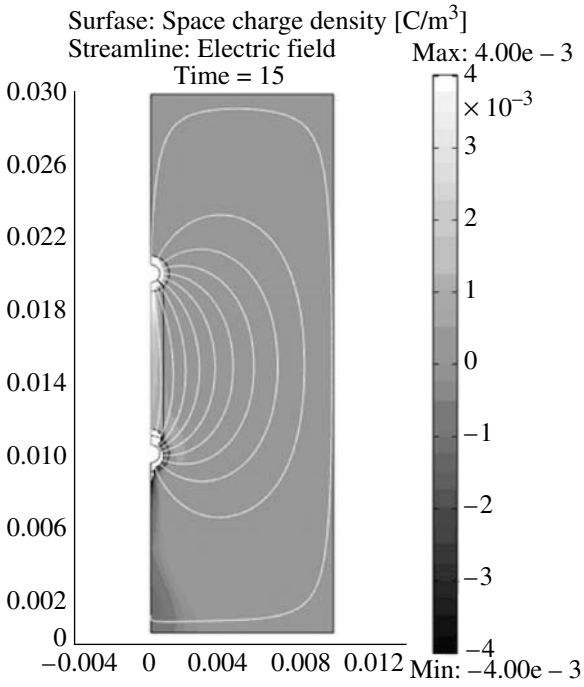

Fig. 9. Distribution of the charge and electric field lines.

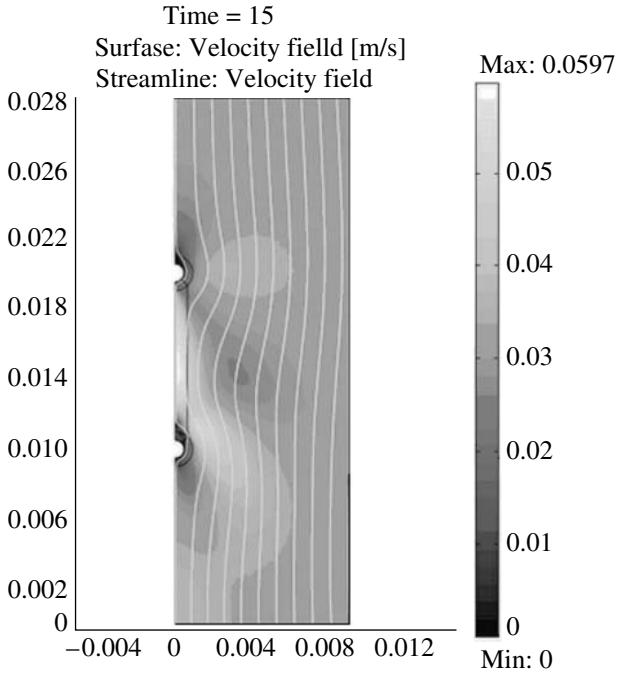

Fig. 10. Outline diagram of the electric field distribution.

$A_+ = 7 \times 10^{-15}$, $B_+ = 7 \times 10^{-3}$; the cathode $A_- = 3.5 \times 10^{-15}$, $B_- = 7 \times 10^{-3}$; the potential difference is 10 kV.

The charge distribution and electric field force lines, as well as the liquid streamlines and the velocity surface diagram, are presented in Figs. 9 and 10. It is seen that the EHD flows in this case occur in the form of two thin charged jets: the positive one spreading "downward" from the upper positive electrode surface and the

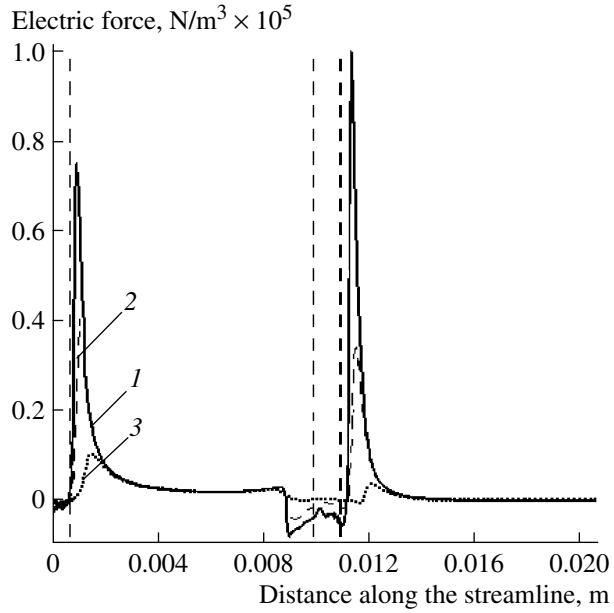

Fig. 11. Diagram of the Coulomb force distribution along the streamlines. *1*—600; *2*—700; *3*—1 mm.

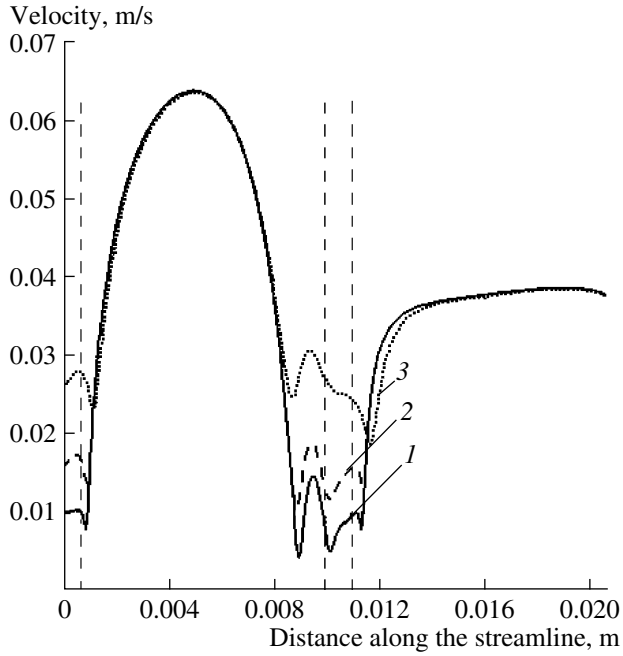

Fig. 12. Diagram of the velocity module distribution along the streamlines. *1*—600; *2*—700; *3*—1 mm.

negative one spreading in the same direction from the lower negative electrode surface. A charge lock does not form in the behind-the-electrode area as in the case of unipolar injection. The liquid streamlines smoothly pass around the passive electrode producing no recurrent vortices, and the so called through EHD flow is realized. Such a flow was obtained and thoroughly studied in experiments using butanol as an impurity [3]. Besides the typical outline diagrams of the velocity, it is useful to examine the distributions of the different variables along the isolated streamlines. Such distributions allow better understanding of the process dynamics of the charging and acceleration of the separate liquid elements. In Figs. 11 and 12, there are presented the distributions of the velocity and the Coulomb forces along three streamlines located in the central EHD-flow jet at 600 μm, 700 μm, and 1 mm from the model symmetry axis. As is seen from Figs. 11 and 12, the electric field beyond the interelectrode gap does not decelerate the through flow but accelerates it.

The velocity field (Figs. 10 and 12) has a number of particular regions:

(1) Immediately at the active electrode, there is some region surrounding the electrode—an immovable liquid "sheath" somewhat outstretched upward. A similar region of more complicated shape is round the passive electrode.

(2) *The leakage area*. As is seen from Fig. 10, the liquid approaching the active electrode has a nonzero velocity at the inlet. This can be explained by examining the pressure forces $\vec{f} = -\nabla p$ affecting the liquid along the streamlines. There is an under-pressure region immediately under the active electrode. This is because, behind the electrode, there is a separation zone appearing at the obstacle flow-around due to the breakdown of the streamlines from the electrode. In this zone, the pressure has a local minimum, which is to say that the pressure gradient has a positive value at the inlet into this region and a negative one at the outlet. With the flow being ordinary, there occur recurrent vortices behind the flown-around body. In our case, this is not observed as, behind the active electrode, the liquid is affected by the positive Coulomb force neutralizing the negative force of the pressure and accelerating the liquid immediately behind the electrode.

(3) *The interelectrode acceleration area.* After the liquid particles acquire a positive charge near the active electrode, they are affected by the Coulomb repulsive force, which creates the main zone of acceleration between the electrodes. As a result, the electric field energy transforms into the liquid kinetic energy and the velocity can amount up to a maximum of 6 cm/s. The jet width in the center can be estimated from the velocity profile between the electrodes. From the velocity distribution presented in Fig. 9, it is seen that a thin jet of the charged liquid moves between the electrodes; the charged jet's thickness is 1.5–2 mm, which is equal to 3–4 radii of the active electrode. This value agrees well with the values gained in practice [3].

(4) *The near-electrode microvortex*. There is a local zone with a very small velocity (about some millimeters per second) ahead of the second electrode, but the liquid in this zone flows in the opposite direction and

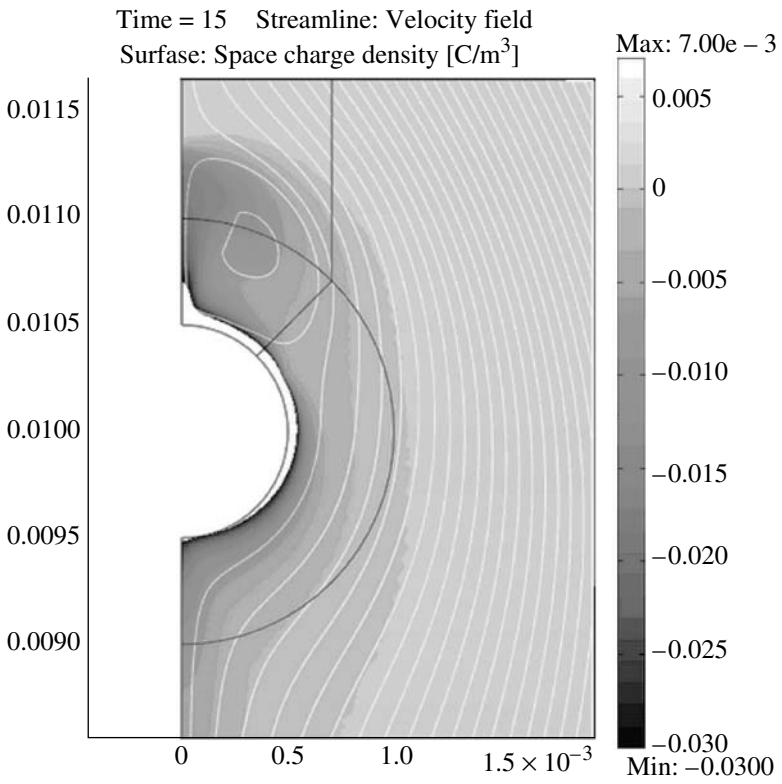

Fig. 13. Electric charge distribution and streamlines near the passive electrode.

the streamlines in this region are of closed "vortex" nature. The existence of this microvortex was suggested for the first time in [3] when analyzing the experimental data on through and recurrent flows. Let us consider more thoroughly the processes occurring here. To understand their nature, we need to examine the electric charge distribution density in the background of the near-electrode flow streamlines.

It follows from the diagram that, near the passive electrode, there occurs the microcirculation of the negative charge sideways along the positive electrode, which the oncoming microvortex generates. It clearly occurs under the action of the inverse Coulomb force localized at the passive counter electrode, which creates some negatively charged oncoming ministream. This stream somehow decelerates the main one and causes a local drop of the flow's kinetic energy. Moreover, it leads to the partial neutralization of the main positive charge coming from the active electrode and to the partial recharge of the stream reaching the flow's tail part.

(5) *Secondary acceleration zone.* The recharge at the passive electrode results in the appearance of the secondary local peak of the Coulomb forces in the flow tail. In turn, this causes the generation of the secondary liquid acceleration zone behind the passive electrode forming the flow type, which is called a through one in the literature [2, 3, 9].

The typical zones of the through EHD flow are easily seen (Fig. 12) when examining the velocity module distribution along the streamlines. Immediately ahead of the active electrode, there is observed the first zone of the liquid active acceleration; ahead of the passive electrode, there is a local peak of the recurrent microvortex; and, behind the passive electrode, there is the zone of the liquid secondary acceleration.

Then, the flow velocity becomes stationary. This is because, behind the passive electrode, the electric force influences the negative charge only in a small behind-the-electrode area (see Fig. 11).

In the case of the through EHD flow, the introduction of the charge from both the active and passive electrodes results in their mutual neutralization; the charge lock retarding the liquid through pumping does not form in the behind-the-electrode area.

The described structure of the through EHD flow is the optimum one in order to organize the electrochemical type EHD pump operation and to remove the EHD flow kinetic energy into the outer circuit. It is advantageous to use such an EHD pump with the aim to produce flows in a closed channel necessary for the operation of EHD heat exchangers. To increase the flow rate, it is also possible to utilize several parallel wires or net-shaped electrodes.

CONCLUSION

A computer simulation of the process of generation and development of EHD flows with a symmetrical sys-

tem of electrodes of the wire–wire type on the basis of a full set of EHD equations in the two-dimensional case has been carried out. In the work, for the first time, the connection of the charge generation degree with the local field intensity in the near-electrode area was considered.

The assay of the EHD flow computer simulation results is presented for the case of unipolar injection and symmetric bipolar and asymmetric bipolar injection.

It is shown that, in the case of unipolar injection, there forms a charge lock hindering the through pumping. In the case of symmetric injection, there is no through pumping, yet the charge accumulation is also absent as there is a zone of charge neutralization located in the center of the IEG.

In the case of the asymmetric bipolar injection, the introduction of the charge from both the active and passive electrodes results in a through EHD flow in which there occurs the mutual neutralization of the charge jets flowing from each electrode in the behind-the-electrode area. As this takes place, behind the interelectrode gap, there appears the liquid secondary acceleration zone favoring the through pumping but not the charge lock hindering it.

REFERENCES

1. Stuetzer, O.M., Ion Drag Pressure Generation, *J. Appl. Phys.*, 1959, vol. 30, no. 7, pp. 98–994.
2. Stishkov, Yu.K. and Ostapenko, A.A., *Elektrogidrodinamicheskie techeniya v zhidkikh dielektrikakh* (Electrohydrodynamic Flows in Liquid Dielectrics), Leningrad: LGU, 1989.
3. Buyanov, A.V. and Stishkov, Yu.K., Peculiarities of Structure of Through Electrohydrodynamic Flow in Symmetric System of Electrodes, *Zh. Tekh. Fiz.*, 2004, vol. 74, issue 8, pp. 120–123.
4. Elagin, I.A. and Stishkov, Yu.K., Computer Simulation of Electrohydrodynamic Flow Formation Process Using a Finite Element Method, Proc. 5th Int. EHD Workshop, France, 2004, pp. 225–229.
5. Zienkiewicz, O.C., Taylor, R.L., and Nithiarasu, P., The Finite Element Method for Fluid Dynamics, 6th edition, Elsevier, 2005.
6. Zhakin, A.I., Near-Electrode and Transition Processes in Liquid Dielectrics, *Usp. Fiz. Nauk*, 2006, vol. 176, no. 3, pp. 280–310.
7. Proc. 7th Int. Conf. On Cond. and Breakd. In Dielectric Liquids (I.C.D.L.), Berlin, West – Germany, 1981.
8. Afanas'ev, S.B., Elagin, I.A., and Stishkov, Yu.K., *Electrofizicheskie protsessy v zhidkostyakh i gasakh. Razdel 2. Electrogidrodinamicheskie process v zhidkostyakh*, (Electrophysical Processes in Liquids and Gases. Section 2. Electrohydrodynamic Processes in Liquids), St. Petersburg: SPbGU, 2007.
9. Glushchenko, P.V. and Stishkov, Yu.K., Electrical Processes in Engineering and Chemistry. Simulation of the Structure of Through EHD-Flow in the wire-wire System, *Electr. Obrabot. Mater.*, 2007, no. 4, pp. 34–41.
10. Groshev, A.K., Mihailov, S.A., and Stishkov, Yu.K., Influence of Electrode-Liquid Boundary Properties on High-Voltage Conductivity of Liquid Dielectrics, *III Mezhresp. Seminar*, (Proc. III Interrep. Seminar), Grodno, 1992.

ISSN 1068-3755, Surface Engineering and Applied Electrochemistry, 2009, Vol. 45, No. 6, pp. 480–484. © Allerton Press, Inc., 2009.
Original Russian Text © F.P. Grosu, M.K. Bologa, 2009, published in Elektronnaya Obrabotka Materialov, 2009, No. 6, pp. 52–58.

ELECTRICAL PROCESSES IN ENGINEERING AND CHEMISTRY

Rotation of a Weakly Conducting Liquid in Crossed Electric and Magnetic Fields

F. P. Grosu[a] and M. K. Bologa[b]

[a]*Moldova State Agrarian University, ul. Mirchesht' 44, Chisinau, MD-2049 Republic of Moldova*
[b]*Institute of Applied Physics, Academy of Sciences of Moldova, ul. Academiei 5, Chisinau, MD-2028 Republic of Moldova*
e-mail: mbologa@phys.asm.md

Received August 21, 2009

Abstract—Two problems of rotation of a liquid in crossed electric and magnetic fields are formulated and solved as applied to the study of the principles of the interaction between external electric and magnetic fields and weakly conducting water type liquids (running water, sea water) and their solutions ($\sigma \sim (10^{-2}$–$10^{2})\ \Omega^{-1}\ m^{-1}$). In the first problem, the liquid is contained in the gap of a vertical cylindrical capacitor, while the second problem deals with the liquid in a rectangular cuvette, two lateral vertical walls of which are used as armatures of a plane-parallel capacitor. In either case, a constant vertical magnetic field is applied to the liquid, while a constant voltage is maintained between the armatures of the capacitor. Three sets of boundary conditions are considered in the first case: the capacitor is of infinite length (throughout the height); the capacitor is confined by a solid bottom from below and has a free boundary with the atmosphere at the top; the capacitor has closed ends and the liquid occupies the entire capacitor gap. The results can be used in various practical applications, for example, for pumping of weakly conducting liquids.

DOI: 10.3103/S1068375509060076

INTRODUCTION

The interactions of external electric, magnetic, or electromagnetic fields with nonmagnetic liquids are known and have been studied thoroughly enough in one of the limiting cases—the high electric conductivity of a liquid when the electric effects (fields) can be neglected in comparison with the magnetic ones; this is the domain of magnetic hydrodynamics (MHD). The opposite case of low conductivity, when the magnetic effects can be neglected, is known and studied to a lesser extent. This is the domain of electric hydrodynamics (EHD), which was formed into a scientific direction not long ago (~20 years ago). However, as a matter of fact, the cases of intermediate values of the electric conductivity of water type liquids (running water or sea water) or their solutions, weak electrolytes, etc., when, as a result of the combined action of electric and magnetic fields, the MHD and EHD effects can appear to be competing, are still unknown and unstudied. It is obvious that the respective hydrodynamic phenomena can be called electro-magneto-hydrodynamic (EMHD). We dealt with these phenomena in [1]; in particular, the ponderomotive forces causing EMHD effects were discussed [2]. It was mentioned that, in the most important cases, in the general expression for the total electromagnetic force, we can be restricted to the pure Coulomb ($\rho\vec{E}$) and ampere ($\vec{j}\times\vec{B}$) ones corresponding to

$$\vec{f} = \vec{f}_e + \vec{f}_m; \quad \vec{f}_e \equiv \rho\vec{E}; \quad \vec{f}_m \equiv \vec{j}\times\vec{B}, \qquad (1)$$

where ρ is the volume-charge density; $\vec{j}$ is the current density; and $\vec{E}$ and $\vec{B}$ are the electric field intensity and the magnetic flux density, respectively.

A criterion of the EHD or MHD-approximations can be the order of the first-to-second term ratio

$$\Pi_{em} \equiv \frac{\tau E}{l_E \cdot B}, \qquad (2)$$

where $\tau \equiv \varepsilon/\sigma$ is the time of the relaxation of the electric phenomena in the medium, and l_E is the characteristic distance at which the electric field intensity varies. If $\Pi_{em} \gg 1$, then the "EHD-approximation" is valid; otherwise, the "MHD-approximation" is. At $\Pi_{em} \sim 1$, the EMHD effects take place.

For good dielectrics ($\tau \geq 10^{-1}$ s), the EHD phenomena become apparent at $E \geq 1$ kV/cm = 10^5 V/m; at $l_E \sim 10^{-2}$ m and $B \sim 1$ T, we obtain $\Pi_{em} \sim 10^5 \gg 1$ (the EHD approximation to high accuracy). The situation is similar for the MHD approximation in liquid metal type conducting media. For sea water, the electric conductivity $\sigma \approx 3.3\ \Omega^{-1}\ m^{-1}$, $\tau \approx 2 \times 10^{-10}$ s [3]; at $E \sim 10^4$ V/m, $\Pi_{em} \sim 1$ at relatively weak magnetic fields $B \sim 10^{-4}$ T.

These estimates show that combined EHD and MHD effects can occur in weakly conducting water type liquids and that they are of concern; however, it is appropriate to begin to study them separately.

Below, we discuss rotational motions of a weakly conducting liquid in crossed electric and magnetic

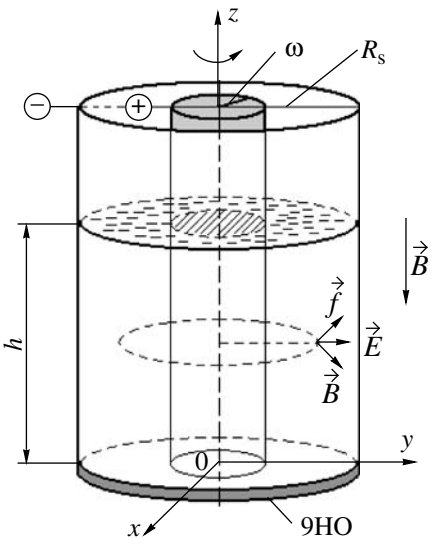

Fig. 1.

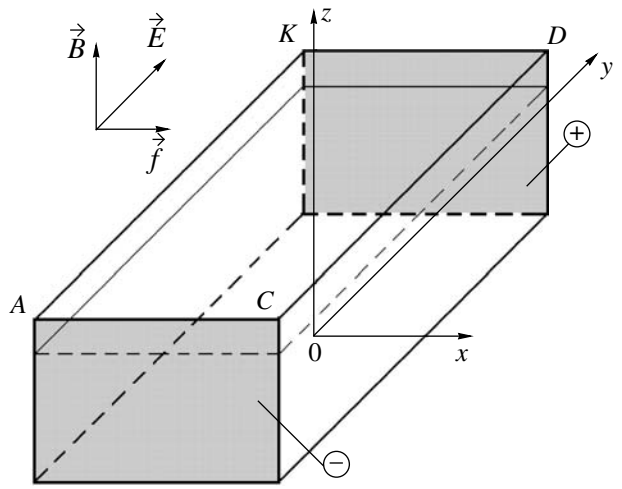

Fig. 2.

fields; for their theoretical description, we can confine ourselves to the magnetic component $\vec{f}_m$ in formulae (1). Herein, the assumed low electric conductivity of the medium allows us to regard the motion as isothermal, because the Joule heating is not taken into account. The regard for the latter would have led to the appearance of the term $\vec{f}_e$, which would have complicated the problem significantly.

Two problems to be analyzed are given by the rotation of a liquid in the gap of a cylindrical capacitor and the rotation of a liquid in a rectangular cuvette (Fig. 2).

THE ROTATION OF A LIQUID IN THE GAP OF A CYLINDRICAL CAPACITOR

Let a liquid occupy the gap of a cylindrical capacitor according to Fig. 1. The entire glass is situated in a vertical constant uniform magnetic field. The cylindrical capacitor is connected to a voltage supply φ_s with the polarity as shown in Fig. 1. The force acting on the liquid has the volume density $\vec{f} = \vec{f}_m$

$$\vec{f} = \vec{j} \times \vec{B}, \tag{3}$$

where the current density is expressed by the formula

$$\vec{j} = \frac{j_s \cdot r_s}{r}\vec{e}_r = \sigma\vec{E} = \frac{\sigma\varphi_s}{r\ln(R/r_s)} \cdot \vec{e}_r, \tag{4}$$

where j_s is the current density on the surface of the inner electrode with the radius r_s, and R is the radius of the outer cylinder.

With regard for (4), it follows from (3) that

$$\vec{f} = \frac{\sigma\varphi_s B}{r\ln m} \cdot \vec{e}_\varphi, \quad m \equiv R/r_s. \tag{5}$$

Due to the azimuthal direction of the force, we seek the solution for the velocity in the form $\vec{\upsilon} = \upsilon_\varphi \cdot \vec{e}_\varphi \equiv \upsilon \cdot \vec{e}_\varphi$; hereupon, the nonlinear term $(\vec{\upsilon}\nabla)\,\vec{\upsilon}$ is omitted in the Navier–Stokes equations, and they take the form

$$\begin{gathered} -\frac{1}{r}\frac{\partial p}{\partial\varphi} + f + \eta\left(\nabla^2\upsilon - \frac{\upsilon}{r^2}\right) = 0; \\ -\frac{\partial P}{\partial r} + \frac{\gamma\upsilon^2}{r} = 0; \quad -\frac{\partial P}{\partial z} - \gamma g = 0; \quad \frac{1}{r}\frac{\partial\upsilon}{\partial\varphi} = 0. \end{gathered} \tag{6}$$

The last equation is the medium continuity equation; the previous ones are written taking it into account. It is obvious that, under the action of rotation force (5), the rotation of the liquid can take place; in addition, from the considerations of the symmetry, we assume that the pressure P will not depend on φ, and $\upsilon = \upsilon(r, z)$ owing to the last equation of set (6). Thereupon, from the first equation of set (6), we obtain

$$\frac{\partial^2\upsilon}{\partial z^2} + \frac{\partial^2\upsilon}{\partial r^2} + \frac{1}{r}\frac{\partial\upsilon}{\partial r} - \frac{\upsilon}{r^2} = -\frac{A}{r}, \tag{7}$$

where we call

$$A \equiv \frac{\sigma\varphi_s B}{\eta\ln m}. \tag{8}$$

We shall solve equation (7) in three variants: if we assume that the cylinder is unbounded neither from below nor from above; if it is bounded by a solid bottom from below and has a free boundary at the top; if the

cylinder is sealed by solid dielectric lids both from below and from above.

Unbounded Cylinder

The case in hand is the velocity distribution in a considerably long cylinder at a distance from its ends, that is, in its center portion. The velocity will be a function of the radial coordinate r only; that is, $\upsilon = \upsilon(r)$. Equation (7) is transformed into the ordinary one

$$\frac{d^2\upsilon}{dr^2} + \frac{1}{r}\frac{d\upsilon}{dr} - \frac{\upsilon}{r^2} = -\frac{A}{r}, \tag{9}$$

In addition, if two conditions (of adhesion) are fulfilled,

$$\upsilon(r)|_{r=r_s} = 0; \quad \upsilon(r)|_{r=R} = 0. \tag{10}$$

Upon the solution of the problem, (9)–(10) have the form

$$\upsilon(r) = \frac{Ar}{2(m^2-1)}\left(m^2\ln\frac{R}{r} + \ln\frac{r}{r_s} - \frac{R^2}{r^2}\ln m\right). \tag{11}$$

In terms of the probable use of the given flow for pumping of liquids (an MHD pump), the rate of the liquid consumption through the longitudinal axial section of a capacitor is of interest

$$Q = \int\limits_{(z,r)}\int \upsilon(r)dzdr = \int\limits_0^h dz\int\limits_{r_s}^R \upsilon(r)dr$$

or per unit of length of the cylinder

$$q \equiv Q/h = \frac{AR^2}{8}\left(\frac{m^2-1}{m^2} - \frac{4\ln^2 m}{m^2-1}\right). \tag{12}$$

This is the steadily increasing function $q(m)$; in addition, at $m \approx 20$, the expression in parentheses amounts to ≈0.9 and tends to unity at a further increase in m. However, it is of concern that $q \sim R^2$ is an extremely strong dependence of the consumption on the outer cylinder radius; it is encouraging with respect to the pump effect as a function of its geometric parameters.

The Situation Corresponding to Fig. 1

It is necessary to solve equation (7) at the boundary conditions

$$\begin{gathered}\upsilon(r,z)|_{r=r_s} = 0; \quad \upsilon(r,z)|_{r=R} = 0,\\ \upsilon(r,z)|_{z=0} = 0; \quad \left.\frac{\partial\upsilon}{\partial z}\right|_{z=h} = 0.\end{gathered} \tag{13}$$

The last condition implies the absence of the tangential component of the stress tensor on the free liquid surface, that is, the neglect of friction between the liquid and the air.

We shall seek the solution of equation (7) in the form

$$\upsilon(r,z) = u(r)\cdot\chi(r,z), \tag{14}$$

where solution (11) of the preceding problem is taken in the capacity of $u(r)$, and the function $\chi(r, z)$ plays the role of a correction factor $0 \le \chi(r, z) \le 1$; in addition, according to (13), it meets the boundary conditions

$$\chi(r,z)|_{z=0} = 0; \quad \left.\frac{\partial\chi(r,z)}{\partial z}\right|_{z=R} = 0. \tag{15}$$

The substitution of (14) into (7) results in the equation

$$\begin{gathered}\chi(r,z)\left(u'' + \frac{u'}{r} - \frac{u}{r^2}\right) + u\left(\frac{\partial^2\chi}{\partial z^2} + \frac{\partial^2\chi}{\partial r^2} + \frac{1}{r}\frac{\partial\chi}{\partial r}\right)\\ + 2u'\cdot\frac{\partial\chi}{\partial r} = -\frac{A}{r}.\end{gathered} \tag{16}$$

Taking into account that $u(r)$ satisfies equation (9), we obtain from (16)

$$\frac{\partial^2\chi}{\partial z^2} + \frac{\partial^2\chi}{\partial r^2} + \frac{1}{r}\frac{\partial\chi}{\partial r}[\ln(ru^2)]' = \frac{A}{ru}(\chi - 1). \tag{17}$$

The estimate of the separate terms of the left-hand side of (17) in terms of the boundary-layer theory conceptions shows that the first term ~χ/δ^2; the other, ~χ/R^2 (at $R \gg r_s$). Taking into account the small thickness of the boundary layer δ on the cylinder bottom as compared to R ($\delta/R \ll 1$), we arrive at the conclusion that, in the left-hand side of (17), we can be restricted to the first term only:

$$\frac{\partial^2\chi}{\partial z^2} \cong \frac{A}{ru}(\chi - 1), \tag{18}$$

where (ru) plays the role of the parameter owning to the absence of derivatives with respect to r. With due regard for the above, the general solution of (18) is as follows:

$$\chi(r,z) = 1 + C_1(r)e^{\lambda z} + e_2(r)e^{-\lambda z}, \tag{19}$$

where we call

$$\lambda \equiv \sqrt{\frac{A}{ru}}, \tag{20}$$

and $C_1(r)$ and $C_2(r)$ are the arbitrary r functions, which are found from conditions (15). Definitely, we find

$$\upsilon(r,z) = u(r)\left(1 - e^{-\lambda z} - \frac{\sinh\lambda z}{\cosh\lambda h}e^{-\lambda h}\right), \tag{21}$$

where $u(r)$ coincides with (11)

$$u(r) = \frac{Ar}{2(m^2-1)}\left(m^2\ln\frac{R}{r} + \ln\frac{r}{r_s} - \frac{R^2}{r^2}\ln m\right). \tag{22}$$

It should be noted that, near the side walls, due to $u(r) \longrightarrow 0$, according to (21), $\upsilon(r, z) \longrightarrow u(r)$, because

$\lambda \longrightarrow \infty$. Hence, $\upsilon(r, z) \longrightarrow 0$ at $r \longrightarrow r_s$, and R is in a complete agreement with the boundary conditions.

On the free liquid surface ($z = h$), the velocity distribution is given by the dependence

$$\upsilon(r, h) = u(r)[1 - e^{-\lambda h}(1 + \tanh\lambda h)]. \quad (23)$$

In thin layers ($\lambda h \ll 1$) within the accuracy of the squared terms $\sim\lambda^2 h^2$, we obtain from (23)

$$\upsilon(r, h) \cong \frac{Ah^2}{2r}, \quad (24)$$

However, according to the foregoing observation, near the walls, this dependence transforms into $\upsilon(r, h) \longrightarrow u(r)$; thus, we state the monotonous increase in the rotational velocity of the film while approaching the capacitor center.

A Capacitor with Closed Ends

A liquid occupies the entire gap of a cylindrical capacitor. In this scenario, we must find $C_1(r)$ and $C_2(r)$ in (19) from the conditions

$$\chi(r, z)|_{z=0} = 0; \quad \chi(r, z)|_{z=h} = 0. \quad (25)$$

We obtain

$$\upsilon(r, z) = u(r)\left[1 - \frac{\sinh(h - z) + \sinh\lambda z}{\sinh\lambda h}\right]. \quad (26)$$

If we displace the origin of the coordinates to the capacitor center, that is, if we set $z = z_1 + (h/2)$ in (26), we find

$$\upsilon(r, z_1) = u(r)\left[1 - \frac{\cosh\lambda z_1}{\cosh\frac{\lambda h}{2}}\right], \quad (27)$$

whence it follows that the velocity is symmetric with respect to the coordinates z_1.

The discussed case of boundary conditions (25) is more adequate in the applied "pump" aspect, because the MHD device is designed to be hermetically-impervious not involving air gaps. The rate of the liquid consumption is determined by formulas similar to (12) and the above, and, with due regard for (27),

$$Q = \int_{-h/2}^{h/2} dz_1 \int_{r_s}^{R}\left[u(r) - u(r)\frac{\cosh\lambda(r)z_1}{\cosh\frac{\lambda(r)h}{2}}\right]dr \quad (28)$$

$$= \int_{-h/2}^{h/2} dz_1 \int_{r_s}^{R}\chi(r, z_1)u dr = \int_{-h/2}^{h/2} dz_1 \cdot \vec{\chi}(z_1) \cdot q \equiv \kappa \cdot h \cdot q,$$

where the mean-value theorem was applied twice (in the first case, with the weight $u(r)$); herein, we call

$$\kappa \equiv \int_{-h/2}^{h/2} \vec{\chi}(z_1)dz, \quad \in (0; 1). \quad (29)$$

Thus, the rate within the accuracy of the proportionality factor κ, which does not exceed unity and tends to unity as h increases, is expressed by the same formula (12) as in the case of an infinite cylinder.

THE ROTATION OF A LIQUID IN A RECTANGULAR CELL

Now consider the physical situation corresponding to Fig. 2, which depicts a rectangular working cell situated horizontally in an external vertical uniform magnetic field with the magnetic flux density $\vec{B}$. The cell is open at the top; in addition, all the walls are made of an insulating material; the two walls hatched in Fig. 2 are metal sheets of a plane-parallel capacitor, which is connected to an external power supply with the voltage φ_s. Under these conditions, the liquid will be in the field of volume-distributed forces (3) with the density

$$\vec{f} = \sigma\vec{E} \times \vec{B} = \sigma EB \cdot \vec{e}_x, \quad (30)$$

where $\vec{e}_x$ denotes the unitary vector of the OX axis; by analogy, $\vec{e}_y$, $\vec{e}_z$ will denote the unitary vectors of the other coordinate axes (lest they be confused with the current density $\vec{i}$ or $\vec{j}$). If we assume that all the quantities in (30) are constant, we arrive at the conclusion that

$$\vec{f} = f \cdot \vec{e}_x, \quad f = \sigma EB = \text{const}, \quad (31)$$

and this force generates a pressure gradient along the OX axis exactly as the gravity force $\vec{f}_g = \gamma\vec{g}$ does vertically. However, a more general equilibrium condition resulting from the general equilibrium equation

$$-\nabla p + \vec{f} = 0, \quad (32)$$

is the equation $\operatorname{rot}\vec{f} \equiv 0$, which, as applied to equations (30) and (31), takes the form

$$\nabla f \times \vec{e}_x = 0, \quad (33)$$

similar to the gravitation case $\nabla\gamma \times \vec{g} = 0$. Herein, as is known [4], there are two possible directions of *gradf*, namely, parallel and antiparallel to the direction $\vec{e}_x$, that is, the force $\vec{f}$. The first one corresponds to stable equilibrium and the second, to unstable equilibrium. Therefore, the motion of the liquid can take place if $\nabla f \uparrow\downarrow \vec{e}_x$, which is equally matched with $\nabla f \cdot \vec{e}_x < 0$. Henceforth, we can

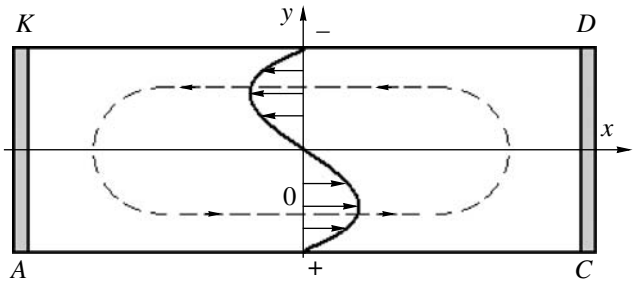

Fig. 3.

be guided by analogy with the gravitational convection probable at $\nabla\gamma \uparrow\downarrow \vec{g}$. Nevertheless, we will discuss one of the simplest problems—the flow in a cell being considerably long along the *OX* direction (Fig. 3). On the basis of the continuity equation $\nabla\vec{j} = 0$, we can see that $j = \sigma E = \text{const}$. Hence, $gradf \neq 0$ can appear only due to the nonuniformity of the magnetic field *B*; that is,

$$\nabla f = j\nabla B = j\frac{dB}{dx}\cdot\vec{e}_x \Rightarrow \nabla f\cdot\vec{e}_x < 0 \Leftrightarrow \frac{dB}{dx} < 0. \quad (34)$$

The magnetic field nonuniformity can be easily generated if the cell is placed in the gap of a permanent magnet (electromagnet) by partial removal of the cuvette from the field along one or another direction; in the case under study, *OX* along the side *DC* (Fig. 3). The field will be weaker in the protruding cell portion (*DC*) and $dB/dx < 0$ according to (34). The situation resembles the case of a liquid heating from below. The appearance of apparently cellular (in the event of $DC \gg AC$) electromagnetic convection will be of the threshold mode. On the basis of the analogies $jB \sim \gamma g$, we can introduce the Grashof number analog—the "magnetic" Grashof number

$$\mathrm{Gr}_{em} = \frac{j\Delta B l^3}{\gamma\nu^2}, \quad (35)$$

where l is the layer thickness. It should be noted that there is no direct analogy with the case of natural convection, because the latter is a purely thermal phenomenon, whereas the problem under discussion is "isothermal."

Now let the working cell be removed from the magnetic field along the direction *OY*. We shall calculate $rot\vec{f}$

$$\nabla\times\vec{f} = \nabla f\times\vec{e}_x = j\frac{dB}{dy}\vec{e}_y\times\vec{e}_x = -j\frac{dB}{dy}\cdot\vec{e}_z \neq 0. \quad (36)$$

Therefore, in this case, equilibrium is impossible at all. Consider the possible rotational motion in the direction elongated according to Fig. 3.

We shall assume the linear law of decreasing of *B*

$$B(y) = B_0\left(\frac{1}{2} - \frac{y}{d}\right), \quad -\frac{d}{2} \le y \le \frac{d}{2}, \quad (37)$$

where $d \equiv CD$ is the cell width. Under the assumed condition $l \gg d$ and the flow according to Fig. 3, the velocity distribution in the center portion of the cell is found from the equation

$$\eta\frac{d^2\upsilon}{dy^2} + \sigma E B_0\left(\frac{1}{2} - \frac{y}{d}\right) = 0, \quad (38)$$

where the pressure gradient is neglected due to its constancy as a consequence of the constancy on the horizontal free surface.

The solution of this equation under the boundary conditions $\upsilon(\pm d/2) = 0$ is the function

$$\upsilon(y) = \frac{\sigma E B_0}{6\eta d}\left(y^2 - \frac{d^2}{4}\right)y, \quad (39)$$

that is, we have a flow with a cubic profile; this flow was qualitatively substantiated by experiments [1].

Let us note that the assumed dependence (37) is the simplest. It is obvious that $B(y)$ is a decreasing but more complicated function; therefore, the velocity profile in a cell can differ significantly from the cubic one.

CONCLUSIONS

The discussed theoretical problems and their solutions can serve as a prerequisite for carrying out new physical experiments with a view to study and design new EMHD devices for practical purposes. In addition, it is possible to advance further by taking into account the Joule heating and the resulting appearance of volume electric charges and Coulomb forces $\rho\vec{E}$ at the next stage of the research. However, all the possible problems concerning the theme under discussion (MHD) are far from settled.

REFERENCES

1. Grosu, F.P., Pasha, G.N., and Bologa, M.K., Hydroelectromagnetic Phenomena in Solutions, *Elektron. Obrab. Mater.*, 2008, no. 2, pp. 55–59 [*Surf. Eng. Appl. Electrochem.* (Engl. Transl.), vol. 44, no. 2, p. 123].
2. Landau, L.D. and Lifshits, E.M., *Elektrodinamika sploshnykh sred* (Electrodynamics of Continua), Moscow: Nauka, 1957.
3. Enokhovich, A.S., *Spravochnik po fizike i tekhnike* (Handbook of Physics and Engineering), Moscow: Prosveshchenie, 1989.
4. Gershuni, G.Z. and Zhukhovitskii, E.M., *Konvektivnaya ustoichivost' neszhimaemoi zhidkosti* (Convective Stability of Incompressible Liquid), Moscow: Nauka, 1972.

ISSN 1068-3755, Surface Engineering and Applied Electrochemistry, 2009, Vol. 45, No. 6, pp. 485–488. © Allerton Press, Inc., 2009.
Original Russian Text © A.V. Khlyustova, A.M. Manakhov, A.I. Maksimov, 2009, published in Elektronnaya Obrabotka Materialov, 2009, No. 6, pp. 59–63.

ELECTRICAL PROCESSES IN ENGINEERING AND CHEMISTRY

A Scenario of Development of Low-Voltage "Underwater" Discharge

A. V. Khlyustova, A. M. Manakhov, and A. I. Maksimov

Institute of Chemistry of Nonaqueous Solutions, Russian Academy of Sciences, ul. Akademicheskaya 1, Ivanovo, 153045 Russia

e-mail: kav@isc-ras.ru

Received May 26, 2009

Abstract—Based on the analysis of experimentally obtained oscillograms of the current, voltage, and "end face" discharge spectral line intensity, a scenario of "underwater" discharge development is proposed. The three main stages of the discharge formation are revealed: the bubble growth, the "quiet" discharge, and the active discharge form differing from the previous forms by the sharp pulse intensity and greater amplitude of the voltage variation.

DOI: 10.3103/S1068375509060088

INTRODUCTION

Diaphragm, capillary, and "end face" discharges and those occurring in long (bent) tubes filled with an electrolyte fall into low-voltage (not impulse) "underwater" discharges (Fig. 1).

It is true for all these discharges that they ignite from (not impulse) sources with a voltage in the range from ~500 V to several thousands of volts. In all the cases, the discharge ignition is preceded by the generation of steam and steam-gas bubbles in the electrolyte bulk, and the estimations show that the most important role is played by the steam generation caused by the local overheating of the solution. The experience suggests that the particular mechanism of bubble growth and electric breakdown depends on the system's geometry and primarily on the diameter of the overlapping cross section of the tube or diaphragm. Evidently, the mechanism in the case of discharge in a diaphragm or a narrowing capillary end is simpler. It is generally agreed that in this case the generation of a bubble results in the overlapping of the transporting channel and the termination of the electrolysis current. The whole e.m.f. source (plus the self-inductance e.m.f. in the case of an alternating current supply) effects the generated bubble. If this potential difference is large enough, electric breakdown happens. The data of work [1] allow one to specify the assumed scenario of the underwater discharge formation for the case of a thin capillary. The generation of a bubble in the form of a ring growing from the side of the walls caused by the local solution overheating will really result in the progressive narrowing of the transporting channel along the capillary axis and the increase of the voltage drop in this part. As in the previous case, with the voltage drop being great enough, there occurs the electric breakdown of the bubble. However, the complete overlapping of the capillary before the breakdown is not necessary. It is easy to verify that, in this case, the breakdown conditions will depend on the full voltage in the cell and the system's geometry. The experimental data for capillary discharges are not in contradiction with the described picture [2]. However, the investigation of the underwater discharge forming in wide tubes with an electrolyte is beyond the mentioned scope.

TEST CONDITIONS

An "end face" underwater discharge was ignited in a glass tube with an inner diameter of 10 mm vertically submersed into a solution with an electrolyte. The graphite electrode overlapping the tube cross section was placed at a distance of 5–15 mm from the tube cut off. The second electrode was located in the bulk of the main cell. Aqueous solutions of sulfuric acid and sodium sulphate with concentrations of 0.01 M to 0.1 M were used as the electrolytes. The discharge was ignited from the transformer at a frequency of 50 Hz with the maximum voltage being not more than 2500 V and the current being up to 1–2 A. The detailed experimental pattern was described earlier [3]. The transition to a tube with a large diameter leads to the fact that the discharge development phases, including the growth of the bubble and its breakdown, slowed down substantially; it becomes easier to observe them and to analyze them. By varying the voltage applied to the cell, it was possible to terminate the process in one of the phases.

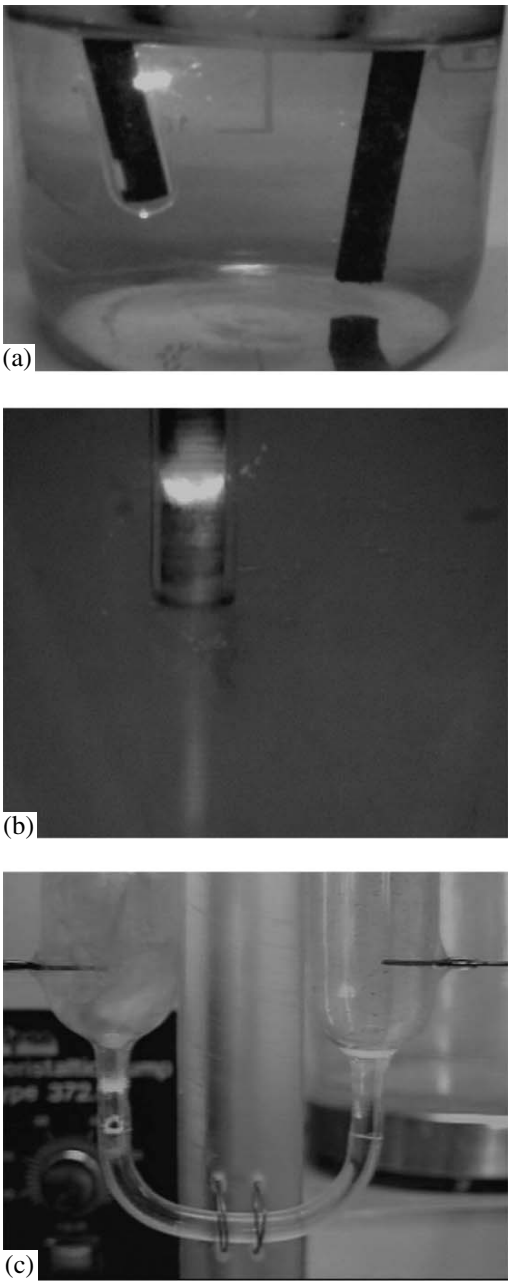

Fig. 1. An external view of underwater discharges. (a) diaphragm discharge; (b) "end face" discharge; (c) discharge in a long dielectric tube filled with an electrolyte.

SCENARIO OF THE FORMATION OF THE "END FACE" UNDERWATER DISCHARGE

Bubble Growth

With the voltage being relatively small, the steam-gas bubble grows without further breakdown. The heating of the electrolyte is insufficient for the quick growth of the steam bubble; therefore, the contribution of the electrolysis to this process is great. Depending on the spacing between the electrode and the tube cut off, the bubble can be fixed immediately near the cut off or in the intermediate position between the electrode and the cut off. The generation of the bubble causes the drop of the current in the circuit from 1–2 A to several milliamperes. There remains a circular gap between the bubble and the tube wall filled with the electrolyte.

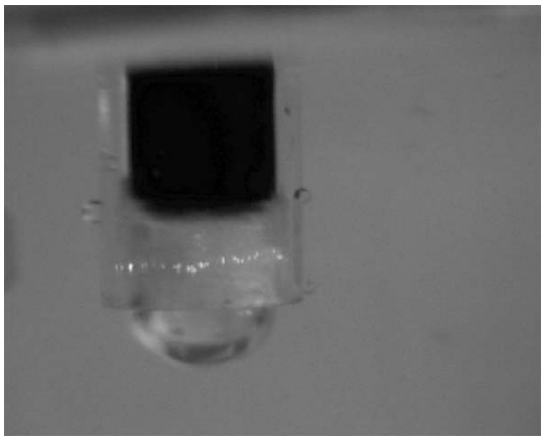

Fig. 2. Microdischarges in the circular gap between the bubble and the tube wall (the "quiet" discharge).

Quite Discharge

When the voltage in the cell is higher, there occur breakdowns in the electrolyte filling the circular gap between the bubble and the tube walls (Fig. 2). They are microdischarges quickly moving in a circle in this circular gap. The current force in the circuit grows from several milliamperes to ~20 mA.

The path of the microdischarges noticeably differs from the circle and, in addition, moves upright. This discharge form can steadily exist for a long time depending on the voltage in the cell, the chemical composition of the solution, and its temperature. Then, there is observed the development of a discharge in the bubble itself, resulting in the bubble collapsing with blowout of the active phase into the region of the main solution and generation of a great sound wave in the solution. The lifetime of the "quite" discharge form observed experimentally is presented in Table 1.

The oscillograms of the current, voltage, and integral radiation intensity during the process of the "quiet" discharge formation are shown in Fig. 3. The region *a* corresponds to the generated bubble before the breakdown. The high voltage in the cell at very small current and radiation is at the background level. At the transition to the "quiet" discharge (region *b*), the current grows, the voltage in the cell drops, and radiation of small intensity appears synchronized with the outer voltage.

Table 1. The lifetime of the "quite" discharge form

Solution	Concentration, mol/l	Electric conductivity, mSm/cm	Time of steady burning
Na_2SO_4	0.002	0.65	more than 1 h
H_2SO_4	0.06	5	more than 1 h
Na_2SO_4	0.02	5	~5 min
H_2SO_4	0.015	10	~10 min
Na_2SO_4	0.05	10	less than 1 min
Na_2SO_4	0.1	15	~1 s

The Active Discharge Form

The transition of the discharge into the active form consists in the transmission of the breakdown to the whole bubble volume with its following enlargement accompanied by the blowout of the plasmolysis products and activated solution into the cell (Fig. 4). The process is attended with the generation in the solution of an intensive sound wave with the maximum amplitude at a frequency of about 2 kHz. The afterglow with a duration up to ~0.1–0.2 s characterizes the active form of the discharge.

The oscillograms in Fig. 5 illustrate the transition from the "quiet" discharge to the active form.

The increase of the voltage in the cell causes the appearance of the active discharge form without delay at two intermediate phases—the bubble generation and

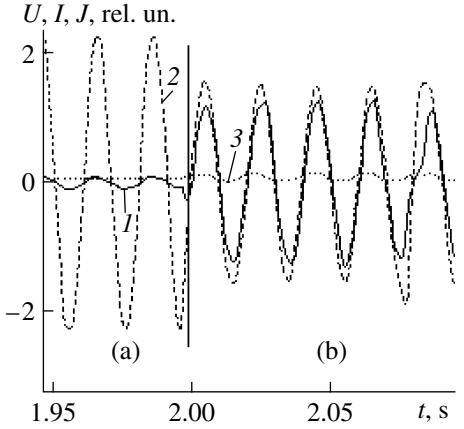

Fig. 3. The current in the cell (*1*), the voltage (*2*), and the integral radiation intensity (*3*). Na_2SO_4 0.01 M.

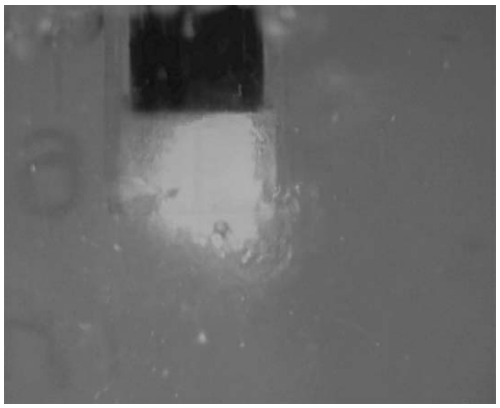

Fig. 4. Active form of the underwater "end face" discharge.

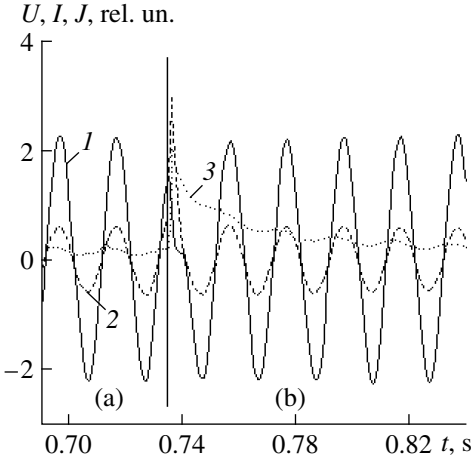

Fig. 5. The current in the cell (*1*), the voltage (*2*), and the integral radiation intensity (*3*). Na_2SO_4 0.05 M.

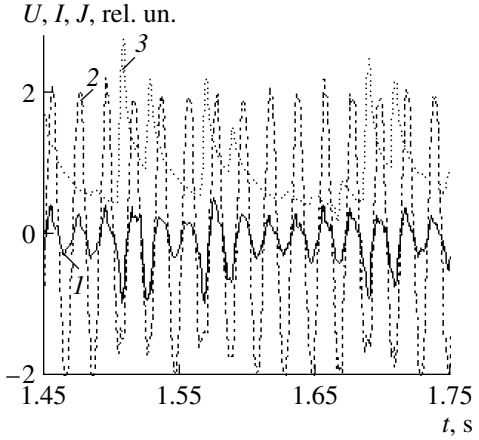

Fig. 6. The oscillograms of the current in the cell (*1*), the voltage (*2*), and the integral radiation intensity (*3*). Na_2SO_4 0.04 M. Repeated ignitions of the active discharge form.

Table 2. Voltage of the ignition of the active form of the "end face" discharge at the solution temperature of 25°C

Solution	Electric conductivity, mSm/cm	Breakdown voltage, B
Na_2SO_4, 0.05 M	9	400
Na_2SO_4, 0.025 M	5	450
Na_2SO_4, 0.02 M	0.65	1000
H_2SO_4, 0.015 M	9	950

the "quiet" discharge ignition. There are observed repeated discharge ignitions (Fig. 6) transiting in the limit (at high voltage and a heated solution) to burning synchronized with the outer voltage.

The voltage of the "direct" ignition of the active form of the discharge depends on the chemical composition of the solution, its electric conductivity, and temperature. Some data for solutions at room temperature are presented in Table 2.

CONCLUSIONS

One of the possible scenarios of the development of low-voltage "underwater" discharge in dielectric tubes filled with an electrolyte solution includes three main phases: (1) generation of steam-gas or steam bubbles not completely overlapping the tube cross section; (2) ignition of "quiet" discharge in the electrolyte interlayer between the bubble and the tube wall; (3) the transition of the "quiet" discharge into the active form filling the whole bubble with the following collapse of the plasma bubble. At relatively low voltages in the cell, all the phases can be realized separately in time. At high voltages, the two first phases are short and sometimes not observed.

REFERENCES

1. Teslenko, V.S., Drozhzhin, A.P., and Sankin, G.N., Autocyclic Circular Breakdown in Electrolyte with Forced Collapse of Bubbles, *Pis'ma v ZhTF,* 2006, vol. 32, issue 4, pp. 24–31.

2. Nikiforov, A.Yu. and Leys, C., Influence of Capillary Geometry and Applied Voltage on Effectiveness of Hydrogen Peroxide and OH Radicals Formation in AC Underwater Electrical Discharge, *Plasma Sources Science and Technology*, 2006, vol. 15, no. 4, pp. 818–828.

3. Khlyustova, A.V., Manakhov, A.M., Maksimov, A.I., and Khorev, M.S., Connection of Electric and Optic Properties of Plasma-Solution Systems, *Electr. Obrab. Mat.*, 2009, no. 5, pp. 18–23.

ISSN 1068-3755, Surface Engineering and Applied Electrochemistry, 2009, Vol. 45, No. 6, pp. 489–491. © Allerton Press, Inc., 2009.
Original Russian Text © M.K. Bologa, I.V. Kozhevnikov, 2009, published in Elektronnaya Obrabotka Materialov, 2009, No. 6, pp. 64–67.

ELECTRICAL PROCESSES IN ENGINEERING AND CHEMISTRY

Influence of the Electric Field and the Arrangement of the Stages on Multistage Pump Characteristics

M. K. Bologa and I. V. Kozhevnikov

Institute of Applied Physics, Academy of Sciences of Moldova, ul. Akademiei 5, Chisinau, MD 2028 Republic of Moldova
e-mail: mbologa@phys.asm.md

Received July 22, 2009

Abstract—Results of the investigation of the influence of the geometric parameters of the gap between the stages and the galvanically isolated high voltage sources on the characteristics of a multistage electrohydrodynamic pump are presented. The optimum distance between the stages at which their mutual influence appearing due to Coulomb forces between neighboring electrodes of different stages is practically absent has been found. It is shown that similar results can be obtained under the conditions of galvanically isolated high voltage sources when the distances between the stages are comparable with the interelectrode gap in a stage. This fact will contribute to the reduction of multistage pump dimensions.

DOI: 10.3103/S106837550906009X

The use of an electric field is one of the promising ways of transport of gaseous and liquid dielectric media. The devices in which the electric energy is converted into mechanical energy are called EHD pumps (converters) [1–3] and are distinguished by the absence of moving parts, their design simplicity, and their higher capacity and economic feasibility. Various designs of EHD pumps are known, but the potentialities of a single-stage model (in most cases formed by two or three electrodes) are limited from the point of view of both the created head and the flow rate of the pumped dielectric liquid.

Thus, single-stage EHD converters are arranged in parallel and in series depending on the necessary output characteristics. For these purposes, constructions with three bar (wire) electrodes are the most plausible, permitting one to easily improve the converter flow characteristics due to their parallel arrangement forming electrode grids located opposite to each other. The head increase is attained with the help of a multistage pump consisting of electrode grids [4]. However, there appear additional factors, such as the mutual influence of the stages, substantially affecting the operation efficiency of the devices.

In this connection, the purpose of this work is to investigate the influence of the gap between the stages and the galvanically isolated voltage sources on the characteristics of multistage converters.

The research work was carried out using an installation consisting of a rectangular reservoir filled with the working medium (transformer oil with the electric conductivity $\sigma = 0.9 \times 10^{-11}$ Ohm^{-1} m^{-1}) in which there is mounted a two-stage EHD pump (Fig. 1). Stages *1* and *2* are located in rectangular casing *3* made from organic glass. Each stage consists of two electrodes: the emitter and the collector made in the form of grids from wires stretched with certain spacing in parallel to each other on a rectangular dielectric frame produced from shock resistant polystyrene. The emitter wires are covered with insulating coatings with holes on the collector side. The stage electrodes are bonded together with the

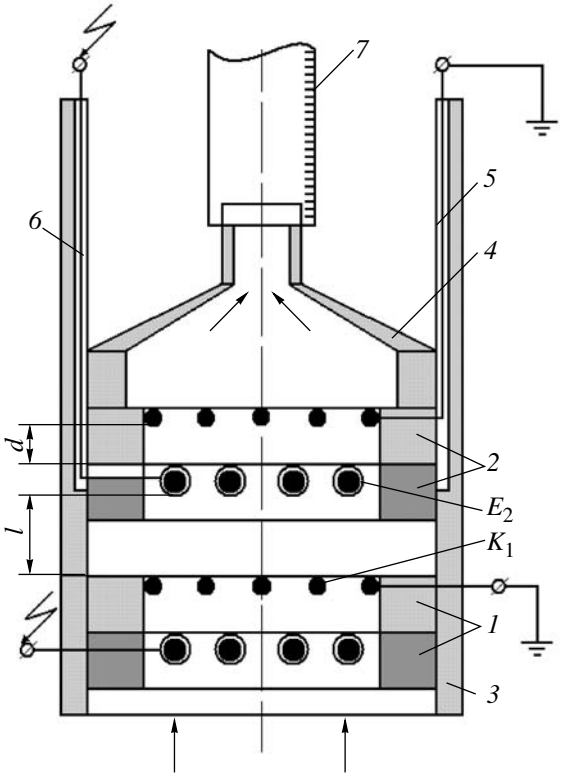

Fig. 1. Two-stage electrohydrodynamic pump.

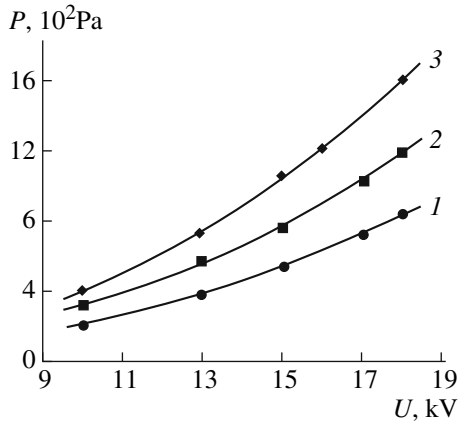

Fig. 2. Relationship between the head and the potential difference between the electrodes: *1*—one stage; *2*—two stages; *3*—two stages connected to galvanically isolated high voltage supplies; d = 2mm, l = 2 mm.

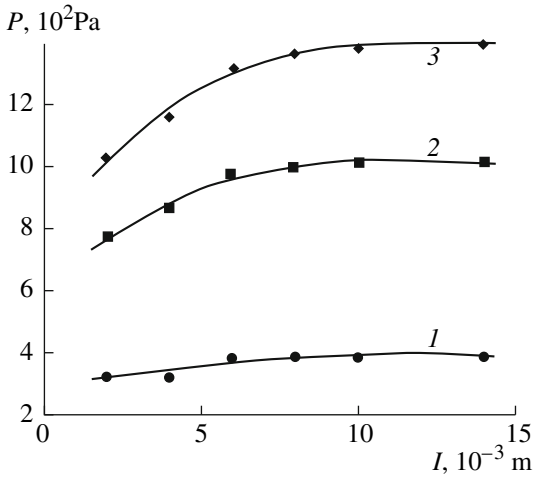

Fig. 3. Dependence of the head on the distance between the stages in a two-stage pump at different voltages, U, kV: *1*—10; *2*—15; *3*—17.

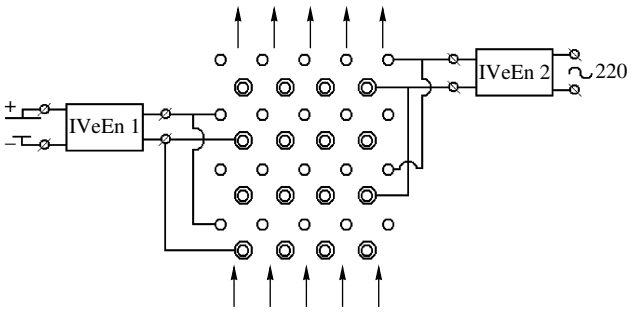

Fig. 4. The diagram of the connection of the electrodes to the high voltage sources.

gap d = 2mm. The first stage *1* (Fig. 2) is bonded to the casing *3* and is immovable. Stage *2* is connected with the pump outlet pipe *4* and can move along the rectangular channel formed by the casing *3*. Grooves *5* and *6* were made in the casing sidewall so that the current leads could be moved when the distance l between the stages is varied. The latter is determined with the help of markings on the casing sidewall *3*.

The pump outlet pipe is connected with piezometer *7* intended for the measurement of the pressure (head) created by the pump. High voltage is applied from two high-voltage supplies with one being fed from the accumulator and the other, from a 220 V network.

The experiments were carried out at the zero flow rate, thus permitting one to reliably reveal the influence of the different factors on the EHD converter operation.

The relationships between the two-stage pump head characteristics and the type of high voltage supply used are presented in Fig. 2. In the case of the connection of both stages to the same supply, the pump head characteristic (curve 2, Fig. 2) is proportional to the pressure produced by one stage (curve *1*, Fig. 2) multiplied by the coefficient $k \sim 1.4$. The reason is that, between the emitter E_2 (Fig. 1) and the collector K_1, under the action of the electric field, there appear coulomb forces that influence the ions not recombined on the collector K_1 creating additional resistance to the main flow of the working substance. The effect of these forces is much weaker when the stages are connected to separate high voltage supplies galvanically isolated from each other (curve *3*, Fig. 2) with the head characteristic of the two-stage pump being almost twice improved ($k \approx 1.93$). However, some mutual influence of the stages is retained at the expense of the polarization effects.

The mutual influence of the stages can also be reduced at the expense of the increase of the gap between them (Fig. 3) with the dependence of the head on l being almost absent at a low voltage (curve *1*). With the voltage increasing, the relationship $P = F(l)$ up to l = 7 mm becomes steeper (curves *2* and *3*), indicating that the mutual influence of the stages enhances. In what follows, the pressure achieves a stationary state and, in the range l = 8–14 mm, does not change. Thus, at $l \geq 8$ mm, the stages do not interact and the two-stage pump head becomes equal to the algebraic sum of the pressures produced by each stage under the conditions of a single-stage converter.

To elucidate the efficiency of the use of galvanically isolated sources in pumps with more than two stages, there were mounted two additional stages. The connection diagram for the EHD-converter stage electrodes is shown in Fig. 4. The obtained relationships (curves *1* and *2*, Fig. 5) indicate the diminution of the influence of the galvanically isolated sources on the four-stage pump performance. The heat increase is not more than 10 percent of the pressure produced by the pump connected to one source (curve *1*, Fig. 5). With l increasing, particularly at l = 4 mm, the galvanic isolation of the

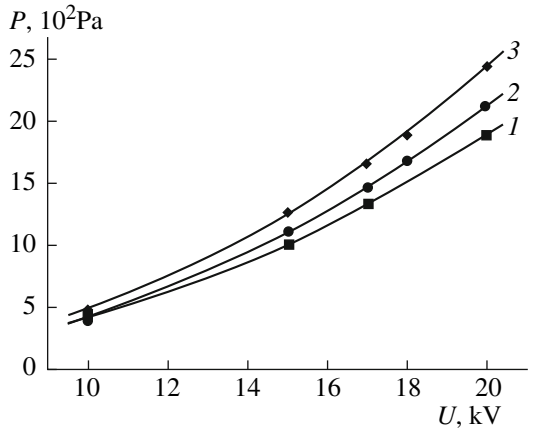

Fig. 5. Dependence of the head on the potential difference between the electrodes at various ways of connection of the electrodes to the voltage supplies; (*1*, *3*) to one supply; (*2*) according to Fig. 4.

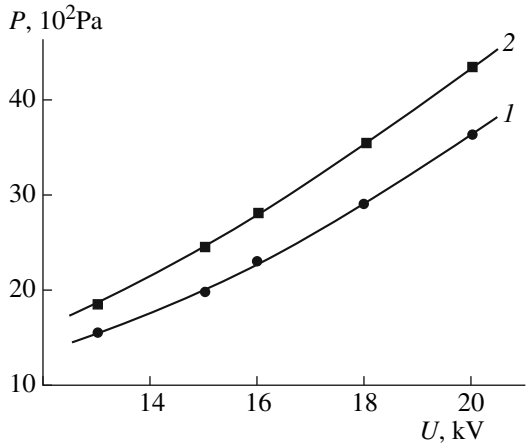

Fig. 6. Dependence of the head on the potential difference between the electrodes at various ways of connection of the electrodes to the voltage supplies; $d = 2$ mm, $l = 2$ mm, $l_1 = 8$ mm, and $\sigma = 2.5 \times 10^{-11}$ $Ohm^{-1}m^{-1}$: (*1*) to one supply; (*2*) according to Fig. 4.

sources does not influence the pump output characteristic (curve *3*, Fig. 5) with the latter changing with the increase of the gap l_1 between the second (the lower stage is the reference point, Fig. 4) and the third stages (curves *1* and *2*, Fig. 6). At the distance $l_1 = 8$ mm, stages 3 and 4 hardly affect stages 1 and 2. The use of galvanically isolated sources reduces the mutual influence between the third and fourth (1st and 2nd) stages, thus increasing by 20 percent the pressure produced by the pump (at $U = 22$ kV).

Thus, the application of galvanically isolated sources is efficient at gaps between the stages comparable with the interelectrode spacing with the number of stages being not more than two. The optimum distance between the pump stages connected to one voltage source is 8 mm (in the studied range of the electric field intensity) influencing the converter dimensions. Therefore, to reduce the geometrical parameters of a multistage pump, it is more expeditious to make use of galvanically isolated sources and the location of single stages or groups of stages at a distance close to the optimum one.

REFERENCES

1. Denisov, A.A. and Nagornyi, V.S., *Elektro- i elektrogazodinamicheskie ustroistva avtomatiki*, (Electro- and Electrogasdynamic Automatic Devices), Leningrad: Mashinostroenie, 1979, 228 p.
2. Rubashev, I.B. and Bortnikov, Yu.S., *Elektrogazodinamika*, (Electrogasdynamics), Moscow: Atomizdat, 1971.
3. Stishkov, Yu.K. and Ostapenko, A.A. *Elektrogidradinamicheskie techeniya v zhidkikh dielectrikakh*, (Electrohydrodynamic Flows in Liquid Dielectrics), Leningrad: Mahinostroenie, 1989, 176 p.
4. Bologa, M.K., Kozhevnikov, I.V., and Kozhuhar', I.A., Multistage Electrohydrodynamic Pump, *Ann. Conf. on Elect. Insulation and Dielectric Phenomena*, 2000, vol. 1, pp. 57–60.

ISSN 1068-3755, Surface Engineering and Applied Electrochemistry, 2009, Vol. 45, No. 6, pp. 492–494. © Allerton Press, Inc., 2009.
Original Russian Text © L.Z. Boguslavskii, 2009, published in Elektronnaya Obrabotka Materialov, 2009, No. 6, pp. 68–70.

ELECTRICAL PROCESSES IN ENGINEERING AND CHEMISTRY

Engineering Methods of the Calculation the Technological Parameters of a Pulse Corona Discharge in Strong Electrolytes and for a Multipoint Electrode System

L. Z. Boguslavskii

Institute of Pulse Processes and Technologies, National Academy of Sciences of Ukraine, pr. Oktyabr'skii 43A, Nikolaev, 54018 Ukraine

e-mail: iipt@iipt.com.ua

Received June 3, 2009

Abstract—An engineering method for the calculation of the technological parameters of a pulse corona discharge (the maximum pressure at the boundary of the continuous plasma formation and its radius and the maximum pressure at the compression wave front for the selected external adjustable parameters of the pulse generator) as part of a technological electrical discharge device is offered. In the second part of the paper, the calculation of the parameters for a multipoint or multi-electrode system is presented.

DOI: 10.3103/S1068375509060106

INTRODUCTION

The engineering methods of calculation of the pulse corona discharge (PCD) characteristics in strongly conducting liquids when the fork corona turns into a continuous plasma formation (CPF) for a single-point electrode system as proposed in the first part of the present paper represents fairly reliable data concerning the choice of the adjustable parameters of the pulse current generator as part of a technological device and their correspondence to the known experimental results.

The use of a PCD in technological applications enables one to form in liquids fields of pressures of a specified configuration due to a great number of points distributed in the space in which there simultaneously ignites a discharge [1 and 2]. Such a multipoint electrode system may be brought into the nearest proximity with the object being processed, and it allows one to consider all the subtleties of the complicated surface being processed without its (or the electrode it is processed by) being mechanically shifted. The latter is of particular importance since mechanically movable systems under conditions of high pulsed loads are considered to be the weakest points in the reliability of technological electrical discharge devices and require the development of intricate systems of automatic control. The use of parallel electrodes included into one discharge circuit allows one to considerably expand the technological capacities of PCD with CPF application.

The second part of the paper deals with the development of engineering methods of the PCD technological parameters' calculation for selected parameters of the pulse load center for a multipoint or multi-electrode system.

THE PCD IGNITIONS IN A MULTIPOINT ELECTRODE SYSTEM

According to the investigations in [2], for the electrolyte conductivities of $\sigma_0 \geq 0.1$ Sm/m, the CPF ignition is possible at n identical points simultaneously, actually, with similar parameters of its development. In this case, at elaborating the engineering methods of the PCD calculation, there arises another condition concerning the simultaneous charge ignition at n points. According to [3], a necessary condition for the charge ignition in an electrolytes is the development of overheating instability. The main characteristic defining this process is the duration of its development t_n, which should be far less than the constant of the time of the capacitive storage discharge C:

$$t_n \ll R_g C. \tag{1}$$

The initial resistance of the gap in this case is determined as

$$R_g = \frac{R_{el}}{n} = \frac{1}{2\pi\sigma_0 n r_{el}}, \tag{2}$$

where R_{el} is the resistance of a gap at a single point and r_{el} is the round-up radius of a single point.

The development of the overheating instability is calculated as follows:

$$t_n = \frac{\rho_1 c_p}{\alpha}\frac{1}{\sigma_0 E_0^2} = \frac{\rho_1 c_p}{\alpha}\frac{r_{el}^2}{\sigma_0 U_0^2}, \tag{3}$$

where ρ_1 is the liquid density, c_p is the thermal capacity, α is the temperature coefficient of the liquid's electric con-

ductivity, E_0 is the electric field intensity at a single point, and U_0 is the initial voltage at the capacitive storage.

Thus, we obtain that $\frac{\rho_1 c_p}{\alpha}\frac{r_{el}^2}{\sigma_0 U_0^2} \ll \frac{1}{2\pi\sigma_0 n r_{el}}$, where the maximum number of points at which the PCD with CPF is to be ignited without fail should not exceed

$$n \ll \frac{\alpha}{\rho_1 c_p}\frac{U_0^2 C}{r_{el}^3}. \quad (4)$$

Expression (4) is supposed to be one of the criteria for the selection of the parameters of the discharge circuit and the electrode radius r_{el}.

The dissipation intensity of the energy liberated from each of the n ignited CPF N_{nam} is determined as

$$N_{nam} = \frac{N_{am}}{n}, \quad (5)$$

where N_{am} is the energy released over the entire discharge gap.

Then, according to the first part of the present paper, the pressure at the plasma–liquid boundary of each of the points reaches its maximum value from the condition

$$P_{nam} = \left(\frac{25(\gamma-1)^2 A_s U_0^2 k \rho_0^2 v_{am} k^* \sigma_0}{16\pi^2\left(\gamma+\frac{1}{3}\right)L^2 n r_{el}\left(1+\frac{v_{am}}{c_0}\right)^2}\right)^{1/4}, \quad (6)$$

where $\gamma = 1.26$ is the effective indicator of the discharge plasma adiabat, $A_s = 10^5 (V^2\ c)/m^2$ is the spark constant, $c_0 = 1400$ m/s is the sound velocity in water, $k^* = 0.126$ m/Sm is a coefficient, $v_{am} = 10^3$ m/s is the velocity of the CPF expansion by the peak current moment, L is the discharge circuit inductance, and ρ_0 is the electrolyte density.

Herewith, the coefficient k for the nonperiodic discharge should also consider the gap resistance varying due to the attenuation decrement change:

$$\delta = \frac{1}{4\pi\sigma_0 n r_{el}}\sqrt{\frac{C}{L}}. \quad (7)$$

The peak radius of each of the CPF looks like

$$a_{nm} = \left(\frac{(\gamma-1)^2 A_s U_0^2 C^2 k_{am} k^* \sigma_0\left(1+\frac{v_{am}}{c_0}\right)^2}{25\pi^2\left(\gamma+\frac{1}{3}\right)r_{el}\rho_0^2 v_{am}^3}\right)^{1/4}, \quad (8)$$

and, relatively, the pressure of the shock-wave front from each of the CPF may be defined as

$$P_{nm} = \frac{(\gamma-1)}{2\pi r}\left(\frac{2A_s W_0 k k^* \sigma_0}{\left(\gamma+\frac{1}{3}\right)r_{el} v_{am} L n}\right)^{1/2}, \quad (9)$$

where W_0 is the energy accumulated in the capacitive storage.

THE CALCULATION METHODS OF THE PCD PARAMETERS FOR A MULITPOINT ELECTRODE SYSTEM

On the whole, the calculation methods for n electrodes should comprise the following items:

(1) The definition of the necessary parameters of the discharge circuit from the conditions offered in first part of the paper needed for obtaining the required pressure level at the shock-wave front for a single electrode.

(2) For the chosen parameters, we fix the attenuation decrement δ, which, in this case, serves as a similarity criterion, and, with regard to a decrease of r_{el} or an increase of the storage capacity, n (the number of the parallel points or electrodes) is selected.

(3) According to the dependence $n = \frac{\alpha}{10\rho_1 c_p}\frac{U_0^2 C}{r_{el}^3}$, we define the maximum number of parallel electrodes at which the CPF ignites. In the case when the calculated value is no less than the quantity of the selected electrodes, the values selected by item 2 are taken. If not, correspondingly, we make corrections to the selected values of either the number n or the parameters U_0, C, and r_{el}.

(4) It is necessary to control the similarity criterion value β [4], which, in the case of n electrodes, is defined as

$$\beta = \frac{\sigma_0 U_0^2 (LC)^{2/3}}{\rho_0 (n r_{el})^4}.$$

(5) Thus, provided all the conditions are met, one can use n parallel electrodes and calculate the pressure using formula (9).

The calculation results according to the offered technique of the maximum wall pressure of the PCD plasma cavity and the shock-wave-front pressure in the multipoint electrode system at each of the points with their various quantities are displayed in the figure.

CONCLUSIONS

In the paper, there are presented the obtained analytical dependencies of the main technological parameters of the PCD with CPF of the peak pressure at the boundary of the CPF and its radius and the maximum pressure

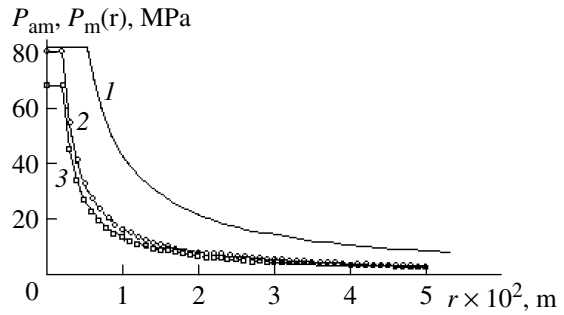

The calculation of the maximum pressures at the wall of the plasma cavity P_{am} and at the compression wave front P_m(r) at a single point with their various quantities depending on the distance to the CPF at $C = 2$ μΦ, $U_0 = 50$ kV, $L = 6$ μG, $\sigma_0 = 2.2$ Sm/m, and $r_{el} = 5$ mm. *1*—$n_{el} = 1$; *2*—$n_{el} = 3$; *3*—$n_{el} = 6$.

at the compression wave-front at a distance from the CPF either for the multipoint or multi-electrode system, which allowed us to offer engineering methods for the calculation of the PCD characteristics with regard to the external adjustable parameters of the pulse power source with the capacitive storage of energy.

REFERENCES

1. Telyashov, L.L., The Development Peculiarities of the "Breakdownless Discharge in the Liquid, *Elektron. obrab. mater.*, 1989, no. 2, pp. 38–41.
2. Boguslavskii, L.Z., Bristetskii, E.V., Krivitskii, E.V. and Petrichenko, V.N., Investigation of the Ignition of Multiflame Corona Discharge in Weakly Conducting Electrolytes, in *Teoriya, eksperiment, praktika elektrorazryadnykh tekhnologii* (Theory, Experiment, Practice of Electrodischarge Technologies), 2002, issue 4, pp. 7–15.
3. Krivitskii, V.V., *Dinamika elektrovzryva v zhidkosti* (Dynamics of Electroblast in Liquids), Kiev: Naukova dumka, 1986.
4. Shamko, V.V., Krivitskii, E.V. and Kucherenko, V.V., Approximated Similarity of Electrophysical and Kinematic Processes at a Pulse Corona Discharge in Strong Water Electrolytes, *Zh. Tekh. Fiz.*, 1999, vol. 69, issue 5, pp. 30–34.

ISSN 1068-3755, Surface Engineering and Applied Electrochemistry, 2009, Vol. 45, No. 6, pp. 495–501. © Allerton Press, Inc., 2009.
Original Russian Text © V.A. Koromyslov, A.I. Grogor'ev, M.V. Rybakov, Yu.N. Zhigalko, 2009, published in Elektronnaya Obrabotka Materialov, 2009, No. 6, pp. 71–79.

ELECTRICAL PROCESSES IN ENGINEERING AND CHEMISTRY

On Calculation of the Electric Field Intensity near the Surface of a Nonlinearly Oscillating Charged Drop in a Uniform External Electrostatic Field

V. A. Koromyslov, A. I. Grogor'ev, M. V. Rybakov, and Yu. N. Zhigalko

Demidov State University, ul. Sovetskaya 14, Yaroslavl, 150000 Russia

e-mail: grig@uniyar.ac.ru

Received August 25, 2009

Abstract—The solution of the problem on nonlinear oscillations of a drop in a uniform external field has been found. It has been shown that, at the top points of the drop, the field intensity is high enough for the corona discharge ignition.

DOI: 10.3103/S1068375509060118

INTRODUCTION

The research of the stability of linear and nonlinear oscillations of charged drops has been due to the numerous academic, engineering, and technological applications (see, e.g., reviews [1–3] and the literature mentioned therein). A charged drop is considered to be an object of study in storm clouds [4, 5]; in liquid-metal sources of ions [6, 7]; in mass-spectrometric devices for thermally unstable and nonvolatile liquids [8, 9]; and at spraying coating compositions, combustibles, and insecticides [10].

However, the most intense interest in charged drops in external electric fields relates to the theory of storm electricity both with respect to the processes of microseparation of the charges and the phenomenon of lightning discharge realization [11–15]. According to the existing concepts, lightning discharge initiation results from the powerful electron avalanche (turning into a streamer) arising at a corona discharge from a group of closely located drops or melting hail stones falling inside a storm cloud [11–13]. However, in situ measurements inside storm clouds of the in-cloud electric fields and the charges on the drops and hail stones show (see, e.g., [14, ch. 10]) that the electric field intensities and charge values on the drops and hail stones are not great enough both for the realization of the electrostatic instability of the liquid surface in relation to the intrinsic and induced charges [1] and for the corona discharge ignition. The measured intensities of the in-cloud electric fields and the charges of the drops and hail stones are too small to enable the summarized intensity of the electrostatic field of the induced and intrinsic charges (at the undisturbed drops or water-bearing hail in the clouds) to reach the value of ~20 kV/cm required for the corona discharge ignition [15, p. 507] at a height of 4–5 km (where the air pressure changes in the range of 460–400 mm Hg) at the level of the wet growth of the hail and intensive separation of the electric charges. At the same time, it is known that the deformation of the charged free surface of the liquid in the external electric field causing the local increase of the surface curvature also results in the local increase of the electric field intensity proportional to the amplitude of the deformation [1, 16 and 17], which, when occurring in the direct vicinity of the drop, may exceed the value crucial for the corona discharge ignition.

In papers [18, 19], it has been shown that the electric field intensity required for corona discharge ignition may be observed at the tops of nonlinearly oscillating weakly charged drops. It should be noted that the problems concerning the electric field intensity calculation in the vicinity of a nonlinearly oscillating drop have already been solved (see, e.g., [18–20]). However, there were mentioned either only the external electric field or only the charge, while, in real conditions, both of them are present [14].

1. SETTING OF THE PROBLEM

We are to solve the problem concerning the location of the electric field intensity in the vicinity of the surface of a nonlinearly oscillating spherical ideally incompressible conducting drop (with the radius R, the density ρ, the coefficient of the surface tension σ, and the charge Q) located in a uniform electrostatic field with the intensity E_0. All of the study is to be performed using a simplified model assuming that the drop moves with respect to the medium parallel to the external electric field where both the medium and its aerodynamic resistance to the drop motion are not taken into consideration. The role of the medium in the proposed model will be reduced to providing the drop with uniform and linear motion, and the entire examination will be carried out in a spherical coordinate system correlated

with the drop mass center in dimensionless alternatives in which $R = \sigma = \rho = 1$. Let us assume that, at the initial moment of time ($t = 0$), the equilibrium spherical form of the free surface of the liquid layer endured virtual axisymmetric deformation of finite amplitude considerably smaller than the radius R proportional to one of the modes of the capillary drop oscillations. The equation of the liquid free surface will be written as follows:

$$F(r, \vartheta, t) = r - 1 - \xi(\vartheta, t) = 0, \quad |\xi| \ll 1. \tag{1}$$

The liquid flow in the drop is assumed to be potential; i.e., we shall accept that the field of rates $V(r, t)$ of the wave motion in the liquid can be totally determined by the potential of the field of rates $\psi(r, t)$ by the known correlation $V(r, t) \equiv \nabla\psi(r, t)$.

The mathematical formulation of the problem on the calculation of the nonlinear oscillations of a drop consists of the Laplace equations for the potential of the field of rates $\psi(r, t)$ and the electrostatic potential $\Phi(r, t)$:

$$\Delta\psi(r, t) = 0; \quad \Delta\Phi(r, t) = 0;$$

along with the boundary conditions for them at the free surface of the liquid:

kinematic

$$r = 1 + \xi: \quad \frac{\partial\xi}{\partial t} = \frac{\partial\psi}{\partial r} - \frac{1}{r^2}\frac{\partial\psi}{\partial\vartheta}\frac{\partial\xi}{\partial\vartheta};$$

dynamic

$$-\frac{\partial\psi}{\partial t} - \frac{1}{2}(\nabla\psi)^2 + \Delta p + p_E - p_\sigma = 0;$$

$$p_E \equiv (\nabla\Phi)^2/8\pi; \quad p_\sigma = \operatorname{div} n;$$

the constancy of the electric potential of the free surface of the liquid

$$\Phi(r, t) = \Phi_S(t);$$

and the boundary conditions at infinity

$$r \longrightarrow \infty: \quad -\nabla\Phi(r, t) \longrightarrow E_0;$$

and in the center of a drop

$$r = 0: \quad \nabla\psi \longrightarrow 0.$$

In the written correlations, Δp is the differential of the constant pressures inside and outside the liquid at a balanced state, p_E is the electric field pressure of the self-charge and the external field on the free surface of a drop, p_σ is the Laplace pressure, $n \equiv \nabla F(r, \vartheta, t)/|\nabla F(r, \vartheta, t)|$ is the unit vector of the outer normal to the surface of the liquid layer, and $\Phi_S(t)$ is the constant electric potential along the free surface of the liquid.

Apart from the above boundary conditions, a number of other conditions should also be considered:

—the permanencies of the intrinsic electric charge of the system

$$-\frac{1}{4\pi}\oint_S (n \cdot \nabla\Phi) dS = Q;$$

$$S = \begin{cases} r = 1 + \xi(\vartheta, t); \\ 0 \le \vartheta \le \pi; \\ 0 \le \varphi \le 2\pi; \end{cases}$$

—the permanencies of the liquid volume

$$\int_V r^2 dr d\mu d\varphi = -\frac{4}{3}\pi;$$

$$V = \begin{cases} 0 \le r \le 1 + \xi(\vartheta, t); \\ 0 \le \vartheta \le \pi; \\ 0 \le \varphi \le 2\pi. \end{cases} \qquad \mu \equiv \cos\vartheta;$$

—the fixednesses of the drop mass center

$$\int_V r d\mu d\varphi = 0.$$

The initial conditions for the set problem shall be formulated as the task of the initial axisymmetric deformation of the equilibrium spherical form of the free surface of a drop and the equality to zero of the initial rate of motion of the free surface:

$$t = 0:$$

$$\xi(\vartheta, t) = \xi_0 \cdot P_0(\mu) + \xi_1 \cdot P_1(\mu) + \varepsilon \cdot P_k(\mu);$$

$$(k \ge 2); \quad \frac{\partial\xi(\vartheta, t)}{\partial t} = 0.$$

Here, ε is the dimensionless amplitude of the initial deformation, being a minor parameter of the problem; $P_k(\mu)$ is the polynom of Legendre of the k-th order; and ξ_0 and ξ_1 are the constants determined by the conditions of the permanency of the liquid layer volume and the fixedness of the system's center of mass.

It can be easily shown that if at the initial moment of time only one k-mode is energized, then

$$\xi_0 = -\varepsilon^2\frac{1}{(2k+1)} + O(\varepsilon^3); \quad \xi_1 = 0 + O(\varepsilon^3).$$

2. THE PROBLEM'S SOLUTION

The formulated problem at the ε quadratic approximation will be solved by the method of multitime scales [21] as has been done before for solving similar problems [18–20]. For this purpose, the required functions $\xi(\vartheta, t)]$, $\Psi(r, t)$, and $\Phi(r, t)$, which will be presented in the form of asymptotic expansions of the minor parameter degrees ε, are considered to be dependent not

merely on the time t but also on its various scales T_m defined by the ratio $T_m \equiv \varepsilon^m \cdot t$:

$$\xi(\vartheta, t) = \sum_{m=1}^{\infty} \varepsilon^m \cdot \xi^{(m)}(\vartheta, T_0, T_1, \ldots);$$

$$\Psi(r, t) = \sum_{m=1}^{\infty} \varepsilon^m \cdot \psi^{(m)}(r, \vartheta, T_0, T_1, \ldots); \quad (2)$$

$$\Phi(r, t) = \sum_{m=0}^{\infty} \varepsilon^m \cdot \Phi^{(m)}(r, \vartheta, T_0, T_1, \ldots).$$

The derivatives of the time are calculated according to the rule in [21]:

$$\frac{\partial}{\partial t} = \frac{\partial}{\partial T_0} + \varepsilon\frac{\partial}{\partial T_1} + \varepsilon^2\frac{\partial}{\partial T_2} + O(\varepsilon^3). \quad (3)$$

Inserting expansions (2) and (3) into the formulated boundary problem and equating the terms of one order of infinitesimals in each of the correlations, one will easily obtain the set of boundary problems for the sequential definition of the unknown functions $\xi^{(m)}$, $\psi^{(m)}$, and $\Phi^{(m)}$, which, for $m \geq 1$, we shall search in the form of a series using Legendre's polynom:

$$\xi^{(m)}(\vartheta, T_0, T_1, \ldots) = \sum_{n=0}^{\infty} M_n^{(m)}(T_0, T_1, \ldots)P_n(\mu).$$

$$\psi^{(m)}(r, \vartheta, T_0, T_1, \ldots) = \sum_{n=0}^{\infty} S_n^{(m)}(T_0, T_1, \ldots)r^n P_n(\mu).$$

$$\Phi^{(m)}(r, \vartheta, T_0, T_1, \ldots) = \sum_{n=0}^{\infty} F_n^{(m)}(T_0, T_1, \ldots)r^{-n-1}P_n(\mu).$$

3. SEARCHING FOR THE SOLUTIONS OF VARIOUS ORDERS OF INFINITESIMALS

Omitting the details of the mathematical procedure for searching for the solutions scrutinized in [18–21], we shall straightforwardly present the ultimate solution of the formulated problem:

$$\xi(\theta, t) = \varepsilon\xi^{(1)}(\vartheta, t) + \varepsilon^2\xi^{(2)}(\vartheta, t) + O(\varepsilon^3 t) = \varepsilon\sum_{n=0}^{\infty} M_n^{(1)}(T_0)P_n(\mu) + \varepsilon^2\sum_{n=0}^{\infty} M_n^{(2)}(T_0)P_n(\mu) + O(\varepsilon^3 t);$$

$$\Psi = \varepsilon\psi^{(1)} + \varepsilon^2\psi^{(2)} \equiv \varepsilon\sum_{n=0}^{\infty}(G_n^{(1)}(T_0) + \varepsilon G_n^{(2)}(T_0))r^n P_n(\mu) + O(\varepsilon^3 t);$$

$$\Phi = \Phi^{(0)} + \varepsilon\Phi^{(1)} + \varepsilon^2\Phi^{(2)} \equiv \frac{Q}{r} - E_0 r\mu(1 - r^{-3}) + \varepsilon\sum_{n=0}^{\infty}(F_n^{(1)}(T_0) + \varepsilon F_n^{(2)}(T_0))r^{-(n+1)}P_n(\mu) + O(\varepsilon^3 t),$$

where

$$M_0^{(1)}(T_0, T_1, \ldots) \equiv 0; \quad M_1^{(1)}(T_0, T_1, \ldots) \equiv 0;$$

$$n \geq 2; \quad A_n M_{n-2}^{(1)}(T_0, T_1, \ldots) + B_n\frac{\partial M_{n-1}^{(1)}(T_0, T_1, \ldots)}{\partial T_0} + \frac{\partial^2 M_{n-1}^{(1)}(T_0, T_1, \ldots)}{\partial T_0^2} + \omega_n^2 M_n^{(1)}(T_0, T_1, \ldots) \quad (4)$$
$$+ C_n\frac{\partial M_{n+1}^{(1)}(T_0, T_1, \ldots)}{\partial T_0} + D_n M_{n+2}^{(1)}(T_0, T_1, \ldots) = 0;$$

$$A_n = -w\frac{n^2(n-1)(n-2)}{(2n-3)(2n-1)};$$

$$B_n = -\sqrt{wW}\frac{n(n+1)(2n-1)}{(2n+3)};$$

$$C_n = -\sqrt{wW}\frac{n^2(2n-3)}{(2n-1)};$$

$$D_n = -w\frac{n^2(n+1)(n+2)}{(2n+3)(2n+5)}; \quad w = \frac{9E_0^2}{4\pi}; \quad W = \frac{Q^2}{4\pi};$$

$$\omega_n^2 = n(n-1)(n+2) - w\frac{n^2(4n^3 + 2n^2 - 6n - 1)}{(2n-1)(2n+1)(2n+3)} - n(n-1)W;$$

$$G_n^{(1)}(T_0, T_1, \ldots) = \frac{1}{n}\frac{\partial M_n^{(1)}(T_0, T_1, \ldots)}{\partial T_0};$$

$$F_0^{(1)}(T_0, T_1, \ldots) \equiv 0; \quad F_1^{(1)}(T_0, T_1, \ldots) \equiv 0;$$

$$F_n^{(1)}(T_0, T_1, \ldots) = QM_n^{(1)}(T_0, T_1, \ldots) + 3E_0\left(\frac{n}{2n-1}M_{n-1}^{(1)}(T_0, T_1, \ldots) + \frac{n+1}{2n+3}M_{n+1}^{(1)}(T_0, T_1, \ldots)\right); \quad n \geq 2;$$

$$\Phi_S^{(1)} \equiv 0;$$

$$\Phi^{(1)} = \sum_{n=0}^{\infty} F_n^{(1)}(T_0, T_1, \ldots) r^{-(n+1)} P_n(\cos\theta);$$

$$M_0^{(2)}(T_0) = \sum_{n=0}^{\infty} \frac{1}{2n+1} (M_n^{(1)}(T_0))^2;$$

$$A_n M_{n-2}^{(2)}(T_0, T_1, \ldots) + B_n \frac{\partial M_{n-1}^{(2)}(T_0, T_1, \ldots)}{\partial T_0} + \frac{\partial^2 M_n^{(2)}(T_0, T_1, \ldots)}{\partial T_0^2} + \omega_n^2 M_n^{(2)}(T_0, T_1, \ldots) + C_n \frac{\partial M_{n+1}^{(2)}(T_0, T_1, \ldots)}{\partial T_0} + D_n M_{n+2}^{(2)}(T_0, T_1, \ldots) = H_n(T_0); \quad (n \geq 1;) \tag{5}$$

$$H_n(T_0) = \sum_{m=2}^{\infty} \sum_{l=2}^{\infty} \left\{ M_m^{(1)}(T_0) M_l^{(1)}(T_0) \times \left\{ K_{m,l,n} \left(2n[l(l+1)-1] + We \frac{n(13m(m+1)-7)}{(2m-1)(2m+3)} + W\frac{n}{2}[m(2n-2m+l-7)+l+3] \right) + \frac{11nWe}{2(2m+1)} \left[\frac{m(m-1)}{(2m-1)} K_{m-2,l,n} + \frac{(m+1)(m+2)}{(2m+3)} K_{m+2,l,n} \right] - \frac{n\sqrt{WeW}}{(2m+1)} [K_{m+1,l,n}(m+1)((m+2)^2-11) + K_{m-1,l,n} m((m+3)^2-15)] + nm\sqrt{WeW} \times \left[\frac{(n+1)(n+2)}{2n+3} K_{m,l,n+1} + \frac{n^2}{2n-1} K_{m,l,n-1} \right] + W\frac{n}{2}\alpha_{m,l,n-1} \right\} + \left(\frac{nm}{(2m-1)} M_{m-1}^{(1)}(T_0) + \frac{n(m+1)}{(2m+3)} M_{m+1}^{(1)}(T_0) \right) M_l^{(1)}(T_0) \times \left\{ mWe \left[\frac{n^2}{2m-1} K_{m,l,n-1} + \frac{(n+1)(n+2)}{2m+3} K_{m,l,n+1} \right] - We\frac{m+1}{2m+3}[(m+2)^2 K_{m+1,l,n} + m(m+5) K_{m-1,l,n}] + \frac{1}{2}\sqrt{WeW}[(l-7+m(2n-7-2m+l)) K_{m,l,n} + \alpha^{m,l,n}] \right\} + \frac{n}{2}[(m+1)(l+1) K_{m,l,n} + \alpha_{m,l,n}] \times \left(\frac{l M_{l-1}^{(1)}(T_0)}{(2l-1)} + \frac{(l+1) M_{l+1}^{(1)}(T_0)}{(2l+3)} \right) \left\{ \sqrt{WeW} M_m^{(1)}(T_0) + We \left(\frac{m M_{m-1}^{(1)}(T_0)}{2m-1} + \frac{(m+1) M_{m+1}^{(1)}(T_0)}{2m+3} \right) \right\} + \frac{\partial^2 M_m^{(1)}(T_0)}{\partial T_0^2} M_l^{(1)}(T_0) \left[(m-n-1) K_{m,l,n} - \frac{\alpha_{m,l,n}}{m} \right] + \frac{\partial M_m^{(1)}(T_0)}{\partial T_0} \frac{\partial M_l^{(1)}(T_0)}{\partial T_0} \left[\left(m-1-\frac{n}{2} \right) K_{m,l,n} - \frac{n+2l}{2ml} \alpha_{m,l,n} \right] + K_{m,l,n} \equiv [C_{m0l0}^{n0}]^2;$$

$$\alpha_{m,l,n} \equiv -\sqrt{m(m+1)l(l+1)}\, C_{m0l0}^{n0} \cdot C_{m-1l0}^{n0};$$

$$G_n^{(2)}(T_0) = \frac{1}{n} \left(\frac{\partial M_n^{(2)}(T_0)}{\partial T_0} - \sum_{m=2}^{\infty} \sum_{l=2}^{\infty} \left[(m-1) K_{m,l,n} - \frac{\alpha_{m,l,n}}{m} \right] \frac{\partial M_m^{(1)}(T_0)}{\partial T_0} M_l^{(1)}(T_0) \right);$$

$$\Phi_S^{(2)} \equiv 0; \quad F_0^{(2)}(T_0) = 0;$$

$$F_n^{(2)}(T_0) = Q M_n^{(2)}(T_0) + 3E_0 \times \left(\frac{n}{2n-1} M_{n-1}^{(2)}(T_0) + \frac{n+1}{2n+3} M_{n+1}^{(2)}(T_0) \right) + \sum_{m=1}^{\infty} \sum_{l=1}^{\infty} \left[3E_0 \left(\frac{m^2}{2m-1} M_{m-1}^{(1)}(T_0) + \frac{m(m+1)}{2m+3} M_{m+1}^{(1)}(T_0) \right) + mQ M_m^{(1)}(T_0) \right] \times K_{m,l,n} M_l^{(1)}(T_0); \quad n \geq 1.$$

C_{m0l0}^{n0} and C_{m-1l0}^{n0} are the Clebsch–Gordan coefficients.

As is seen from the written expressions, the coefficients $F_n^{(j)}(T_0, T_1, \ldots)$ and $G_n^{(j)}(T_0, T_1, \ldots)$ are expressed through $M_n^{(j)}(T_0, T_1, \ldots)$, which may be defined by way of the numerical solution of the coupled systems of differential equations (4) and (5).

4. THE CALCULATION OF THE ELECTRIC FIELD INTENSITY NEAR THE SURFACE OF A CHARGED HAIL STONE

The expression for the electrostatic field intensity $E(r, t) \equiv -\nabla\Phi(r, t)$ in the vicinity of the free surface of the nonlinearly oscillating charged liquid layer is as follows:

$$r \geq 1 + \xi(\vartheta, t): \quad E = E^{(0)} + \varepsilon \sum_{m \in \Omega} E_m^{(1)} + \varepsilon^2 \sum_{n=0} E_n^{(2)};$$

$$E^{(0)} = e_r\left(E_0\mu\left(1 + \frac{2}{r^3}\right) + \frac{Q}{r^2}\right) + e_\vartheta\left(E_0\sqrt{1-\mu^2}\left(1 + \frac{1}{r^3}\right)\right);$$

$$\begin{aligned} E^{(1)} &= e_r \sum_{n=0}^{\infty} (n+1) F_n^{(1)} r^{-(n+2)} P_n(\mu) \\ &\quad - e_\vartheta \sum_{n=0}^{\infty} F_n^{(1)} r^{-(n+2)} \frac{\partial P_n(\mu)}{\partial \vartheta}; \end{aligned} \tag{6}$$

$$\begin{aligned} E^{(2)} &= e_r \sum_{n=0}^{\infty} (n+1) F_n^{(2)} r^{-(n+2)} P_n(\mu) \\ &\quad - e_\vartheta \sum_{n=0}^{\infty} F_n^{(2)} r^{-(n+2)} \frac{\partial P_n(\mu)}{\partial \vartheta}, \end{aligned}$$

where e_r and e_ϑ are the unit vectors of the spherical system of coordinates. From the obtained expression, we shall find the intensity of the electric field at the undisturbed spherical surface of the free surface of the liquid layer. For this purpose, let us decompose (6) in the vicinity of the equilibrium spherical form by the amplitude of the deformation. Also, we shall define the derivatives using the following coordinates:

$$\begin{aligned} &E(r, \vartheta, t)\big|_{r=1+\xi} \\ &\approx \left[E(r, \vartheta, t) + \xi \frac{\partial E(r, \vartheta, t)}{\partial r} + \frac{1}{2}\xi^2 \frac{\partial^2 E(r, \vartheta, t)}{\partial r^2}\right]\Bigg|_{r=1} \\ &= e_r\{3E_0\mu + Q\} + \varepsilon e_r \\ &\times \sum_{n=0}^{\infty} \{(1+n)F_n^{(1)} - 2(3E_0\mu + Q)M_n^{(1)}\} P_n(\mu) \\ &- \varepsilon e_\vartheta \sum_{n=0}^{\infty} \left\{F_n^{(1)} \frac{\partial P_n(\mu)}{\partial \vartheta} + 3E_0\sqrt{1-\mu^2} M_n^{(1)} P_n(\mu)\right\} \\ &+ \varepsilon^2 e_r \sum_{n=0}^{\infty} \{(1+n)F_n^{(2)} - 2(3E_0\mu + Q)M_n^{(2)}\} P_n(\mu) \\ &+ \varepsilon^2 e_r \sum_{m=0}^{\infty} \sum_{l=0}^{\infty} [3(4E_0\mu + Q)M_m^{(1)} M_l^{(2)} \\ &- (m+1)(m+2)M_m^{(1)} F_l^{(1)}] P_m(\mu) P_l(\mu) \\ &+ \varepsilon^2 e_\vartheta \sum_{n=0}^{\infty} F_n^{(2)} \frac{\partial P_n(\mu)}{\partial \vartheta} + 3E_0\sqrt{1-\mu^2} M_n^{(2)} P_n(\mu) \\ &+ \varepsilon^2 e_\vartheta \sum_{m=0}^{\infty} \sum_{l=0}^{\infty} \left[(m+2)F_m^{(1)} \frac{\partial P_m(\mu)}{\partial \vartheta} \right. \\ &\left. + 6E_0\sqrt{1-\mu^2} M_l^{(1)} P_m(\mu)\right] M_l^{(1)} P_l(\mu). \end{aligned} \tag{7}$$

In order to find the normal constituent of the electric field in the vicinity of the free surface of the nonlinearly oscillating liquid layer $E_n = n \cdot E$, let us write in the explicit form the analytic expression for the vector of the normal to the free surface of the liquid layer:

$$n \equiv \nabla F(r, \vartheta, t)/|\nabla F(r, \vartheta, t)| \equiv n_r \cdot e_r + n_\vartheta \cdot e_\vartheta. \tag{8}$$

Within the accuracy of the items of the second order of the infinitesimals by ε in the vicinity of the free surface of the projections n_r and n_ϑ at the unit vectors of the spherical system of coordinates e_r and e_ϑ, the vectors of the normal are defined by the following expressions:

$$\begin{aligned} r = 1: \quad n_r &= 1 - \varepsilon^2 \frac{1}{2}(\partial_\vartheta \xi^{(1)})^2 \\ &= 1 - \varepsilon^2 \frac{1}{2}\left(\cos(\omega_k t) \frac{\partial P_k(\mu)}{\partial \vartheta}\right)^2; \end{aligned}$$

$$\begin{aligned} n_\vartheta &= -\varepsilon \partial_\vartheta \xi^{(1)} + \varepsilon^2(\xi^{(1)} \partial_\vartheta \xi^{(1)} + \partial_\vartheta \xi^{(2)}) \\ &= -\varepsilon \cos(\omega_k t) \frac{\partial P_k(\mu)}{\partial \vartheta} \\ &+ \varepsilon^2 \left([\cos(\omega_k t)]^2 P_k(\mu) \frac{\partial P_k(\mu)}{\partial \vartheta} + \sum_{j=0}^{k} M_{2j}^{(2)}(t) \frac{\partial P_{2j}(\mu)}{\partial \vartheta} \right). \end{aligned}$$

The scalar product of expressions (7) and (8) considering n_r and n_ϑ will give the expression for the normal constituent of the electric field at the hail-stone surface:

$$\begin{aligned} E_n &= 3E_0\mu + Q \\ &+ \varepsilon \sum_{n=0}^{\infty} \{(1+n)F_n^{(1)} - 2(3E_0\mu + Q)M_n^{(1)}\} P_n(\mu) \\ &+ \varepsilon^2 \sum_{n=0}^{\infty} \{(1+n)F_n^{(2)} - 2(3E_0\mu + Q)M_n^{(2)} \\ &+ \sum_{m=0}^{\infty} \sum_{l=0}^{\infty} \left\{\left[3(4E_0\mu + Q)M_m^{(1)} M_l^{(2)} \right.\right. \\ &\left.\left. - (m+1)(m+2)M_m^{(1)} F_l^{(1)}\right] K_{m,l,n} \right. \end{aligned} \tag{9}$$

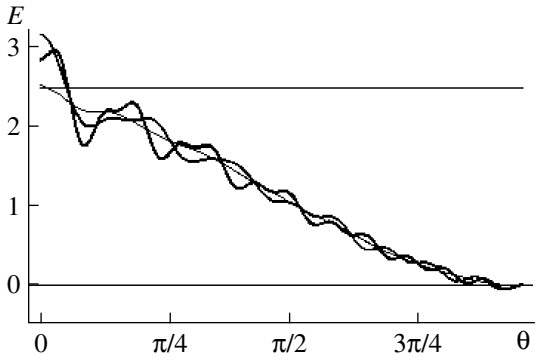

Fig. 1. The dependency on the azimuth ϑ of the value of the dimensionless intensity of the electric field at the surface of a drop at the moment of time $t = 1$ for various modes that define the initial deformation: $k = 8$ (the thin curve), $k = 10$ (the curve of average thickness), $k = 12$ (the thick curve). $W = 0.1$, $w = 0.1$, and $\varepsilon = 0.1$.

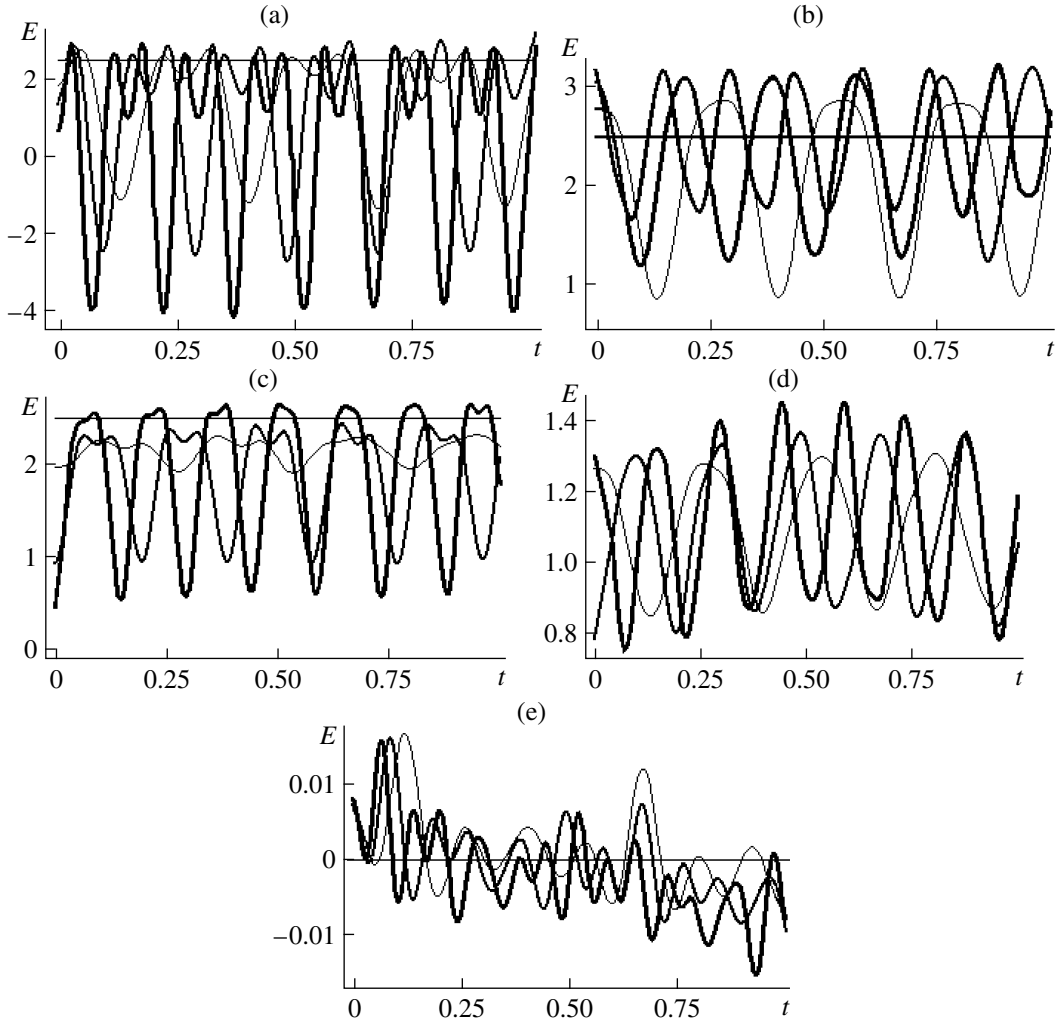

Fig. 2. The dependence on the dimensionless time of the value of the dimensionless intensity of the electric field in the vicinity of the free surface of a drop for various modes that define the initial deformation: $k = 8$ (the thin curve), $k = 10$ (the curve of average thickness), $k = 12$ (the thick curve). At $W = 0.1$, $w = 0.1$, $\varepsilon = 0.1$, and at various angles ϑ with respect to the axis of symmetry of the drop: (a) 0; (b) 0.15; (c) 0.3; (d) π/2; (e) π.

$$+ [F_m^{(1)} M_l^{(2)} - (3E_0\mu + Q) M_m^{(1)} M_l^{(1)}] \alpha_{m,l,n}$$

$$+ \frac{3m(m+1)}{2m+1} E_0 M_m^{(1)} M_l^{(1)} [\alpha_{m+1,l,n} - \alpha_{m-1,l,n}] \Bigg\} P_n(\mu).$$

5. DISCUSSION OF THE RESULTS

Figures 1 and 2 illustrate the results of the calculation of correlation (9). In all the figures, the straight line $E = 2.5$ parallel to the X-axis is relevant to the dimensionless intensity of the electrostatic field of 20 kV/cm critical for the corona discharge ignition in a storm cloud at a height of ≈4–5 km.

ACKNOWLEDGMENTS

This work was performed within the framework of the Topical University Plan with the support of the Russian Education Foundation (project no. 2.1.1/3776) and the Russian Foundation for Basic Research (project nos. 09-01-00084 and 09-08-00148).

REFERENCES

1. Grigor'ev, A.I. and Shiryaeva, S.O., Capillary Instabilities of the Charged Surface of Drops and Electrodispersion of Liquids, *Izv. Ros. Akad. Nauk*, 1994, no. 3, pp. 3–22.
2. Grigor'ev, A.I., Shiryaeva, S.O, Zharov, A.N., and Koromyslov, V.A., Non-Linear Oscillations of the Charged Drops (Review). Part 1., *Surf. Eng. Appl. Electrochem.*, 2005, no. 3, pp. 25–35.
3. Grigor'ev, A.I., Shiryaeva, S.O, Zharov, A.N., and Koromyslov, V.A., Non-Linear Oscillations of the Charged Drops (Review). Part 2., *Surf. Eng. Appl. Electrochem.*, 2005, no. 4, pp. 24–34.
4. Muchnik, V.M. and Fishman, B.E., *Elektrizatsiya grubodispersnykh aerozolei v atmosphere* (Electrization of Coarse-Dispersive Aerosols in the Atmosphere), Leningrad: Gidrometeoizdat, 1983.
5. Mazin, I.P. and Shmeter, S.M., *Oblaka. Stroenie i fizika obrazovaniya* (Clouds. Structure and Physics of Formation), Leningrad: Gidrometeoizdat, 1983.
6. Dudnikov, V.G. and Shabalin, A.L., Electrohydrodynamic Sources of Ion Beams (Review), *Preprint of Inst. Nucl. Phys., Sib. Dpt. of USSR Acad. Sci.*, Novosibirsk, 1987, no. 87–63.
7. Grigor'ev, A.I. and Shiryaeva, S.O., Electrodynamic Aspects of Functioning of Liquid-Metal Sources of Ions, *Zh. Tekh. Fiz.*, 1992, Vol. 62, issue 12, pp. 9–20.
8. Gall', L.N., Krasnov, V.N., et al., Electrohydrodynamic Introduction of Liquid Substances into Mass-Spectometer, *Zh. Tekh. Fiz.*, 1992, Vol. 62, issue 12, pp. 9–20.
9. Zolotoi, N.B., Karpov, G.V., and Skurat, V.E., On the Mechanism of Ion Formation and Ionic Clusters from the Charged Drops, *Zh. Tekh. Fiz.*, 1988, Vol. 58, issue 2, pp. 315–323.
10. Kozhevnikov, V.I. and Fuks, N.A., Electrohydrodynamic Diffusion of the Liquid (Review), *Uspekhi khimii*, 1976, Vol. 45, no. 12, pp. 2274–2284.
11. D'yachuk, V.A. and Muchnik, V.A., Corona Discharge from the Water-Bearing Heil-Stone, the Main Mechanism of Lightning Initiation, *Dokl. Akad. Nauk SSSR*, 1979, Vol. 248, no. 1, pp. 60–63.
12. Beituganov, M.N., On the Physical Phenomena in the Clouds Provided by the Strong Electric Fields, *Meteorologiya i gidrologiya*, 1989, no. 9, p. 49.
13. Grigor'ev, A.I. and Shiryaeva, S.O., The Possible Physical Mechanism of Initiation and Growth of Lightning, *Physica Scripta*, 1966, Vol. 54, pp. 660 –666.
14. *Oblaka i oblachnaya atmosfera. Spravochnik* (a Handbook on Clouds and Cloudy Atmosphere), Mazin, I.P., Khrgian, A.Kh., and Imyanitov, I.M. (Eds.), Leningrad: Gidrometeoizdat, 1989.
15. Raizer, Yu.P., *Fizika gazovogo razryada* (Physics of Gas Discharge), Moscow: Nauka, 1987.
16. Shiryaeva, S.O., Grigor'ev, A.I., and Belonozhko, D.F., On Certain Regularities of Realization of Instability Plane Charged Surface of Liquid, *Zh. Tekh. Fiz.*, 1999, Vol. 69, issue 7, pp. 15–22.
17. Grigor'ev, A.I., On Certain Regularities of Realization of Instability of Strongly Charged Viscous Drop, *Zh. Tekh. Fiz.*, 2001, vol. 71, issue 10, pp. 1–7.
18. Grigor'ev, A.I., Shiryaeva, S.O., and Volkova, M.V., On Possibility of the Corona Dischrge Ignition in the Vicinity of a Non-Linearly Oscillating Weakly Charged Drop, *Zh. Tekh. Fiz.*, 2003, Vol. 73, issue 11, pp. 31–36.
19. Grigor'ev, A.I., Koromyslov, V.A., and Shiryaeva, S.O., On Possibility of the Corona Dischrge Ignition Near the Surface of a Non-Linearly Oscillating Liquid Layer at the Surface of a Charged Heil-Stone, *Zh. Tekh. Fiz.*, 2009, Vol. 79, issue 11, pp. 10–19.
20. Shiryaeva, S.O., Grigor'ev, A.I., and Volkova, M.V., On Possibility of the Corona Dischrge Ignition in the Vicinity of Non-Linearly Oscillating in the External Electrostatic Field of the Electroconductive Drop, *Zh. Tekh. Fiz.*, 2005, Vol. 75, issue 7, pp. 40–47.
21. Naife, A., *Metody vozmushchenii* (Methods of Perturbations), Moscow: Mir, 1983.

ISSN 1068-3755, Surface Engineering and Applied Electrochemistry, 2009, Vol. 45, No. 6, pp. 502–506. © Allerton Press, Inc., 2009.
Original Russian Text © V.Yu. Baklar', N.I. Kuskova, A.N. Yushchishina, 2009, published in Elektronnaya Obrabotka Materialov, 2009, No. 6, pp. 80–85.

ELECTRICAL PROCESSING OF BIOLOGICAL OBJECTS AND FOOD PRODUCTS

Electrodischarge Treatment of Alcohols to Produce Carbonic Nanomaterials

V. Yu. Baklar', N. I. Kuskova, and A. N. Yushchishina

Institute of Pulse Processes and Technologies, National Academy of Sciences of Ukraine, pr. Oktyabrskii 43a, Nikolaev, 54018 Ukraine

e-mail: iipt@iipt.com.ua

Received April 28, 2009

Abstract—The method and products of the electrodischarge treatment of alcohols have been studied. The method of separation of the CNM produced from inferior alcohols by the high-voltage electrophoresis method has been proposed and tested. As the X-ray diffraction analysis results show, the application of only the electrophoresis method is not enough for the complete separation of the crystallites into the different allotropic forms of carbon. It is necessary to use complex methods of the CNM enrichment.

DOI: 10.3103/S106837550906012X

INTRODUCTION

There exist three excited states of carbon C connected with hybridization (by the method of the formation of atom orbitals with consideration for the repulsion of the valence shell electron pairs) of 2*s*- and 2*p*-atom orbitals. The hybridization degree can be expressed as sp^n. The exponent $n = 3$ is inherent in the three-dimensional carbon polymer diamond, $n = 2$ in planar graphite, and $n = 1$ in linear-chain carbine. There also exist the transient (mixed and intermediate) forms of elementary carbon. The forms with mixed short-range ordering consist of accidentally organized atoms of carbon of different hybridization (it is an "amorphous" carbon), as well as black coke and similar materials. The second group unites the intermediate carbon forms for which n is not a whole number but a fractional one ($1 < n < 3$); they are carbonic monocycles and various closed-skeleton structures such as fullerenes and carbonic nanotubes (CNT) [1].

The C excited state connected with sp^2-hybridization is the reason for the existence of alkenes (C_nH_{2n}), among these is ethylene, polyacetylene, and so on. Alkenes are chemically active; their chemical properties are determined by the presence of the double bond. It is possible to produce alkenes through catalytic dehydration of alcohols. Thus, the dehydration of ethanol results in the synthesis of ethylene:

$$CH_3–CH_2–OH \longrightarrow CH_2=CH_2 + H_2O. \quad (1)$$

As the view of the shock adiabats shows, substantial changes (being the consequence of the breakdown of the covalent bonds between the atoms of C and H and the formation of new C–C and molecular hydrogen H–H bonds) take place in the structure of organic substances at compression by shock waves. The results of experiments on multistep shock compression of some organic liquids put into special "conservation ampoules" showed that, after the passage of the shock waves (with maximum pressures up to 40 GPa), there remained an amorphous black powder in the surviving ampoules [1]. The decomposition of the original structures into their constituent elements is an important outcome of these experiments.

It is supposed that the synthesis of fullerenes, CNT, diamond, and carbine from organic compounds with the hybridization degree being the same or near to the hybridization degree of the produced material will occur with a minimum consumption of energy. Thus, it is necessary to look for substances suitable for producing new materials with the prescribed degree of hybridization of carbon atoms n in the class of compounds in which carbon has like values of the hybridization degree.

The purpose of this work is to produce carbonic nanomaterials (CNM) through electrodischarge treatment and to separate and investigate them.

PRODUCTION OF CNM THROUGH ELECTRODISCHARGE TREATMENT OF ALCOHOLS

The electrodischarge method is one of the proficient ways of impulse action on a substance [2–4]. Under the action of powerful electrodischarge current impulses on hydrocarbons, there appears a region of high pressure and temperatures in which the destruction and decomposition of hydrocarbon molecules into their constituent elements occurs according to the scheme

$$C_nH_m \longrightarrow nC + 0.5mH_2.$$

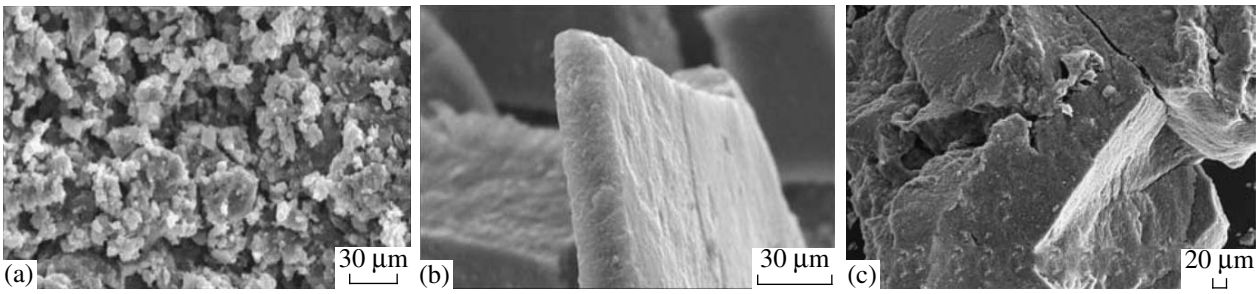

Fig. 1. Microphotos of carbon particles produced at the treatment of alcohols: a—ethyl; b—butyl; c—isoamyl.

In this case, the carbon is liberated as a solid phase in different allotropic states, and hydrogen is released in the gaseous form.

We studied the processes going on at the electrodischarge treatment of alcohols. As the C–O bond breakdown energy in alcohols $\varepsilon = 333.1$ kJ/mol is smaller than the C–H bond energy, with the alcohols being affected by the high temperature in the course of the electrodischarge treatment, there initially occurs their dehydration according to scheme (1) with the generation of alkenes (C_nH_{2n}). Gaseous alkenes will first be liberated in the liquid and subjected to the further electrodischarge treatment.

In the course of intensive electrodischarge treatment, the breakdown of intercarbon bonds is also possible.

The energy necessary for the proceeding of the mentioned chemical reactions in the local area of the spark effect (in a volume of an alcohol with the mass m) can be calculated by the expression

$$E_i = \frac{\varepsilon_i m}{M},$$

where M is the alcohol's molecule molar mass, and ε_i is the bond energy.

The C-H energy bond in molecules of alkenes $\varepsilon_1 = 433$ kJ/mol is smaller than the C+C double bond energy $\varepsilon_2 = 588$ kJ/mol; thus, it can be assumed that, by selecting the energy of a single electrodischarge effect W in the alcohol local volume in the range $E_1 < W < E_2$, it is possible to produce carbon having predominantly sp^2 hybridization in the solid phase.

The possibility is shown of the proficient synthesis of nanocarbon in macroamounts at the electrodischarge action on alcohols. The powders are roentgen amorphous; i.e., they contain a mixture of various allotropic forms of carbon.

Microphotos of CNM particles obtained through the electrodischarge treatment of ethyl C_2H_5OH, butyl $CH_3(CH_2)_2CH_2OH$, and isoamyl ($(CH_3)_2CH(CH_2)_2OH$) alcohols are presented in Fig. 1. It is well seen that the powder particles have a regular layer structure with their size reducing as the length of the carbon chain of the initial alcohol molecules decreases.

During the drying process, the powder greatly aggregates up to particle sizes of about several tens of μm due to the high chemical activity and large specific surface of the carbon nanoparticles (from 150 to 250 m^2/g).

The regularities of the distribution of the powder particles according to their size, area, and form factor have been studied with the help of the program MEGRAN (designed by the Admiral Makarov National University of Shipbuilding in Nikolaev). Based on the data of the computer processing of the microphotos of the powder, it is possible to reach a conclusion concerning the variety of the obtained forms of ultradispersed carbon particles and the size distribution. Electron-microscopic pictures of the specimens with higher resolution were used to specify the morphology of these particles. The results of the investigations carried out with the help of the program MEGRAN are presented in Table 1.

CNM ELECTROKINETIC PROPERTIES

It is known that different carbonic nanostructures can be charged negatively or positively; thus, it is suggested to separate the produced CNM by the electrophoresis method.

Research work was conducted using a laboratory electrophoresis device at different voltages to determine the intensity and conditions of the CNM separation. To study the electrokinetic properties of the nanocarbonic material powders, they were dispersed by the electrophoresis method in the alcohol and placed into a cell with flat electrodes. The applied voltage was varied in the range from 10 to 600 V with the current intensity depending on the powder specimen type.

There is no current in the pure alcohol at $U = 400$ V; that is, no electrochemical reactions proceed in the pure solvent.

With the dispersion of an industrial graphite powder in the alcohol at a voltage of $U = 350$ V, the current intensity amounted up to 25 mA. No active boiling of the liquid phase was observed, and the surfaces of the electrodes, anode, and cathode remained clean.

Table 1. The results of computer processing of the CNM specimens produced by the electrodischarge treatment of alcohols

Microphoto of specimens	Production conditions	Area of the particle distribution (number of particles for the analysis)	The form factor F_s of the particle distribution
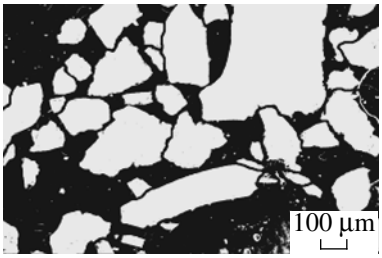	Butanol electrodischarge treatment	32 percent falls into the range from 20 to 40 μm^2; S_{min} = 10 μm^2; S_{max} = 250000 μm^2 (1057)	48 percent has $F_S \approx 1$; 20 percent has from 0.6 to 0.7
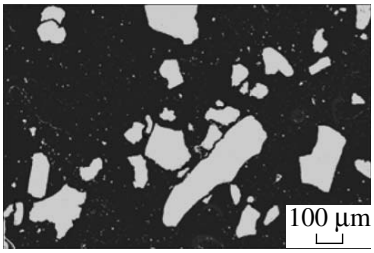	*n*-butanol electrodischarge treatment	16 percent falls into the range from 16 to 30 μm^2. S_{min} = 8 μm^2; S_{max} = 100000 μm^2 (1199)	64 percent has $F_S \approx 1$; 12 percent has from 0.6 to 0.7
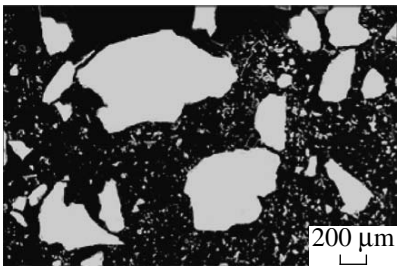	Electrodischarge treatment of isoamyl alcohol	32 percent falls into the range from 12 to 50 μm^2. S_{min} = 7 μm^2; S_{max} = 100000 μm^2 (1736)	23 percent has $F_S \approx 1$; 50 percent has from 0.4 to 0.7

The Saltykov form factor is determined from the formula $F_S = 4\pi S/p^2$, where S is the particle area, m^2; and p is the perimeter, m.

With the CNM produced at the electrodischarge treatment of the alcohols, the current amounts up to a value of I = 110 mA even at U = 150 V with the process being accompanied by active boiling and a black film of the carbonic material depositing on the anode.

With carbonic material produced at the electroexplosion of graphite conductors in organic liquids, there forms a film of dark brown color on the anode possessing high hygroscopicity. The process is characterized by the parameters U = 200 V and I = 110 mA. Active boiling begins at U = 300 V.

The experimental data prove that the nanocarbon particles are negatively charged. This CNM feature could be used both in the processes of separation of the produced carbonic nanomaterials and the production of highly active deposited sorbents. Utilizing the electrophoresis method, it is possible to form with the help of CNM uniform layers of a material on the surface of an article with a complex configuration thus improving the wear resistance.

The investigation of the movement of the CNM microparticles shows that the use of the electrophoresis device (with a [UIP]-1 apparatus for the direct current supply (varying the voltage from 10 to 600 V)) did not allow the rapid and complete separation of the CNM. The high-voltage electrophoresis method was originally used to increase the rate of the processes of the CNM separation and enrichment.

A high-voltage source of electric energy was utilized ensuring a voltage in the range from 1.5 to 10 kV was applied to the vessel's electrodes. The electric field

Table 2. Characteristic diffractograms and microscopic pictures of the CNM produced by the electrodischarge treatment of butanol and separated using the electrophoresis method

Electrode	Diffractograms of the CNM	Microscopic picture of the CNM
Anode	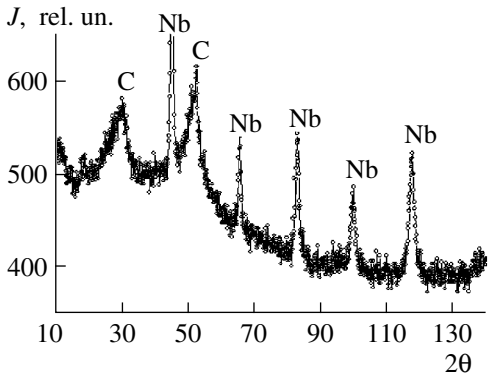	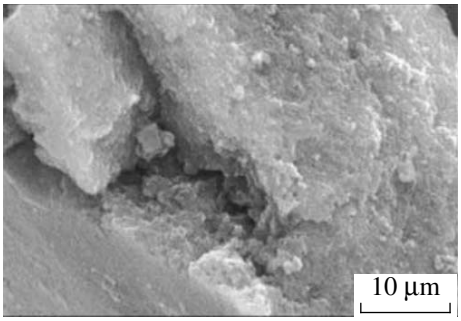
Cathode	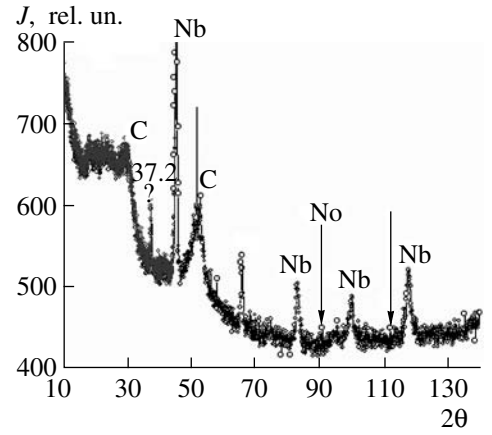	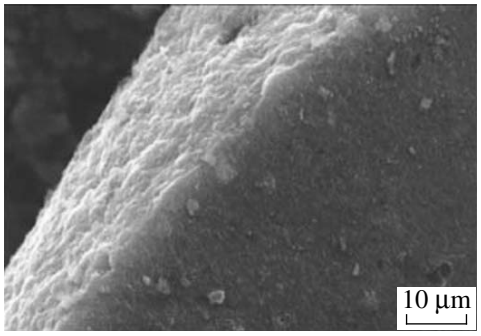

Note: C—graphite, Nb—substrate; *J*—radiation intensity, θ—angle of reflection.

intensity in the vessel amounts up to 10^4 kV/m. An external view of the electrophoresis device is presented in Fig. 2.

The use of the high-voltage electrophoresis device allowed separating the CNM and collecting it on the electrodes. The CNM collected from the anode surface and dried is a fine black powder and that collected from the cathode surface is a grey flocculation one.

The materials obtained on the anode and cathode have been investigated at the Institute of Metallophysics of the National Academy of Sciences of Ukraine by the methods of X-ray diffraction analysis and chemical analysis; the typical results are presented in Tables 2 and 3 (butanol is the source of the carbon).

The chemical composition of the powders obtained after the electrophoretic separation showed that it is necessary to purify them in order to remove impurities.

The results of the X-ray diffraction analysis of the CNM produced by the electrodischarge treatment of the ethyl alcohol after the separation in the high-voltage electrophoresis device are presented in Fig. 3.

The presented results (see Tables 2 and 3) allow one to draw a conclusion concerning the proficient separation of the CNM produced by the electrodischarge method in the high-voltage electrophoresis device. As

Table 3. Data of the chemical analysis of the CNM produced by the electrodischarge treatment of butanol and separated using the electrophoresis method

Electrode	The element amount, mass %					
	C	O	Fe	Al, Ca, Na	S	Total
Anode	70.1	16.1	11.0	2.2	0.6	100
Cathode	77.0	10.5	10.5	1.5	0.5	100

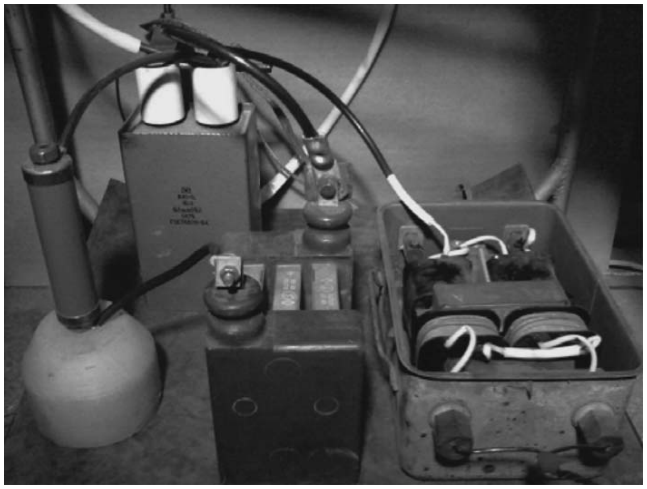

Fig. 2. The external view of the electrophoresis device.

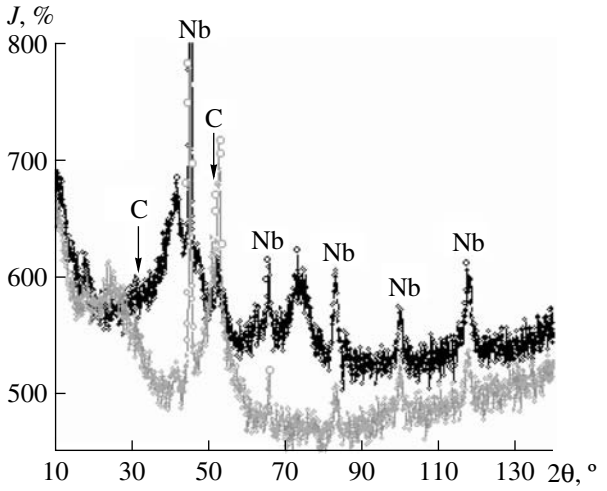

Fig. 3. Diffractograms of negatively charged (upper curve) and positively charged particles (lower curve) of CNM obtained at the electrodischarge treatment of ethyl alcohol.

the X-ray diffraction analysis shows, the materials collected from the anode and cathode differ greatly, but the carbon hybridization degree is close to $n = 2$. The diffractograms of similarly charged amorphous CNM produced by the electrodischarge method from different lower alcohols are similar.

The assay of the obtained results shows that the CNM collected from the anode and cathode are composites represented by different carbon phases in different ratios and mainly containing carbon and iron oxide. Evidently, the difference in the charge of the CNM particles is caused by the high content of electronegative oxygen in the specimen deposited on the anode.

CONCLUSIONS

The method and products of the electrodischarge treatment of alcohols have been investigated. A procedure for the separation of the CNM produced from lower alcohols by the high-voltage electrophoretic method was proposed and tested. It has been established that the high-voltage electrophoretic separation is more efficient than the low-voltage one. However, as the X-ray diffraction analysis results show, its implementation does not allow one to completely solve the problems connected with the separation and enrichment of the CNM. It is impossible to realize the complete separation of the crystallites into different allotropic forms of carbon using only the electrophoresis method; it is necessary to utilize complex ways of the CNM enrichment.

REFERENCES

1. Trunin, R.F., Compression of Condensed Substances by High Pressures of Shock Waves, *Usp. Fiz. Nauk*, 2002, vol. 171, no. 4, pp. 400–413.
2. Kuskova, N.I., Boguslavskii, L.Z., Smal'ko, A.A., and Gubenko, A.A., Production of Nanocarbon by Method of Electrodischarge Treatment of Organic Liquids, *Electr. Obrab. Mat.*, 2007, no. 4, pp. 46–52.
3. Vovchenko, A.I., Gorodyan, V.I., Kuskova, N.I., Razmenov, E.P., and Shvets, I.S., Ukraine Inventor's Certificate no. 77370, Byull.Izobret., 2006, no. 11.
4. Kuskova, N.I., Rud', A.D., Uvarov, V.N., Ivashchuk, L.I., Perekos, A.E., Boguslavskii, L.Z., and Oreshkin, V.I., Electric Explosion Methods of Synthesis of Carbonic Nanomaterials, *Metallofizica i noveishie tekhnologii*, 2008, vol. 30, no. 6, pp. 833–847

ISSN 1068-3755, Surface Engineering and Applied Electrochemistry, 2009, Vol. 45, No. 6, pp. 507–511. © Allerton Press, Inc., 2009.
Original Russian Text © V.L. Lanin, V.V. Parkovskii, 2009, published in Elektronnaya Obrabotka Materialov, 2009, No. 6, pp. 86–91.

OPERATING EXPERIENCE

Application of Convection and Infrared Heat Sources for Mounting and Demounting of Electronic Modules

V. L. Lanin and V. V. Parkovskii

State University of Informatics and Radioelectronics of Belarus, ul. P. Brovki 6, Minsk, 220013 Republic of Belarus
e-mail: vlanin@bsuir.by

Received July 13, 2009

Abstract—The parameters were optimized of convection and infrared heat sources for mounting and demounting of electronic modules on printed circuit boards with surface-mounted electronic components. The modeling of the thermoprofiles of convection and infrared sources allows one to optimize the process duration and the temperature of heating of the electronic components.

DOI: 10.3103/S1068375509060131

Convection heat sources are widely used for mounting and demounting of electronic modules on printed circuit boards in small-scale and pilot production [1]. Air is used as a heat carrier, which, passing through the heater (thermofan), acquires a high temperature. The heating efficiency and the temperature in the working zone considerably depend on the construction of the thermofan nozzle [2]. The process of heat transfer from the thermofan to the surface of the printed circuit board is described by the equation

$$Q = \frac{\lambda S t \Delta T}{l}, \quad (1)$$

where λ is the air's thermal conductivity, S is the area of the heated zone, t is the time of the heating, $\Delta T = (T_S - T_m)$ is the difference between the temperature of the heat source and the ambient temperature, and l is the distance between the heat source and the surface.

When calculating the heat quantity eliminated in the working zone, one should take into account the factors that influence the air dissipation at the head nozzle outlet of the thermofan (Fig. 1); for example, the coefficient of dissipation and the angle of dissipation α, which depend on the nozzle construction

$$K_r = \frac{r}{a + r}, \quad (2)$$

where r is the radius of the nozzle, and a is the distance over which the air dissipates when leaving the nozzle

$$a = l\tan(\alpha), \quad (3)$$

where α is the dissipation angle defined by the construction peculiarities of the head.

Then, the heat quantity eliminated in the working zone is calculated as follows:

$$Q = K_r \frac{\lambda S t \Delta T}{l}. \quad (4)$$

The heating temperature of the circuit board surface depends on the time, the heat exchange conditions, and the heat capacity of the circuit board material:

$$T_H = T_{HC}\left(1 - e^{-\frac{t}{\tau_h}}\right), \quad (5)$$

where T_{HC} is the temperature of the heat carrier, and τ_h is the heating time constant

$$\tau_h = \frac{C_T}{\alpha S_n}, \quad (6)$$

where C_T is the heat capacity of the material of the circuit board (0.9 J/°C for glass fiber plastic), and α is the heat exchange coefficient of the heat source with the circuit board surface.

$$\alpha = \frac{P}{S_n \Delta T}, \quad (7)$$

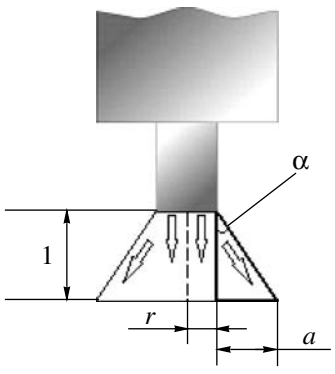

Fig. 1. Air flux at the thermofan nozzle outlet.

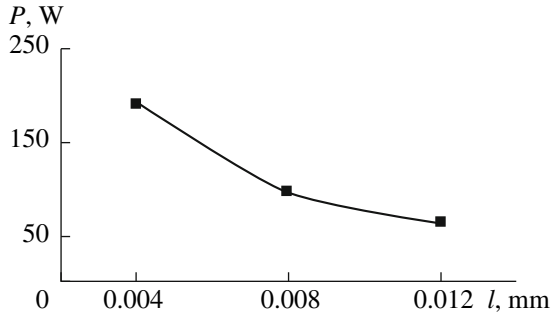

Fig. 2. Power eliminated in the heating zone of the convection heater versus the distance to the thermofan nozzle.

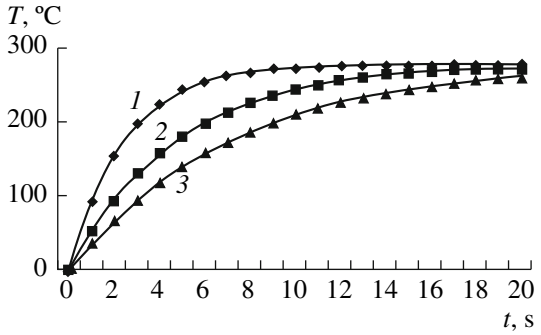

Fig. 3. Thermoprofile of heating by a convection heater for various distances to the source.

where P is the power of the convection heat source

$$P = K_r \frac{\partial Q}{\partial t} = K_r \frac{\lambda S \Delta T}{l}. \quad (8)$$

The power of the convection heating at the temperature difference $\Delta T = 255$°C, the time of the heating of 20 s, and the average heat conductivity of the air in the temperature range of 80–300°C, which amounts to 14.96 W/mK, decreases nonlineary when the distance between the heat source and the surface increases (Fig. 2). The temperature in the heating zone reaches its maximal values within 15–20 s and also depends on the distances to the heat source (Fig. 3). The temperature in the working zone increases slowly when the distance to the source increases; this lowers the thermal shock on the printed circuit board.

The main advantage of convection heat sources is the ability to use various thermofan heads for the air flux dissipation. This method of heating is appropriate to use while repairing electronic modules. The process of demounting of microcircuits using a thermofan includes the following operations: placing of the vacuum grip on its surface, melting of the solder alloy by hot air (Fig. 4a), and demounting (Fig. 4b). The process of demounting using hot air is rather complicated, since the temperature in the heating zone depends on the distance to the heated surface and also on the relative inclination angle of the tool to the surface.

It is necessary to use precise solder dosing at convection heating, since the greater the solder mass is, the longer time is necessary for its unsoldering; this implies that the printed circuit board is subjected to the action of high temperature for a longer time, which is critical for its durability parameters. The application of lead-free solders with higher melting points makes the problem of demounting by convection heaters more complicated, since it demands that one control the temperature in the working zone very precisely.

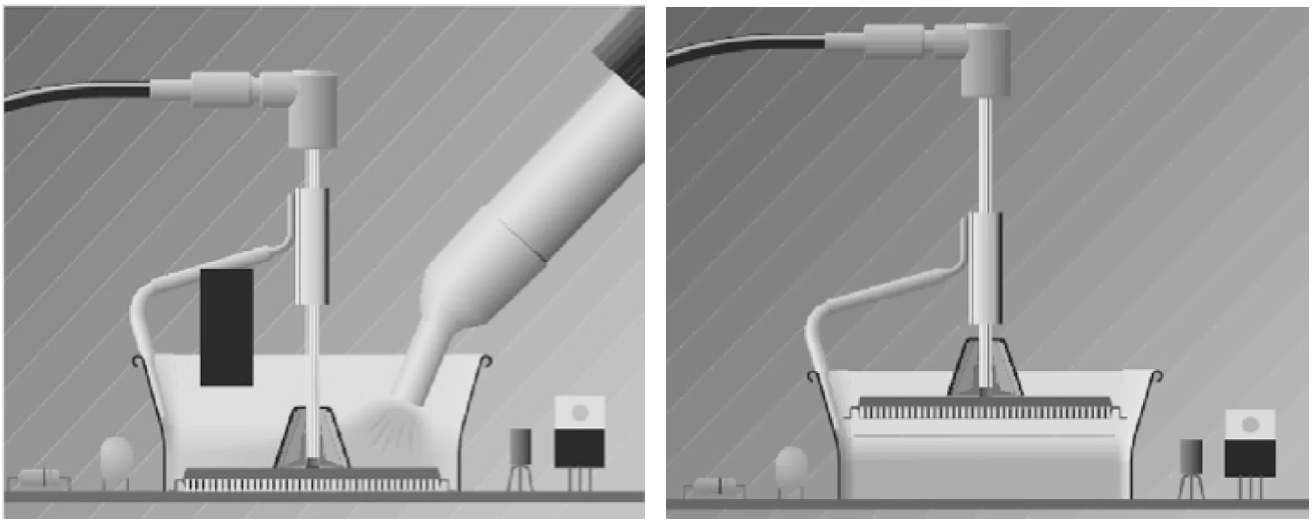

(a) (b)

Fig. 4. Mounting (a) and demounting (b) of the component from the board using a thermofan.

Sources of infrared (IR) heating are also widely used for mounting of surface-mounted electronic components on printed circuit boards and for heating of circuit boards in the process of mounting or repairing of electronic modules. Infrared heating possesses several advantages, though their practical application depends on the construction of the installation for the IR heating [3].

Depending on the specific conditions, reflectors with various geometry are used that form a heat field in the heating zone: focusing, diffuse, and with a nozzle head. The main advantages of IR heat sources are as follows: the higher heating temperature, its stability during the soldering process, and the ability to precisely control the temperature in the heating zone. However, at IR heating, a large amount of heat is absorbed by the cases of components, since their area is large as compared with the connections.

The intensity of the IR radiation can be presented as the sum of the intensities of the direct and the reflected fluxes [4]:

$$I = I_{\text{dir}} + I_{\text{ref}}. \tag{9}$$

The intensity of the direct radiation flux depends on the power of the IR source P_s, the distance to the source h, and the dimensions of the heating zone:

$$I_{\text{dir}} = 2\frac{P_s}{l\sqrt{x^2 + h^2}}, \tag{10}$$

where l is the heating zone length, and x is the halfwidth of the heating zone (Fig. 5).

The intensity of the IR radiation flux with account for the coefficient of reflection is

$$I_{\text{ref}} = \frac{\mu K_S P_s}{2\pi l\sqrt{R_r^2 + \left(\frac{h^2}{4f} f\right)^2}}, \tag{11}$$

where R_r is the radius of the reflector, f is the focal distance, K_S is the coefficient of the useful mirror surface of the reflector, and μ is the coefficient of the reflection.

The reflection coefficient is defined using the geometrical dimensions of the IR source and the reflector surface

$$K_S = -\frac{S_S}{2S_r}, \tag{12}$$

where S_S and S_r are the surface areas of the IR lamp and the reflector, respectively.

The intensity of the resultant flux of the IR radiation impinging the surface is limited by the width of the reflector base

$$I_{\text{ref}} = K_S\mu 2\frac{\sum_{i=1}^{n}\left(P_s\left/2\pi l\sqrt{R_r^2 + \left(\frac{h^2}{4f} - f\right)^2}\right.\right)}{n}, \tag{13}$$

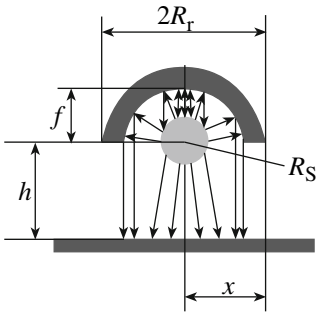

Fig. 5. Schematic view of the IR heater

where n is the number of intervals chosen for the heating zone discretization relative to its center.

Then, the intensity of the direct IR radiation is

$$I_{\text{dir}} = 2\int_0^x \frac{P_S}{l\sqrt{x^2 + h^2}} dx. \tag{14}$$

The temperature in the zone of the IR heating is determined according to the Stefan–Boltzmann law:

$$T_H = \sqrt[4]{\frac{I + KT_c^4}{K}} - 273, \tag{15}$$

where K is the Stefan–Boltzmann constant.

The temperature in the heating zone also depends on the process duration:

$$T_{\text{heat}} = T_H\left(1 - e^{\frac{-\tau}{\tau_h}}\right), \tag{16}$$

where T_{heat} is the temperature in the heating zone, τ is the duration of the heat flux action, and τ_h is the heating time constant.

$$\tau_h = \frac{C_T}{\alpha S_{\text{surf}}}, \tag{17}$$

where S_{surf} is the area of the heating zone confined by the geometrical dimensions of the reflector, α is the heat exchange coefficient with the circuit board material, and C_T is the heat capacity of the circuit board material.

$$\alpha = \frac{P_H}{S_{\text{syrf}}\Delta T}, \tag{18}$$

where ΔT is the difference between the heating temperature and the ambient temperature, and P_H is the heating power

$$P_H = I(S_S + S_r). \tag{19}$$

Parameters of the source and the zone of IR heating

P_s, W	h_s, m	R_s, m	l, m	f, m	x', m	l' , m	Reflector surface area S_r, m^2
500	0.05	0.01	0.1	0.03	0.06	0.1	0.009

The dependence of the power eliminated in the zone of heating by the IR source versus the distance is shown in Fig. 6 (see the relevant parameters in the Table).

The temperature in the heating zone depends both on the process duration and the distance to the IR heating source (Fig. 7). The temperature in the working zone increases sufficiently fast (for 5–7 s) and, unlike with convection heating, is not critically sensitive to the changing of the distance to the surface.

In the process of mounting and demounting of electronic modules using convection heat sources, the printed circuit board is heated using an IR radiation source to maintain the board temperature and prevent its thermal shock (Fig. 8). This combined method of heating was implemented in an ERSA IR/PL650 installation for repairing of electronic modules [5], which represents the third-generation of systems for IR soldering combining three main technological systems: IR and convection heating, temperature feedback control, and contactless temperature measurements. The installation exhibited good performance while working with complex printed circuit boards with a large number of components when a lead-free technology was used.

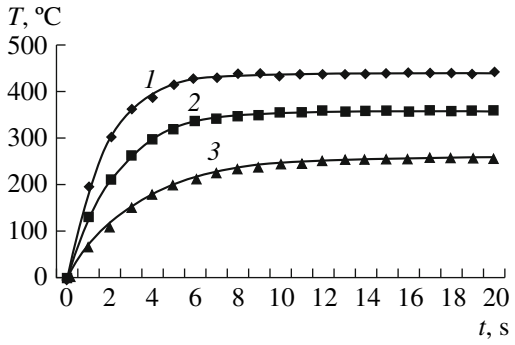

Fig. 6. Power eliminated in the heating zone of the IR heater versus the distance to the source.

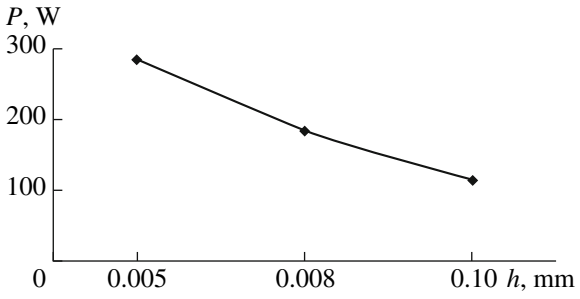

Fig. 7. Thermoprofile of IR heating for various distances to the source.

While using IR heat sources, one should take into account the reflector construction and the distance from the source to the board surface; otherwise, the radiation will not focus well in the heating zone. This can lead to overheating of the board or component, or the quantity of the eliminated heat will not be sufficient to melt the solder. It is especially important to control the temperature accurately when a lead-free technology is employed. In this case, automated temperature control systems should be used that ensure the specified process's thermoprofile.

Modeling of thermoprofiles of convection and IR heating sources allows one to calculate the temperature in the heating zone as a function of the process time and to optimize the process of mounting and demounting of electronic modules; this is very important when expensive components are used. For convection heat sources,

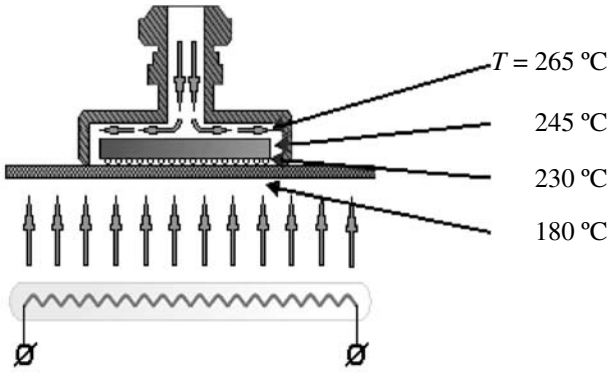

Fig. 8. Heating of the electronic module by convection and IR heaters.

it is necessary to optimize the head construction for the optimal spreading of the heat flow, the air pressure, and the spreading rate in the heating zone.

REFERENCES

1. Judd, M., and Brindley, K., *Soldering in Electronics Assembly*, Oxford: Newnes, l999.
2. Lanin, V.L., and Parkovskii, V.V., Mounting and Demounting of Electronic Components, *Kompon. Tekhnol.*, 2009, no. 3, pp. 147–152.
3. Lanin, V.L., Infrared Heating in the Technology of Soldering Components in Electronics, *Surf. Eng. Appl. Electrochem.*, 2007, no. 5, pp. 381–386.
4. Zvorykin, D.V., and Prokhorov, Yu. N., *Primenenie luchistogo infrakrasnogo nagreva v elektronnoi promyshlennosti* (Application of Radiant Infrared Heating in Electronic Industry), Moscow: Energiya, 1980.
5. Afanas'ev, V., IR/PL650: the Third Generation of ERSA Service Centers, *Tekhnol. Elektron. Prom-sti.*, 2006, no. 4, pp. 80–83.